Design, Fabrication and Characterization of Gallium Nitride High-Electron-Mobility Transistors

by Jonathan George Felbinger

DESIGN, FABRICATION AND CHARACTERIZATION OF GALLIUM NITRIDE HIGH-ELECTRON-MOBILITY TRANSISTORS

A Dissertation

Presented to the Faculty of the Graduate School

of Cornell University

in Partial Fulfillment of the Requirements for the Degree of

Doctor of Philosophy

by

Jonathan George Felbinger

August 2010

DESIGN, FABRICATION AND CHARACTERIZATION OF
GALLIUM NITRIDE HIGH-ELECTRON-MOBILITY TRANSISTORS

Jonathan George Felbinger, Ph.D.
Cornell University 2010

Over the past few years, systems based on gallium nitride high-electron-mobility transistors (GaN HEMTs) have increasingly penetrated the markets for cellular telephone base stations, RADAR, and satellite communications. High power (several W/mm), continuous-wave (CW) operation of microwave HEMTs dissipates heat; as the device increases in temperature, its electron mobility drops and performance degrades. To enhance high-power performance and enable operation in high ambient temperature environments, the $Al_xGa_{1-x}N$/GaN epitaxial layers are attached to polycrystalline diamond substrates. The lower surface temperature rise on GaN-on-diamond is directly measured; subsequently, improved electrical performance is demonstrated on diamond versus the native (Si) substrates. Benchmark $Al_xGa_{1-x}N$/GaN devices are fabricated on SiC for comparison to diamond, Si, and bulk GaN substrates; the merits and performance of each is compared. In collaboration with Group4 Labs, X-band amplifier modules based on GaN-on-diamond HEMTs have been demonstrated for the first time. Recent efforts have focused on substituting $Al_xIn_{1-x}N$ barriers in place of $Al_xGa_{1-x}N$ to achieve higher output power at microwave frequencies and addressing the challenges of this new material system. Ultimately, these techniques may be combined to attain the utmost in device performance.

BIOGRAPHICAL SKETCH

Jonathan G. Felbinger was raised in Chicago, Illinois. He studied engineering and music at Vanderbilt University in Nashville, Tennessee, and graduated *summa cum laude* with Honors in Electrical Engineering and Mathematics. He was awarded the Electrical Engineering Program Award and the Dean's Award for Outstanding Service. In the summer of 2005, Jonathan worked as a Visiting Fellow in the Guidance Hardware Division at Draper Laboratory, Cambridge, Massachusetts. Interested in advancing the frontier of electronics, Jonathan joined Prof. Lester F. Eastman's compound semiconductor device research group at Cornell University in the summer of 2006. His pioneering work into microwave GaN-on-diamond transistors was recognized in 2007 with the Best Student Paper Award at the 31st Workshop on Compound Semiconductor Devices and Integrated Circuits in Europe (WOCSDICE) in Venice, Italy. During the summer of 2007, he advanced his research into homoepitaxial AlGaN/GaN-on-GaN HEMTs as a Visiting Scientist within the GaN RF Power Electronics Group at the Fraunhofer Institute for Applied Solid-State Physics (IAF), Freiburg im Breisgau, Germany. During the 2007-2008 academic year, he received the Lester Eastman Graduate Fellowship in recognition of his research.

Within his minor concentration in Science & Technology Studies at Cornell, Jonathan explored his interest in U.S. technology policy, with a focus on dual-use technologies, under Prof. Judith Reppy. In support of this research, he received an Elaine Scott Travel Grant from the Cornell University Peace Studies Program in 2008.

Jonathan remained active outside of the laboratory, serving as the 2009 President of the Cornell Engineering Graduate Student Association and performing regularly as principal clarinetist with the Cornell orchestras and chamber ensembles.

Geliebte Familie

ACKNOWLEDGEMENTS

Die Philosophen haben die Welt nur verschieden interpretiert;
es kommt darauf an, sie zu verändern.

- Karl Marx

Foremost I wish to acknowledge Prof. Lester F. Eastman for imparting technical knowledge and providing sage wisdom and support, from our very first meeting, without which this culmination of our collaboration would not have been possible. Additionally, I am grateful to Prof. Michael Spencer for his early interest in and support of the research. Furthermore, I thank Prof. Judith Reppy, whose expertise and encouragement piqued my interest in the broader social concerns of the development of dual-use technology.

Financial support for this work was provided by a Missile Defense Agency (MDA) contract monitored by John Blevins of the Air Force Research Laboratory (AFRL); Group4 Labs, Inc.; and the Office of Naval Research (ONR) Millimeter-wave Initiative for Nitride Electronics (MINE) Multidisciplinary Research Program of the University Research Initiative (MURI) subcontract from the University of California, Santa Barbara (UCSB). Such extensive research would not have been possible without the generous donation of semiconductor material from Group4 Labs, IQE RF, Northrop Grumman, EPFL LAPSE, and General Electric. Certain measurements within this work were facilitated by Lockheed Martin Corporation, Syracuse, NY (A. Allen and K. Robinson); the Air Force Research Laboratory, Dayton, OH (Capt. B. Winningham); Northrop Grumman Space Technology, Redondo Beach, CA (B. Luo and R. Sandhu) and TriQuint Semiconductor, Richardson, TX (D. Dumka and P. Saunier).

I would like to acknowledge the hospitality of the Directors of the Fraunhofer Institute for Applied Solid-State Physics (IAF), Prof. Dr. Günter Weimann and Prof. Dr. Oliver Ambacher, and the guidance and assistance of Dr. Rüdiger Quay. For finding the time to discuss their work and experiences as it pertained to my research interests, I remain grateful to Dale R. Corson, former President and, later, Chancellor of Cornell University, and Steven Aftergood, Director of the Government Secrecy Project at the Federation of American Scientists (FAS).

Finally, I thank my colleagues in the Eastman Group, including Bill Schaff, Quentin Diduck, Dong Hao, Kristoph Matthews, and Junxia Shi, for innumerable discussions and holistic support.

TABLE OF CONTENTS

Biographical Sketch iii

Dedication iv

Acknowledgements v

List of Figures x

List of Tables xiii

List of Abbreviations xiv

List of Symbols xvi

Chapter 1: Introduction 1

Chapter 2: Gallium Nitride HEMTs 6

2.1. Material Properties of Gallium Nitride and Related Alloys 6

2.1.1 Lattice Structure 6

2.1.2 Band Structure 7

2.1.3 Polarization 9

2.2 Substrates 12

2.3 Growth Techniques 16

2.4 Dislocations 17

2.5 HEMT Electrical Properties 21

Chapter 3: HEMT Design and Fabrication 28

3.1 Epitaxial Layers 28

3.2 AlInN Barriers 31

3.3 Surface Passivation 31
3.4 Process Technology 32
3.4.1 Alignment Marks 33
3.4.2 Ohmic Metallization 34
3.4.3 Mesa Isolation 38
3.4.4 Ohmic Anneal 38
3.4.5 Passivation 38
3.4.6 Gate & Pad Metallization 40
Chapter 4: HEMT Characterization 42
4.1 Material Pre-Screening 42
4.2 Transfer Length Method 43
4.3 DC 45
4.4 Thermal Measurement 46
4.5 Thermal Modeling 48
4.6 Small-Signal Measurement and Modeling 50
4.7 Pulsed DC 55
4.8 Load-pull 56
4.9 Efficiency Model for Multi-Finger HEMTs 61
Chapter 5: Approaches 64
5.1 AlGaN/GaN-on-Diamond HEMTs 64
5.1.1 Material Preparation 65
5.1.2 Fabrication and Measurement 66

5.1.3 AlGaN/GaN-on-Diamond Performance 66
5.1.4 Comparison between AlGaN/AlN/GaN HEMTs on Diamond and Si Substrates 68
5.1.5 Summary 70
5.2 AlGaN/GaN-on-GaN HEMTs 70
5.2.1 Fabrication and Measurement 71
5.2.2 Experimental Results 71
5.2.3 Summary 76
5.3 AlInN Barrier HEMTs 76
5.3.1 Material Structure and Properties 77
5.3.2 Fabrication and Characterization 77
5.3.3 Experimental Results 78
5.3.4 Summary 81
Chapter 6: Conclusions and Future Directions 82
Appendix A: Information Controls on Dual-Use Technology 84
A.1 Case Study 95
A.2 Recommendations & Conclusion 103
Works Cited 105

LIST OF FIGURES

Figure 1. Band gap energy ε_g versus lattice constant a for nitrides and other semiconductors at 300K 2

Figure 2. Operating regimes of high-frequency semiconductor technologies [2] 3

Figure 3. Natural band alignment for unstrained semiconductors [3] 4

Figure 4. Band structure of wurtzite GaN [7] 8

Figure 5. Fixed interface charge density evolved at an Al(Ga,In)N/GaN heterojunction; the spontaneous and piezoelectric components of the total charge density are indicated 23

Figure 6. CBM and VBM energy as a function of lattice constant for all compositions of ternary nitrides at 300K 25

Figure 7. Conduction band discontinuity for nitride heterojunctions at 300K 25

Figure 8. Conduction band edge of an AlGaN/GaN HEMT structure 27

Figure 9. Conduction band edge of an AlGaN/GaN HEMT structure with (solid) and without (dashed) an AlN interbarrier 30

Figure 10. Contact resistance for Ti/Al/Mo/Au contacts to highly-doped n^{++} Ge:GaN as a function of dopant concentration and anneal temperature 35

Figure 11. Field-plated Ni/Au gate atop $Al_{0.26}Ga_{0.74}N$/GaN-on-diamond depicting the asymmetric gate extension, atop the SiN_x passivation layer, extending toward the drain 40

Figure 12. Modeled temperature dependence of thermal conductivity 49

Figure 13. Two-dimensional finite element simulation of the nonlinear dependence of temperature rise versus dissipated power for a GaN-on-SiC HEMT 50

Figure 14. Linear equivalent circuit for a GaN HEMT 54

Figure 15. Classes of amplifier operation illustrated by quiescent point of gate and drain bias and load line; the dynamic class A load line is indicated by the light-gray, dashed ellipse [81] 58
Figure 16. Block diagram for dc, small-signal, and 10 GHz power measurements..... 60
Figure 17. Thermal resistance as a function of channel width and gate pitch for an 8-finger $Al_xGa_{1-x}N$/GaN HEMT on a 100 μm Si, SiC, or diamond substrate..... 62
Figure 18. Drain efficiency and temperature rise as a function of pitch..... 63
Figure 19. 1.5", 2", and 4" GaN-on-diamond wafers 65
Figure 20. Output power measured at 10 GHz CW, V_{DS} = 35 V class AB for a $2 \times 100 \times 0.1$ μm AlGaN/GaN-on-diamond HEMT with matching condition $Z_S = 178 \,||\, j82\ \Omega$ and $Z_L = 454 \,||\, j748\ \Omega$ 67
Figure 21. I-V characteristics for a $2 \times 50 \times 0.06$ μm GaN-on-diamond (solid) and GaN-on-Si (dotted) HEMT 69
Figure 22. Quasi-dc (solid) and 200 ns pulsed (hollow) off-state (circular; V_{DS} = 0 V, V_{GS} = 0 V) and drain-lag (square; V_{DS} = 20 V, V_{GS} = −7 V) performance of a 2×100×0.1 μm (FP), 50 μm pitch $Al_xGa_{1-x}N$/GaN HEMT 73
Figure 23. 18 GHz large-signal power-matched performance of a $2 \times 75 \times 0.1$ μm (FP), ... 74
Figure 24. Thermal resistance for 80 μm-wide GaN-on-GaN and GaN-on-SiC devices measured by SThM and calculated using a 3D finite-difference (FD) model..... 75
Figure 25. Gate leakage for typical 2-finger $Al_xIn_{1-x}N$/GaN-on-SiC HEMTs from each process at V_{DS} = 10 V..... 79
Figure 26. Number of publications on the subject of GaAs transistors by author affiliation for the top seven contributing countries, 1972–2008. 98
Figure 27. Collaborative publication count on the subject of GaAs transistors between the United States and other top-seven contributing countries, 1972–2008. 99

Figure 28. Number of publications on GaAs transistor technology by domestic authors, 1972–2008; black indicates the subset of publications that include collaborators with foreign affiliations. 100
Figure 29. Percentage of US-Affiliated GaAs Publications with International Collaborators, 1981–2008. 101

LIST OF TABLES

Table 1. Calculated and experimental (denoted "e") unit cell dimensions at 300K..... 7

Table 2. Band gap, low-field mobility, breakdown field, relative static dielectric constant, and spontaneous polarization of wurtzite nitrides at 300K..... 9

Table 3. Second-order band gap bowing parameter for wurtzite ternary nitride alloys. 9

Table 4. Second-order bowing parameter for selected wurtzite ternary nitride alloys. 10

Table 5. Spontaneous polarization and hexagonal crystal properties for binary wurtzite nitrides at 300K [6] 11

Table 6. Properties of commercially-available GaN substrates at 300K 13

Table 7. Calculated threshold voltage and zero-bias and full-channel 2DEG sheet density for GaN-on-diamond HEMTs with and without an AlN interbarrier..... 30

Table 8. Work function Φ_M of selected metals and alloys to GaN..... 37

Table 9. Ohmic contact properties measured by TLM before and after mesa isolation for a 200 Å $Al_{0.25}Ga_{0.75}N$/GaN-on-GaN HEMT..... 44

Table 10. Output waveform, conduction angle, peak drain efficiency, and maximum output power for passively-terminated continuous-wave amplifier operation..... 59

Table 11. Characteristics of an $Al_{0.26}Ga_{0.74}N$/GaN-on-diamond HEMT averaged over more than twenty 2 × 100 μm devices..... 67

Table 12. Ti/Al/Mo/Au ohmic contact properties measured by four-point probe TLM at seven sites across each wafer 72

Table 13. Ohmic contact properties measured by four-point probe TLM..... 80

LIST OF ABBREVIATIONS

2DEG	Two-Dimensional Electron Gas
AFM	Atomic Force Microscopy
ALD	Atomic Layer Deposition
CAD	Computer-Aided Design
CBM	Conduction Band Minimum
C –V	Capacitance–Voltage
CW	Continuous Wave
FZ	Float-Zone, high-resistivity Si
HEMT	High Electron Mobility Transistor
HFET	Heterostructure Field Effect Transistor
HVPE	Hydride Vapor Phase Epitaxy
IR	Infrared
MAG	Maximum Available Gain
MBE	Molecular Beam Epitaxy
MOCVD	Metal Organic Chemical Vapor Deposition
MSG	Maximum Stable Gain
MTA	Microwave Transition Analyzer
OMVPE	Organometallic Vapor Phase Epitaxy
P.A.E.	Power Added Efficiency
PECVD	Plasma-Enhanced Chemical Vapor Deposition
RHEED	Reflection High Energy Electron Diffraction
RTA	Rapid Thermal Anneal
SI	Semi-Insulating
SiopSiC	Silicon-on-poly-SiC, a composite substrate

SOI	Silicon-on-Insulator, a composite substrate
STEM	Scanning Transmission Electron Microscopy
SThM	Scanning Thermal Microscopy
TBR	Thermal Boundary Resistance
TLM	Transfer Length Method measurement
UID	Unintentionally Doped
VBM	Valence Band Maximum
VNA	Vector Network Analyzer

LIST OF SYMBOLS

d_{crit}	critical layer thickness
E	electric field, V/cm
ε_1	biaxial strain
ε_c	conduction band energy
ε_g	band gap
ε_f	Fermi level
ϵ_0	dielectric permittivity of free space, 8.854×10^{-14} F/cm
ϵ_r	relative static dielectric permittivity
f_T	unity-current-gain frequency
f_{MAX}	maximum frequency of oscillation
g_m	transconductance
n_s	sheet density
Φ_M	work function
Φ_{SB}	Schottky barrier height
P_{pz}	piezoelectric polarization charge density
P_{sp}	spontaneous polarization charge density
μ_d	electron drift mobility
V_t	Threshold voltage

CHAPTER 1: INTRODUCTION

The binaries, aluminum nitride (AlN), gallium nitride (GaN), indium nitride (InN), and their alloys constitute the group III–nitride (III–N) family of semiconductors. These materials have been the subject of active research spanning nearly two decades and involving researchers in more than thirty countries. Prior, extensive development of the related arsenide family, another material system combining elements from group III and V of the periodic table, began with exploring optoelectronic applications in the 1960s and high-speed electronics in the 1970s. The development of the arsenides as the "second generation of useful semiconductors" established the role of nitride devices, including white light emission or "solid television display" [1]. At present, GaN technologies permeate the markets for military sensing, wireless communications, solid-state lighting, and "green" energy including solar cells and high-efficiency power conversion.

Many of the unique properties of GaN derive from its material structure. The room-temperature band gap energy of various semiconductor materials is plotted as a function of lattice constant in Figure 1. Solid lines connect families of III–V materials, including the wurtzite nitrides (note that boron nitride, BN, is presented in its common, cubic structure), the phosphides, the arsenides, and the antimonides. Additionally, the effective lattice constant of substrates for the epitaxial growth of GaN are indicated by vertical, dotted lines. The visible region of the electromagnetic spectrum from red (λ = 750 nm, ε_g = 1.65 eV) through violet (λ = 400 nm, ε_g = 3.10 eV) is shaded. With respect to electromagnetic emission and absorption, ternary alloys of the III-N family are of great commercial interest for their direct band gaps spanning nearly an order of magnitude in energy, which includes the spectrum from ultraviolet through near infrared.

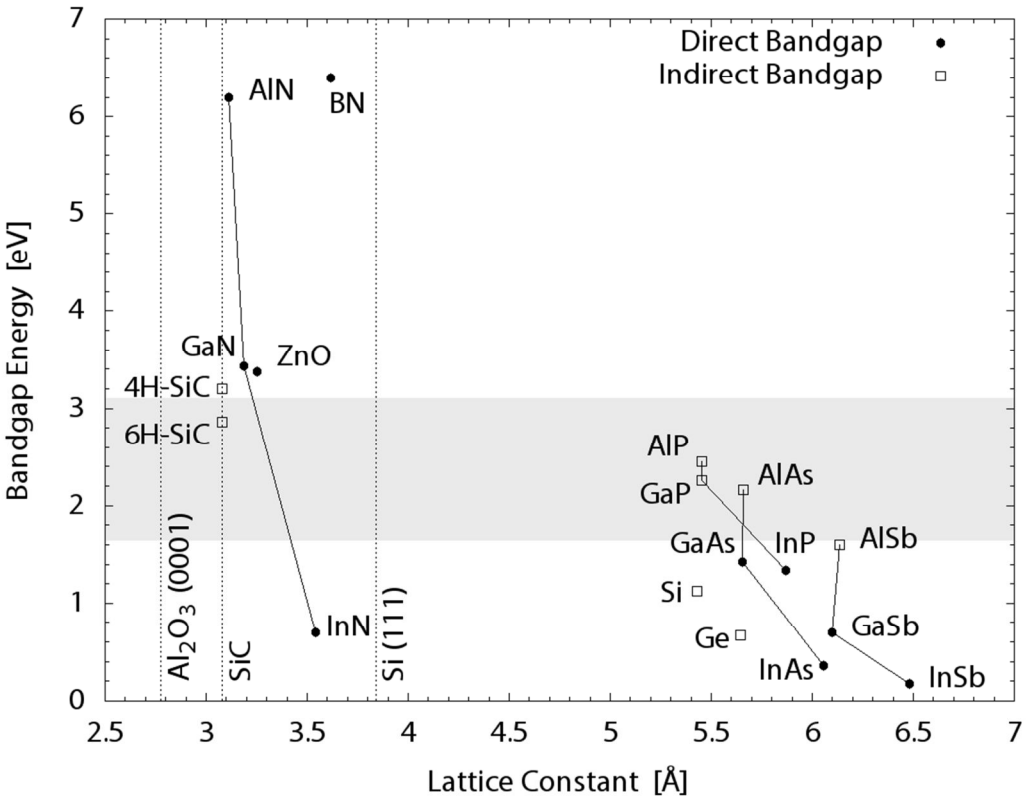

Figure 1. Band gap energy ε_g versus lattice constant a for nitrides and other semiconductors at 300K

The scope of this dissertation encompasses the design, fabrication, and characterization of GaN high-electron-mobility transistors (HEMTs) for applications requiring high-power, high-frequency amplification. The suitability of GaN to deliver higher power relative to competing technologies through microwave and millimeter-wave (mm-wave) frequency regimes is illustrated in Figure 2.

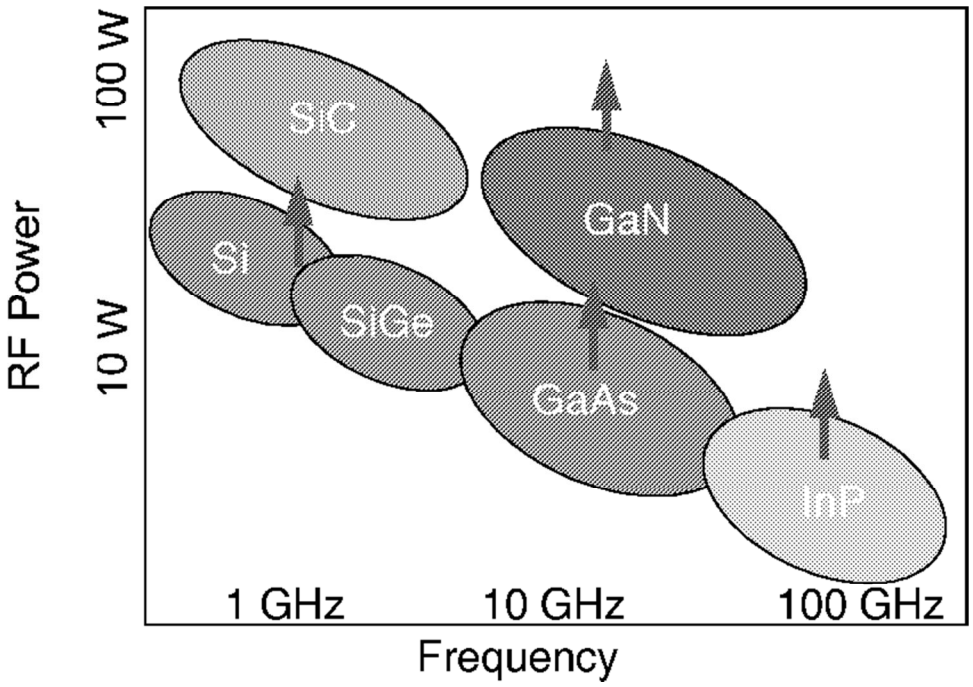

Figure 2. Operating regimes of high-frequency semiconductor technologies [2]

Chapter 2 details the unique combination of material properties in the GaN family. Unlike most III–V semiconductors, which crystallize in the zincblende lattice, the Al–Ga–In nitrides form stably in the wurtzite lattice. The strongly polar metal–N bond in this structure results in spontaneous polarization-induced surface charge densities on the order of 0.01 C/cm². The pseudomorphic, i.e., strained, growth of thin $Al_xGa_{1-x}N$ or high Al composition $Al_xIn_{1-x}N$ layers atop GaN introduces a complementary piezoelectric polarization charge density of even greater magnitude. These charge densities are utilized to produce an undoped field effect transistor with a quantum-confined electron density on the order of 10^{13}/cm² and current density of 1–2 A/mm. Challenges related to the growth and performance of GaN HEMTs resulting from the lack of a native substrate, which differentiates the nitrides from the other commercial semiconductors, are discussed. The theory may be employed to inform the development of high-power, high-frequency GaN transistors.

As suggested in Figure 3, the band alignment of the III-N family of devices is such that type I, straddling, heterojunctions form between binary and ternary Al–Ga–In nitrides. Chapter 3 builds upon the material properties introduced in Chapter 2 and details the device structure of the undoped, depletion-mode GaN HEMT. The chapter culminates with a discussion of the performance limitations faced by state-of-the-art devices.

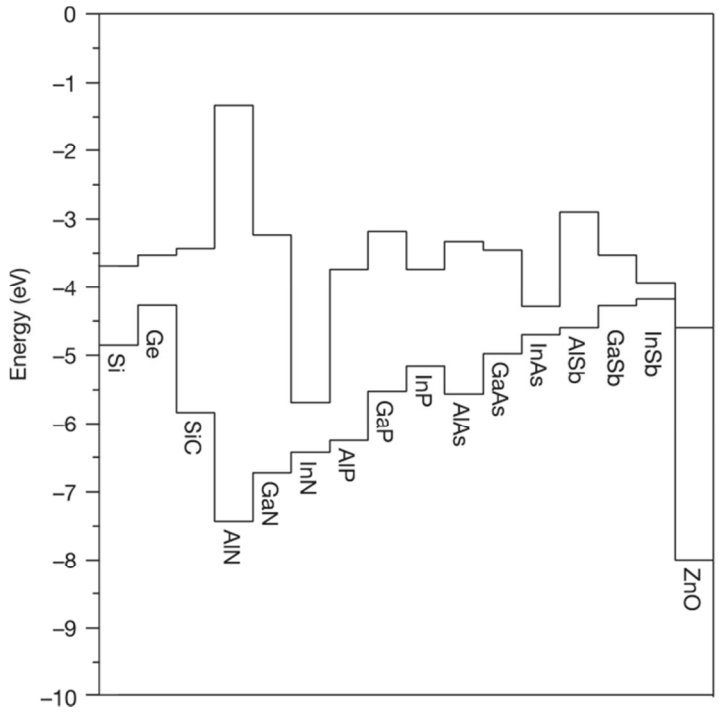

Figure 3. Natural band alignment for unstrained semiconductors [3]

Chapter 4 describes the suite of methods and techniques used to characterize GaN material and devices. In a research environment, for which the material growth is not controlled by tight production tolerances, it is beneficial to pre-screen the epitaxy to verify its electrical performance prior to processing . A combination of Lehighton, capacitance–voltage (C–V), and Hall measurements provide an indication of the electrical performance of the devices. The C–V data may be compared to models of the

structure to identify any discrepancies. During and following fabrication, transfer length method (TLM) measurements may be used to assess ohmic contact quality and monitor for any process-induced degradation affecting the electron channel. Subsequent to device fabrication, HEMTs are characterized at dc, both static and pulsed, and ac, both small-signal linear response and large-signal nonlinear performance. These methods and techniques enable the evaluation of novel GaN transistor designs.

In this dissertation, three approaches toward enhancing the performance of GaN HEMTs are described. First, purely to ameliorate the thermal limitations on the electrical performance of high-power HEMTs, the use of composite substrates comprised of transferred $Al_xGa_{1-x}N$/GaN epitaxial layers atomically attached to CVD diamond is investigated. Next, the homoepitaxial growth of $Al_xGa_{1-x}N$/GaN layers atop small, bulk GaN substrates is explored as a means toward low defect density epitaxial layers offering enhanced performance. Finally, the growth of $Al_xIn_{1-x}N$/GaN epitaxial layers providing increased sheet charge density and reduced biaxial strain is investigated. These three, disparate approaches are discussed in detail, including the presentation of detailed material and device characterization, in Chapter 5.

Chapter 6 summarizes the results of this research and proposes an holistic approach for realizing the best performance of GaN-based HEMTs. Future directions for GaN research and applications are presented.

CHAPTER 2: GALLIUM NITRIDE HEMTS

Gallium nitride (GaN) is a material of considerable interest for its reasonable electron mobility, high breakdown field, and high electron velocity. The nitrides offer a platform for harsh environments, and the large band gap and gate-oxide-free high electron mobility transistor (HEMT) design provide inherent radiation hardness. Furthermore, properly-designed devices perform in extremely harsh environments. For example, HEMTs utilizing an $Al_xIn_{1-x}N$/GaN heterostructure and a copper-based ohmic and Schottky contact scheme have been demonstrated to operate 50 hours at 900°C ambient temperature with constant threshold voltage between room temperature and 800°C [4]. The high performance of GaN-based devices is derived from its material properties.

2.1. Material Properties of Gallium Nitride and Related Alloys

2.1.1 Lattice Structure

Most of the III–V semiconductors crystallize in the zincblende lattice, which is comprised of two interpenetrating face-centered cubic (FCC) lattices displaced by [¼ ¼ ¼]. Similar to many II–VI compounds, the family of Al–Ga–In nitrides form stably in the wurtzite lattice, which is the hexagonal analogue of the zincblende lattice and is comprised of two interpenetrating hexagonal close packed (HCP) lattices. The zincblende unit cell contains eight atoms per unit cell volume a^3 versus the hexagonal wurtzite unit cell, which contains four atoms per volume $(3\sqrt{3}/2)a^2c$.

Examining the zincblende crystal along the [111] direction, we observe the stacking sequence of planes ABCABC, whereas, for the wurtzite crystal along the [0001] direction, or c-axis, the stacking sequence is ABAB. Along these respective axes,

the lattices lack inversion symmetry. Within this dissertation, all of the wurtzite nitrides are grown along the c-axis; thus, due to the lack of symmetry, one c-plane face of the crystal is comprised of metal atoms and the other nitrogen. For a GaN growth, if the nitrogen layer is terminated at the substrate and the Ga layer at the surface, it is said to be Ga-face, and vice versa for N-face crystal orientation.

Although the ideal HCP lattice parameters are $u_0 = 3/8 = 0.375$ and $c_0/a_0 = (8/3)^{½} \approx 1.6330$, the nitride semiconductors deviate from these ideal geometries. Table 1 presents two sets of simulated and one set of experimental lattice parameters for three different binary nitrides.

Table 1. Calculated and experimental (denoted "e") unit cell dimensions at 300K

	AlN		AlN[e]	GaN		GaN[e]	InN		InN[e]
a_0 (Å)	3.112	3.110	3.103	3.189	3.199	3.189	3.54	3.585	3.560
c_0 (Å)	4.982	4.995	4.980	5.185	5.227	5.188	5.705	5.801	5.713
c_0/a_0	1.601	1.606	1.605	1.627	1.634	1.627	1.612	1.618	1.605
Ref.	[5]	[6]	[6]	[5]	[6]	[6]	[5]	[6]	[6]

2.1.2 Band Structure

The wurtzite nitride semiconductors are direct band gap materials with the conduction band minimum (CBM) and valence band maximum (VBM) occurring at the Γ point, as depicted for wurtzite GaN in Figure 4. The forbidden energy gap of the Al–Ga–In nitrides spans from 0.67 eV of InN through 6.16 eV for AlN (Figure 1, Table 2). The valence band offsets are such that type I, straddling heterojunctions form between these three binaries and their ternary alloys.

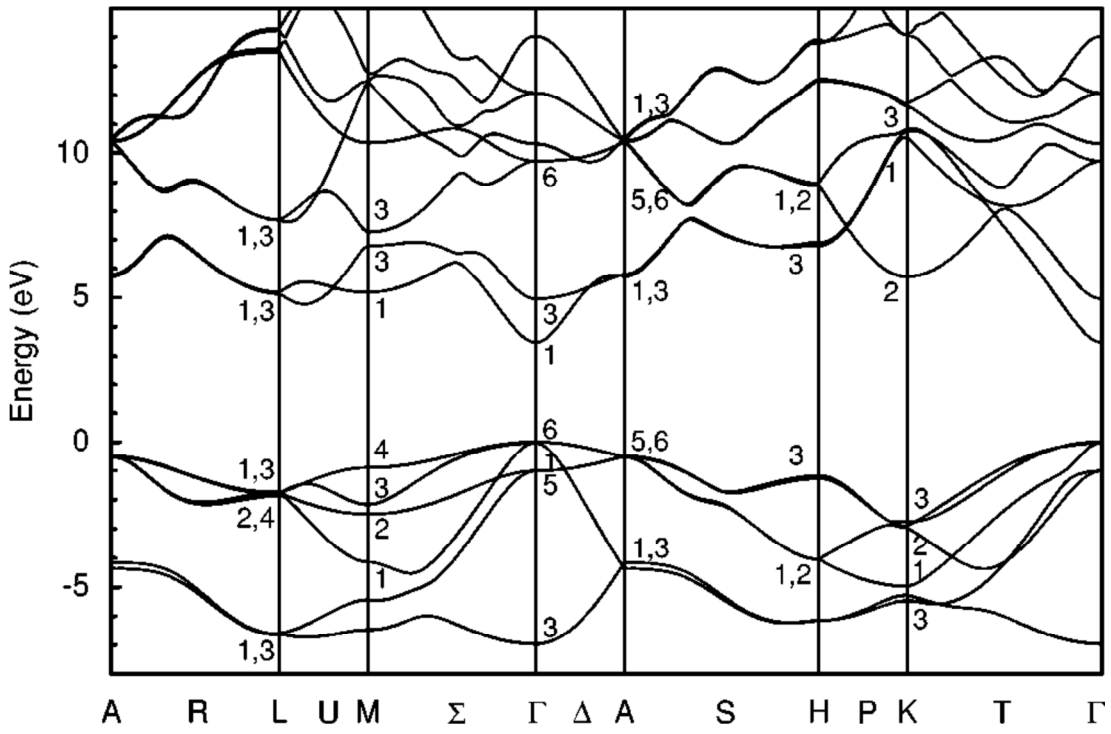

Figure 4. Band structure of wurtzite GaN [7]

Until recently, the band gap of the wurtzite nitride family was understood to have a narrower range. Due to the Burstein-Moss effect [8] – i.e., a dependency of the optical absorption limit on the degeneracy of donor concentration – the empirical band gap of InN was overestimated in 1986 as $\varepsilon_g(300K) = 1.89$ eV [9]. In early 2000 the correct, narrower band gap was established from empirical data and *ab initio* calculations; however, the joint publication was rejected by multiple journals until it was ultimately split into two papers and published in 2002 [10].

The band gap of the nitride ternary alloys may be calculated as:

$$\varepsilon_g^{A(x)B(1-x)N}(x) = \varepsilon_g^{A}\, x + \varepsilon_g^{B}\,(1-x) - b_{\varepsilon g}^{ABN}\, x\,(1-x) \qquad (1)$$

For the ternary alloys of interest, the alloy band gap is smaller than the linear interpolation would suggest; this is reflected by the positive bowing parameters listed in Table 3.

Table 2. Band gap, low-field mobility, breakdown field, relative static dielectric constant, and spontaneous polarization of wurtzite nitrides at 300K

	ε_g (eV)	μ_n (cm²/V s)	E_{crit} (MV/cm)	ϵ_r	P_{sp} (C/m²)
AlN	6.16	135	8.4	8.5	−0.090
GaN	3.42	1,100[1]	3.3	9.5	−0.034
InN	0.67	3,570	1.2	15.3	−0.042
Ref.	[11]	[12]	[12]	[12]	[6]

Table 3. Second-order band gap bowing parameter for wurtzite ternary nitride alloys

	AlGaN	AlInN	InGaN
$b_{\varepsilon g}^{ABN}$ (eV)	0.7 [13]	4.0 [14]	1.72 [15]

2.1.3 Polarization

The wurtzite III–N semiconductors at equilibrium, i.e., in the absence of external forces, exhibit strong polarization arising from a combination of two factors. First, nitrogen is the most electronegative element of the group V elements; therefore, the electron distribution in the III–N covalent bond is distorted toward the nitrogen atom, inducing a polarity in the bond. Secondly, the wurtzite nitrides exhibit a lack of inversion symmetry along the c-axis. The combination of these factors induces a spontaneous polarization in all wurtzite nitrides.

Deviation from the ideal c_0/a_0 ratio of $(8/3)^{½} \approx 1.6330$ toward a lower value in the binary nitrides (Table 1) results in an increasing magnitude of spontaneous polarization from GaN, through InN, to AlN (Table 2). The spontaneous polarization

[1] Here the 2DEG mobility is listed since quantum-confined HEMT structures with 2DEG GaN channels are the topic of this dissertation; the bulk mobility is 990 cm²/V s

for ternary nitrides may be calculated to second order using the values in Table 2 and Table 4:

$$P_{sp}^{A(x)B(1-x)N}(x) = P_{sp}^{A}\, x + P_{sp}^{B}\,(1-x) - b^{ABN}\, x\,(1-x) \quad (2)$$

Due to the lack of inversion symmetry, a polarization-induced fixed charge density forms at the two c-plane faces of the crystal.

Table 4. Second-order bowing parameter for selected wurtzite ternary nitride alloys

	AlGaN	AlInN	InGaN
b^{ABN} (C/m²) [6]	−0.021	−0.070	−0.037

The lattice constant of ternary nitrides may be calculated by applying Vegard's Law to the binary lattice constants in Table 1; for the two ternaries of interest:

$$a(Al_xGa_{1-x}N) = 3.189 - 0.086\, x \quad (3)$$

$$a(Al_xIn_{1-x}N) = 3.560 - 0.457\, x \quad (4)$$

Similarly, the piezoelectric coefficients and elastic constants for the ternary nitrides of arbitrary composition may be approximated by a composition-weighted linear interpolation between the values for the binary nitrides in Table 5.

Biaxial strain in pseudomorphic layer is given by:

$$\varepsilon_1 = \frac{a_0 - a}{a} \quad (5)$$

where, in the case of an $Al_xGa_{1-x}N$/GaN HEMT, the biaxial strain in the pseudomorphic $Al_xGa_{1-x}N$ layer is dependent upon a_0, the lattice constant of the relaxed GaN buffer, and a, the lattice constant of relaxed $Al_xGa_{1-x}N$. The piezoelectric polarization induced by this biaxial strain in wurtzite crystals, neglecting negligible shear stresses, is [6]:

$$P_{\mathrm{pz}} = 2\,\varepsilon_1\left(e_{31} - e_{33}\frac{C_{13}}{C_{33}}\right) \tag{6}$$

where the relevant elastic constants C_{13} and C_{33} and improper piezoelectric coefficients e_{31} and e_{33} are listed for the binary nitrides in Table 5; for the ternary nitrides, a composition-weighted linear interpolation may be used.

Table 5. Spontaneous polarization and hexagonal crystal properties for binary wurtzite nitrides at 300K [6]

	AlN	GaN	InN
e_{31} (C/m²)	−0.53	−0.34	−0.41
e_{33} (C/m²)	1.50	0.67	0.81
C_{13} (GPa)	108	103	92
C_{33} (GPa)	373	405	224

Examining the constants in Table 5, the parenthetical expression in equation (6) is always negative. Consequentially, the piezoelectric polarization along the [0001] direction, or c-axis, is always negative for layers under biaxial tensile strain, such as AlGaN grown pseudomorphically atop GaN. Conversely, the piezoelectric polarization is positive and antiparallel to the spontaneous polarization for Ga-face layers under compressive strain, e.g. for low Al composition AlInN grown on GaN.

While useful for illustrating the above point, equation (6) fails to take into account the nonlinear dependence of piezoelectric polarization on strain; an improved approach developed the following nonlinear dependencies of polarization on strain for the binary nitrides [6]:

$$
\begin{aligned}
P_{pz}^{AlN}(\varepsilon_1) &= -1.808\ \varepsilon + 5.624\ \varepsilon^2 \\
P_{pz}^{AlN}(\varepsilon_1) &= -1.808\ \varepsilon - 7.888\ \varepsilon^2 \\
P_{pz}^{GaN}(\varepsilon_1) &= -0.918\ \varepsilon + 9.541\ \varepsilon^2 \\
P_{pz}^{InN}(\varepsilon_1) &= -1.373\ \varepsilon + 7.559\ \varepsilon^2
\end{aligned}
\tag{7}
$$

The piezoelectric polarization within a binary, strained nitride layer should be calculated using equations (5) and (7). For a pseudomorphically-grown ternary nitride layer, Vegard's Law may be applied and the strain-induced piezoelectric polarization may be interpolated linearly between these composition-dependent binary endpoints.

The use of the spontaneous and piezoelectric polarization to engineer an undoped structure with a high quantum-confined carrier concentration, the HEMT, is discussed in Section 2.5.

2.2 Substrates

The substrate provides mechanical and thermal support to the epitaxial layers grown atop it. Unlike competing technologies including Si, SiC, and GaAs, there are at present no bulk, large-area, i.e., 2" or greater diameter, native substrates for GaN. The production epitaxial growth of wurtzite GaN requires a large-area, commercially-available substrate with a hexagonal surface of similar lattice constant to GaN. Furthermore, for high-field or high-frequency applications, a substrate with high electrical resistivity is important to prevent, respectively, premature breakdown and capacitive loading. For continuous-wave (CW) microwave or high-duty-cycle switching applications, the thermal conductivity of the substrate should be at least that of the GaN buffer.

The GaN HEMT buffer design calls for micron-thick growth of relaxed, i.e., adhering to its bulk lattice constant, GaN. The lattice mismatch of the GaN buffer with respect to the substrate may be calculated as:

$$
LM = (a - a_0) / a_0 \tag{8}
$$

where a and a_0 are the cell dimensions of the GaN buffer and substrate, respectively.

The thermal conductivity, electrical resistivity, lattice mismatch of relaxed GaN growth, diameter of commercially-available material, and relative cost of common substrates for GaN are detailed in Table 6. To date, the substrates of choice for the commercial production of GaN switching and microwave transistors are, respectively, sapphire (α-Al_2O_3) and silicon carbide (SiC).

Table 6. Properties of commercially-available GaN substrates at 300K

Substrate	k (W/cm-K)	ρ (Ω-cm)	Lattice Mismatch	Diameter	Relative Cost
Sapphire	0.4	10^{16}	15%	4"	$
SiC	3.5	10^{6}	3%	4"	$$$
Si	1.5	10^{4} (FZ)	17%	8"	$
SI-GaN	2.25	10^{6}	0%	30 mm	$$$
CVD diamond	12–15	10^{13}–10^{16}	n/a	4"	$$

Given its low cost, high resistivity, and reasonable lattice mismatch, sapphire is an attractive substrate for low duty cycle switching applications. When cooled to 70 K, the thermal conductivity of sapphire rises above 12 W/cm-K [16] and peaks near 30 K in excess of 200 W/cm-K [17]. Thus, sapphire may also be used as a substrate in a laboratory environment for prototyping devices that are then cooled for on-wafer testing and demonstration before transitioning to a SiC or diamond substrate.

Silicon carbide (SiC) offers a thermal conductivity ~80% higher than that of GaN buffers grown epitaxially on a foreign substrate. The low lattice mismatch of relaxed GaN atop SiC facilitates the high-quality, low-dislocation-density growth. The highest microwave output power densities of GaN HEMTs have been reported for SiC

substrates [18]. Lower-cost misoriented SiC substrates have been investigated as a compromise between epitaxial quality and defect density while maintaining the high thermal conductivity of SiC [19].

The thermal conductivity of high-resistivity, float zone (111) Si offers a design compromise between the high thermal conductivity of SiC and the low cost of sapphire. In this work (Chapter 5), the sheet densities for epitaxial layers grown atop (111) Si were consistently lower than the design would suggest or achieve on SiC. Recently, as a testament to improving GaN-on-Si material quality, excellent small-signal performance, including a unity-current-gain frequency f_T = 107 GHz and f_{MAX} = 150 GHz for a 75 nm gate length, has been reported [20].

Another promising platform, semi-insulating (SI), bulk GaN crystals grown by HVPE uniquely facilitate the homoepitaxial growth of GaN epitaxial layers. The benefits include a two order of magnitude reduction in defect density versus GaN-on-Si and will be detailed in Chapter 5. Homoepitaxial GaN is now available in 30 mm HVPE-grown substrates.

In addition to the above substrates on which the GaN buffer is grown, a variety of transferred substrates exist to achieve higher performance than on the as-grown substrate. One example arises from the application of the commercial Smart Cut process, developed for silicon-on-insulator (SOI) technologies, to transfer a thin (111) high-resistivity Si layer onto polycrystalline SiC. The composite substrate is comprised of a 0.2 μm (111) Si growth surface, a 0.1 μm SiO_2 interlayer (k = 0.02 W/cm-K), and a polycrystalline SiC substrate (k = 3 W/cm-K) [21]. Epitaxial layer growth is then achieved by MBE or MOCVD, with devices on the latter exhibiting 5 W/mm output power with 35% P.A.E. biased at 30 V and driven at 10 GHz [22]. SiopSiC offers a promising large-area platform for GaN epitaxy and devices, compromising between the thermal conductivity and cost of Si and crystalline SiC.

Further advancement of GaN HEMTs for high-power applications requires reducing the temperature rise of the devices beyond what has been possible with SiC substrates. A materials solution to mitigate self-heating involves locating the active region of the HEMT device within close proximity to a substrate with high thermal conductivity. Diamond offers the highest isotropic thermal conductivity of any material at room temperature. Three approaches have been pursued to integrate high-power GaN devices onto diamond substrates. In the most direct approach, GaN epitaxial layers were grown atop a 3 × 3 mm crystalline diamond substrate [23] demonstrating a sheet density of $n_s = 1.3 \times 10^{13}$ cm^{-2}, mobility of $\mu_H = 731$ cm^2/Vs, and current density $I_{Dmax} = 0.73$ A/mm [24]. At present, the scalability of this approach is limited by the small area, prohibitive cost, and lengthy growth times for such crystalline diamond substrates.

Although not as high as crystalline diamond, the thermal conductivity of chemical vapor deposition (CVD) polycrystalline diamond is 3–4 times that of SiC. In commercial development of a diamond coating process developed by the Naval Research Labs, sp3 Inc. has demonstrated AlGaN/GaN HEMTs on Si-on-diamond (SOD) substrates at 100 mm diameter [25]. The substrate formation begins with a FZ Si wafer upon which CVD diamond is grown up to 50 μm thickness. The (111) Si substrate is then ground to a thin (0.5–2 μm) seed layer upon which the GaN epitaxial layers may be grown [26]. To facilitate fabrication of a thin, large-area wafer, a ~500 μm Si handle wafer is attached to the backside of the material stack and removed subsequent to fabrication [27]. This approach is limited by the relatively thick Si interlayer in addition to the GaN buffer layer through which more than half of the temperature rise in the structure is evolved before reaching the relatively thin diamond heat-spreading layer.

In an enhancement to this process, AlGaN/GaN layers are first grown on a Si substrate. The surface is coated with 10 nm SiN_x upon which polycrystalline diamond is seeded and grown to a thickness of 10 μm [28]. Such an epitaxial transfer process provides a means to achieve high-quality N-face GaN epitaxial layers, traditionally difficult to grow, by flipping the superior Ga-face-grown epitaxy. This approach facilitates ohmic contact formation, improves electron confinement at pinch-off, and increases ion implantation activation yield [29]. The greatest improvement compared to the standard sp3 Inc. Ga-face wafer preparation is that this epi-inverted process places the diamond heat spreader within 30 nm of the 2DEG.

Group4 Labs has developed a method to atomically attach AlGaN/GaN epitaxial layers to polycrystalline diamond substrates, presently at 4" diameters [30]. Organometallic Vapor Phase Epitaxy (OMVPE) AlGaN/GaN is grown epitaxially on a silicon substrate, the material is then flipped and mounted to a carrier, and the substrate is etched away. The exposed GaN surface is treated with a proprietary dielectric coating and the epitaxial layer is atomically attached to CVD polycrystalline diamond. Finally, the carrier wafer is etched from the front side of the epitaxial layer.

In summary, although there is at present no large-area native substrate for GaN, continuous improvements in low-defect-density GaN-on-Si templates as well as the increasing area of bulk SI GaN coupled with the thermal approaches of engineered diamond substrates provide design choices for GaN power devices for diverse applications.

2.3 Growth Techniques

The two most common techniques for the epitaxial growth of nitride layers are Metal Organic Chemical Vapor Deposition (MOCVD) and Molecular Beam Epitaxy (MBE). MOVCD offers faster growth rates and larger-area reactors than available by

MBE at the cost of higher growth temperatures ~1100°C. An additional disadvantage is the positive correlation between buffer resistivity and growth temperature, resulting in a trade-off between buffer resistivity and surface morphology [12].

MBE growth occurs at a lower temperature, ~800°C, and offers precise precursor control for sharp compositional interfaces and in-situ monitoring of growth rate and composition (by X-Ray Diffraction, or XRD) and crystallinity (by Reflection High Energy Electron Diffraction, or RHEED).

2.4 Dislocations

When GaN is grown epitaxially on lattice-mismatched substrates such as sapphire and SiC, strain is introduced. This lattice mismatch between disparate materials is naturally accompanied by a mismatch between the coefficients of thermal expansion. For example, GaN-on-sapphire exhibits a 14% mismatch in lattice spacing and a 34% mismatch in thermal expansion coefficient at room temperature [31]. Resulting from these disparities, a high density of dislocations is present in relaxed, epitaxially-grown GaN layers. The high concentration of defects in GaN adversely impacts carrier transport.

Dislocations may occur in the form of edge, screw, or mixed dislocations, the last of which is a combination of the preceding two. Dislocations may be represented by a Burgers vector, which indicates the lattice displacement from a perfect crystal induced by a dislocation. The Burgers vectors for edge and screw dislocations are, respectively, orthogonal and parallel to the given dislocation line.

Edge dislocations arise from what may be considered a prematurely terminating plane, introducing strain into the surrounding crystal and perturbing its periodic potential. Similarly, screw dislocations arise from a partial mismatch in crystal plane spacings such that following the planes near the dislocation would be

akin to tracing the threading on a screw. Screw dislocations have been found to occur with three different atomic core structures: full core, filled core, and open core [32]. The literature agrees that these cores are often comprised of eight atoms, an excess of two atoms over the typical hexagonal arrangement. Mixed dislocations, also comprised of eight-atom cores, have been experimentally and theoretically shown to structurally reorder into partial edge and screw dislocations plus a stacking fault with the span of a few atomic lengths [32].

Edge dislocations oriented along the [0001] growth axis tend to span the depth of the GaN epitaxial layer, while screw and mixed dislocations reduce in density along the growth direction [33]. Therefore, considering a 2DEG in an AlGaN/GaN HEMT structure, the effect of edge dislocations is of greatest concern.

Edge and screw dislocations in GaN grown epitaxially in the [0001] direction may be modeled as lines of charge. In a large band gap semiconductor, the trap levels introduced by the dangling bonds found in dislocations may be considered to act as acceptor sites [33]. These acceptor levels are mostly filled in the presence of a high carrier concentration and can be considered to reduce the effective band gap. Thus, they are associated with leakage current, which induces premature breakdown in devices under reverse bias conditions. Since the trap sites are spaced equally along the dislocation line separated by inter-planar lattice constant c, the energy levels of these closely-spaced traps begin to disperse over a range of quantized energies.

Considering the effect of dislocations on electron transport, for a small electric field the drift velocity is proportional to the field and related by the drift mobility; viz.

$$\boldsymbol{v}_{\mathrm{d}} = -\mu \boldsymbol{E} \tag{9}$$

Implementing the approximation of isotropic effective mass $m^{\star}$, the relationship between mobility and the momentum relaxation time, τ_{m}, becomes:

$$\mu = q \langle \tau_{\mathrm{m}} \rangle / m^{\star} \tag{10}$$

Ionized impurity scattering in GaN may be approximated by the Brooks-Herring equation, which states that the momentum relaxation time due to ionized impurity scattering is inversely proportional to the ionized impurity concentration. In unintentionally doped structures, such as the AlGaN/GaN HEMT whose 2DEG arises from polarization, the ionized impurity concentration is low. Applying Matthiessen's rule:

$$\frac{1}{\tau_{\mathrm{m}}} = \sum_{i} \tau_i \tag{11}$$

to (10), we develop an expression for the dependency of mobility on its components arising from dislocation scattering, μ_{dis}; ionized impurity scattering, μ_{ii}; and all other lattice scattering mechanisms, μ_{lat}:

$$\frac{1}{\mu} = \frac{1}{\mu_{\mathrm{dis}}} + \frac{1}{\mu_{\mathrm{ii}}} + \frac{1}{\mu_{\mathrm{lat}}} \tag{12}$$

Particularly in an environment with high dislocation density, N_{dis}, the contribution to the momentum relaxation time due to ionized impurity scattering may be neglected. In the low-dimensional case of a 2DEG, this may be approximated as:

$$\frac{1}{\mu} = \frac{1}{\mu_{\mathrm{dis}}} + \frac{1}{\mu_{\mathrm{lat}}} \tag{13}$$

Intuitively, an increase in carrier concentration would be expected to increase lattice scattering and thus decrease overall mobility. However, at carrier densities below $10^{17}/\mathrm{cm}^2$, it is observed that mobility increases under such conditions [31]. Inspired by the computations by [33] and in agreement with those of [31], the momentum relaxation time due to dislocation scattering may be expressed as:

$$\tau_{\mathrm{dis}} = \frac{\hbar^3\, \epsilon^2\, c^2}{m^*\, N_{\mathrm{dis}}\, q^4\, f^2} \frac{(1 + 4\, k_{\mathrm{t}}^2\, \lambda^2)^{3/2}}{\lambda^4} \tag{14}$$

where f is the fraction of filled traps and $(2\ k_t\ \lambda)^2$ describes the transverse component of the electron kinetic energy. Screening of dislocation scattering is described by the Debye screening length:

$$\lambda = \sqrt{\frac{\epsilon\ k\ T}{q^2\ n'}} \tag{15}$$

where n' is the carrier concentration:

$$n' = n + (n + N_A)\left(1 - \frac{n + N_A}{N_D}\right) \tag{16}$$

and where N_D and N_A represent bulk concentrations [31]. Note that the carrier concentration in the screening term (15) results in the unexpected relationship between increasing carrier concentration and increasing mobility due to dislocation scattering.

When analyzing the lower-dimensional case of an ideal 2DEG, i.e., a single atomic plane, screening from the charged dislocation lines orthogonal to the 2DEG plane must be taken into account [34]. In that case, a screening factor for the 2DEG was used to derive the momentum relaxation time due to dislocation scattering in a 2DEG, viz.

$$\mu_{dis}^{2DEG} \propto \frac{n_s^{3/2}}{N_{dis}} \tag{17}$$

Consistent with this result, it was determined from numerical comparison between two- and three-dimensional mobilities that the two-dimensional case is comparatively insensitive to dislocation scattering. Particularly at lower carrier concentrations, where dislocation scattering dominates, the two-dimensional structure offers performance benefits over the bulk structure. For this reason, nitride HEMTs offer relatively high electron mobilities, despite high dislocation densities.

In the case of AlGaN/GaN HEMTs with a 2DEG carrier concentration on the order of $n_s \sim 10^{13}/cm^2$, the effective three-dimensional concentration would be on the order of $N \sim 10^{20}/cm^3$, assuming a 2DEG thickness of 25 Å. As documented in [33], essentially all of the dislocation-induced traps in GaN are filled at such a high carrier concentration. In this quantum-confined case, the mobility is limited primarily by lattice scattering.

Dislocations common in GaN structures have been demonstrated to reduce the drift mobility in devices. Dislocation scattering, dominant at lower carrier concentrations, is responsible for the relationship between increasing carrier concentration and increasing mobility. By reducing the dislocation densities through improved growth techniques, mobilities due to dislocation scattering will increase without additional inhibition by lattice scattering, resulting in an overall higher mobility. The development of bulk GaN as a lattice-matched substrate may pave the way for higher mobilities (and higher performance devices), particularly at lower carrier concentrations.

2.5 HEMT Electrical Properties

The High-Electron-Mobility transistor (HEMT) is a Heterostructure Field Effect Transistor (HFET) featuring a quantum-confined electron channel. The polarization-induced fixed charge densities at c-plane surfaces of nitride semiconductors may be utilized to evolve a quantum-confined Two-Dimensional Electron Gas (2DEG) at a nitride heterojunction. This is a contrast to AlGaAs/GaAs HEMTs which require doping to provide electrons to the 2DEG potential well [35].

Consider the simple case of a pseudomorphic, strained $Al_xGa_{1-x}N$ barrier layer grown atop a relaxed GaN buffer. The total polarization in each layer is the sum of its

spontaneous and piezoelectric polarization vectors. The fixed-charge density is related to the electric polarization as:

$$\rho = -\nabla \cdot \boldsymbol{P} \tag{18}$$

By integrating equation (18) along the c-axis, which does not exhibit inversion symmetry, we obtain the fixed sheet charge density:

$$\sigma = -\boldsymbol{P} \tag{19}$$

At each c-plane surface and at the $Al_xGa_{1-x}N$/GaN heterojunction there is an abrupt change in polarization which evolves a fixed, planar interface charge density given by [6]:

$$\sigma_{\mathrm{AlGaN/GaN}} = P_{\mathrm{GaN}} - P_{\mathrm{AlGaN}} = (P_{\mathrm{sp,GaN}} + P_{\mathrm{pz,GaN}}) - (P_{\mathrm{sp,AlGaN}} + P_{\mathrm{pz,AlGaN}}) \tag{20}$$

Thus, for the example $Al_xGa_{1-x}N$/GaN, the relaxed GaN layer implies $P_{\mathrm{pz,GaN}} = 0$. The calculation of the spontaneous-induced, piezoelectric-induced, and total fixed charge densities at the interface are presented in Figure 5 for $Al_xGa_{1-x}N$/GaN and $Al_xIn_{1-x}N$/GaN heterojunctions. In the latter structure for aluminum compositions $x < 83\%$, the piezoelectric polarization vector is antiparallel to the spontaneous polarization vector. Below a 70% Al mole fraction, the piezoelectric contribution dominates and the fixed interface charge changes polarity; this regime is not plotted in Figure 5 as it is not germane to the device designs explored in this work.

The offset of the conduction bands coupled with the polarization-induced charge at a Ga-face $Al_xGa_{1-x}N$/GaN heterojunction establishes a triangular quantum well [36] within the GaN at the interface. The electrons are confined in a high concentration to this two-dimensional electron gas (2DEG). For such an undoped structure, the induced 2DEG sheet charge density is given by [37]:

$$n_{\mathrm{s}}(x) = \frac{\sigma(x)}{q} - \frac{\epsilon_0 \epsilon_{\mathrm{r}}(x)}{d\, q^2}\left[q\, \phi_{\mathrm{SB}}(x) + \varepsilon_{\mathrm{f\text{-}c}}(n_s) - \Delta\varepsilon_{\mathrm{c}}(x)\right] \tag{21}$$

where $\epsilon_0\epsilon_r(x)$ is the permittivity of the $Al_xGa_{1-x}N$ barrier of thickness d; Φ_{SB} is the Schottky barrier height; $\varepsilon_{f-c}(n_s)$ is the energy of the Fermi level above the GaN conduction band edge at the $Al_xGa_{1-x}N$/GaN interface; and $\Delta\varepsilon_c(x)$ is the height of the conduction band discontinuity at the interface.

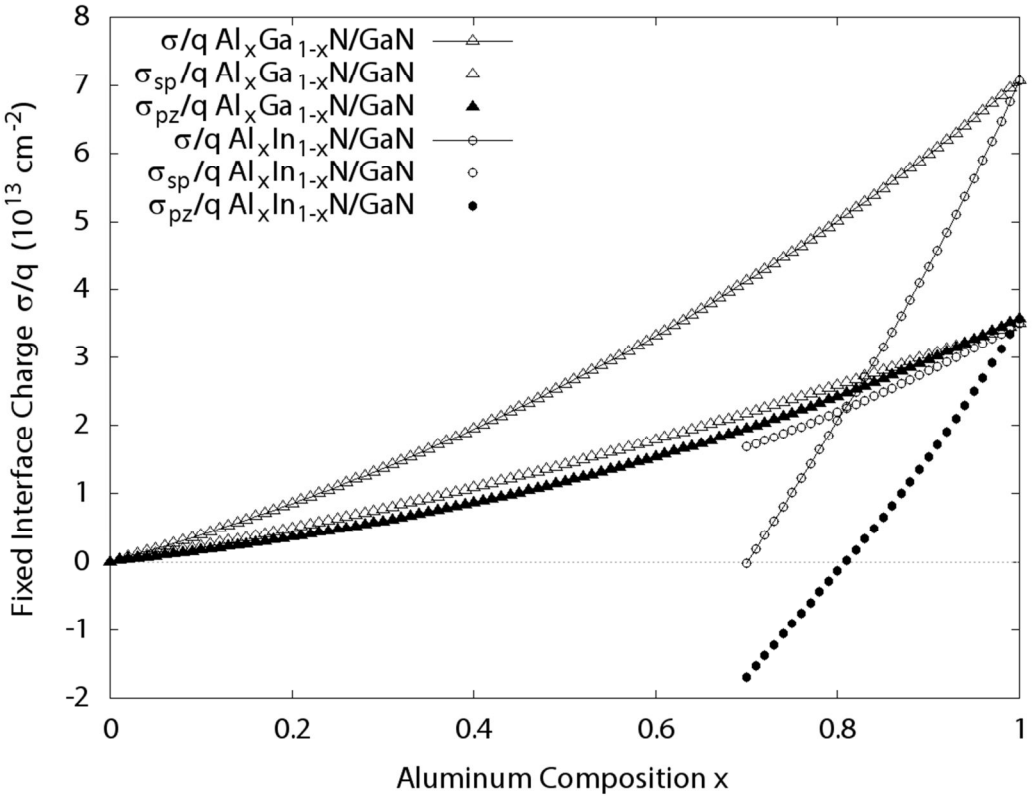

Figure 5. Fixed interface charge density evolved at an Al(Ga,In)N/GaN heterojunction; the spontaneous and piezoelectric components of the total charge density are indicated

The relative static dielectric constant of ternary nitrides of interest is approximated by the composition-weighted average:

$$\epsilon_r^{ABN}(x) = \epsilon_r^{AN}(x) + \epsilon_r^{BN}(1-x) \tag{22}$$

where the relative static permittivities for the binary Wurtzite nitrides are listed in Table 2. Unlike earlier data [38] for which the static relative permittivity $\epsilon_r^{AlN} > \epsilon_r^{GaN}$,

the latest data compiled in [12] follow the trend of the dielectric constant increasing with atomic size.

In AlGaAs/GaAs heterostructures, the relationship between the conduction and valence band discontinuities at the heterojunction is $\Delta\varepsilon_c$:$\Delta\varepsilon_v$ ~ 60:40 [39]. An early report for the AlGaN material system suggests the applicability of a similar 67:33 rule to AlN/GaN interfaces [40]. More recently, publications suggest that 63% [6] or 70% [12] of the band gap discontinuity at an AlGaN/GaN heterojunction occurs within the conduction band, viz.

$$\Delta\varepsilon_c \approx 0.63[\varepsilon_g^{\mathrm{Al}(x)\mathrm{Ga}(1-x)\mathrm{N/GaN}}(x) - \varepsilon_g^{\mathrm{GaN}}] \tag{23}$$

As can be seen in Figure 6, for ternary nitrides, the composition-dependent conduction band minimum (CBM) and valence band maximum (VBM) energies vary asymmetrically. In particular, the CBM for the ternary nitrides bows far more strongly than the VBM. While the 63% rule in equation (23) may provide a first-order approximation of the conduction band discontinuity between GaN and AlGaN, such a rule does not provide a reasonable approximation for the more strongly bowed $Al_xIn_{1-x}N$ layers. Thus, the conduction band offset at a heterojunction must be calculated based on the interpolation between empirical binary valence band offsets [11] and the composition-dependent band gap calculated using equation (1). The calculated conduction band offset for $Al_xGa_{1-x}N$/GaN and $Al_xIn_{1-x}N$/GaN interfaces and the simple approximation for the former given by equation (23) are plotted in Figure 7.

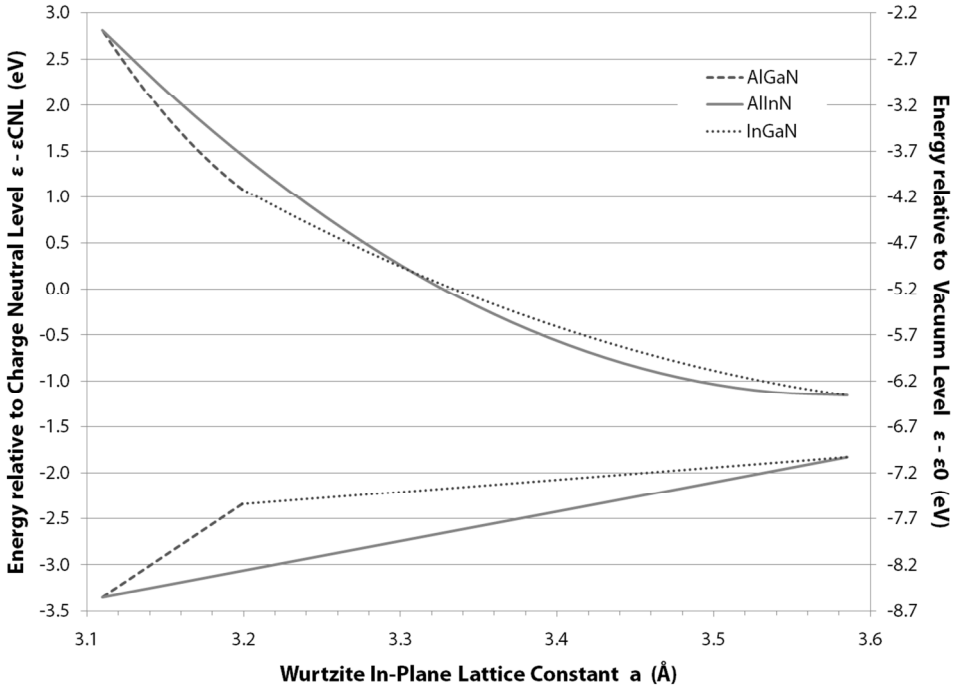

Figure 6. CBM and VBM energy as a function of lattice constant for all compositions of ternary nitrides at 300K

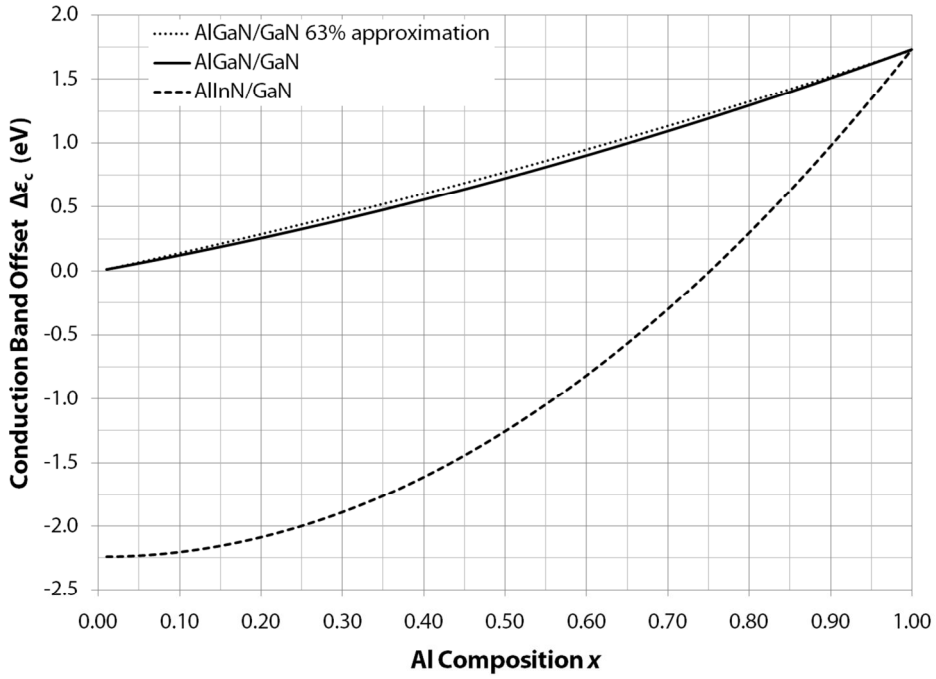

Figure 7. Conduction band discontinuity for nitride heterojunctions at 300K

Consider an example of a heterostructure consisting, from the bottom up, of a relaxed GaN buffer, a 175 Å $Al_{0.26}Ga_{0.74}N$ barrier, and a 20 Å GaN cap layer. The conduction band edge for this structure is plotted at pinch-off, for which the 2DEG is fully depleted, in Figure 8. The conduction band discontinuities are calculated using equation (23), and the Schottky barrier height of Ni, in the general case, on $Al_xGa_{1-x}N$ is approximated as:

$$\Phi_{SB} \approx 1.0 + 1.9\,x \tag{24}$$

The net polarization-induced charge density at the $Al_xGa_{1-x}N$/GaN heterojunction is calculated using equation (20). Gauss' Law relates the piezoelectric charge density to the resultant electric field:

$$\nabla \cdot \boldsymbol{E} = \frac{\rho}{\epsilon} \tag{25}$$

Substituting (18) into (25) and integrating along the c-axis, we find:

$$E = \frac{\sigma}{\epsilon} \tag{26}$$

Applying Gauss' Law, we can calculate the net electric field within the pseudomorphic $Al_xGa_{1-x}N$ barrier layer. In this example, the Fermi level of the Schottky contact is 3.0 eV above the Fermi level at the AlGaN/GaN heterojunction where the 2DEG is fully depleted.

Taking the threshold voltage from this conduction band edge at pinch-off, the sheet charge density may be approximated using equation (26) and employing the relationship between electron density and charge density $n = \sigma/q$:

$$n_{s0} \approx \frac{E\,\epsilon_0\,\epsilon_r}{q} \tag{27}$$

Thus, the sheet charge at zero bias n_{s0} may be approximated by the calculated threshold voltage E (V/cm), the elementary charge $q = 1.602\times10^{-19}$ C, the permittivity of free space ϵ_0, and the relative dielectric constant approximated by (22).

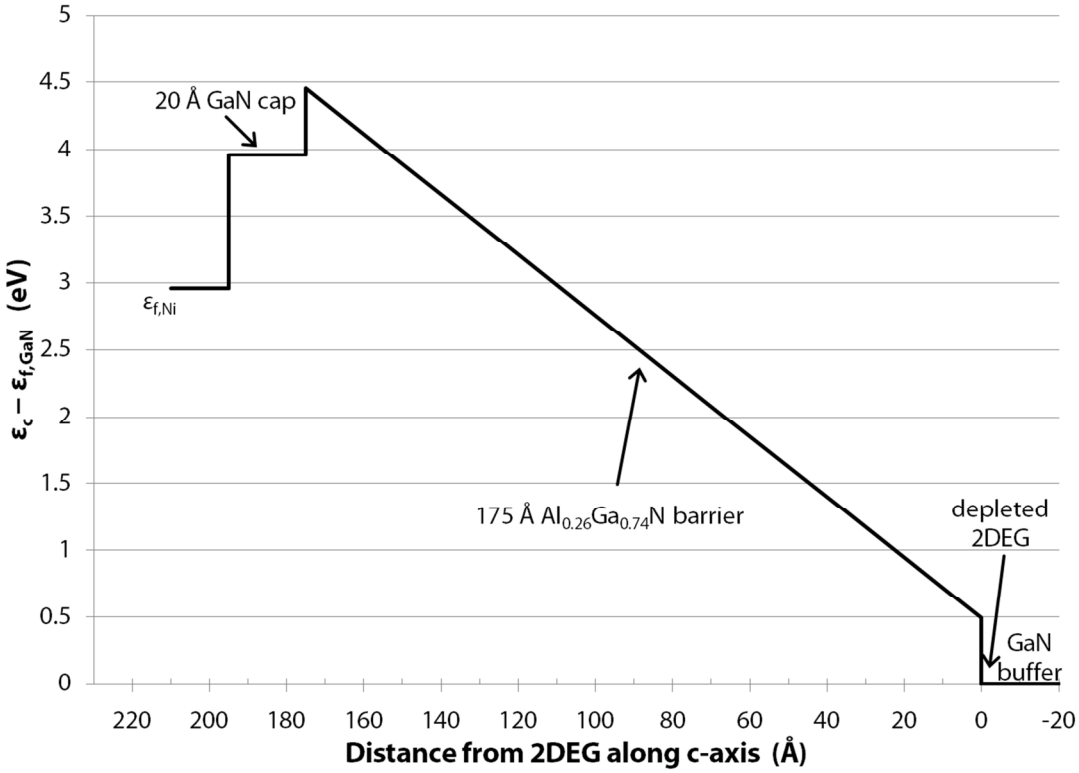

Figure 8. Conduction band edge of an AlGaN/GaN HEMT structure

Returning to the structure in Figure 8, the electric field may be calculated as the threshold voltage at pinch-off, 3.0 V, over 208 Å from the Schottky contact to the center of the 2DEG; in this case, the 2DEG charge density is approximated using (27) as $n_s = 6.7\times10^{12}/\text{cm}^2$.

To accurately estimate the carrier distribution in such a quantum-confined structure, a self-consistent Schrödinger-Poisson solver must be used. Applying the one-dimensional coupled Schrödinger-Poisson solver C-BAND [41] to the above example, a zero-bias sheet density of $n_s = 7.7\times10^{12}/\text{cm}^2$ is calculated.

The aforementioned theories may be applied to the development of high-power, high-frequency GaN HEMTs.

CHAPTER 3: HEMT DESIGN AND FABRICATION

3.1 Epitaxial Layers

The first step in the design of a HEMT is determining the epitaxial layer structure of the device. As discussed in Chapter 2, the device is designed such that a high-density sheet charge evolves at the top of the GaN buffer layer, leveraging the high mobility and critical field of GaN. The buffer is typically grown to a thickness of ~2 μm to reduce the dislocation density at the 2DEG. The barrier layer above the channel is designed to leverage the strong polarization in the nitrides, discussed in Chapter 2, to elicit electrons into the 2DEG without the need for doping, which would reduce carrier mobility. With the exception of lattice-matched $Al_{0.83}In_{0.17}N$/GaN heterojunctions, thin ternary nitrides atop GaN are grown under strain. The growth of pseudomorphically strained layers is limited by a critical thickness, beyond which micro- or macroscopic cracking occurs. The thickness of $Al_xGa_{1-x}N$ layers grown pseudomorphically atop relaxed GaN buffers must satisfy the empirical limit:

$$\Sigma(d_{\mathrm{Al}(x)\mathrm{Ga}(1-x)\mathrm{N}}/d_{\mathrm{crit}}(x)) < 1 \tag{28}$$

A summary of the composition dependence of the critical thickness d_{crit} is found in [5]; for $Al_xGa_{1-x}N$ barrier compositions of particular interest, the critical thickness $d_{\mathrm{crit}}(0.38 \pm 0.03) = 300 \pm 50$ Å. For an MBE-grown AlN interbarrier, the $d_{\mathrm{crit}}(1) = 49$ Å. $Al_xIn_{1-x}N$ is lattice-matched to GaN at an aluminum composition of $x = 83\%$; as such, thick unstrained layers may be grown atop GaN, limited by the mismatch in the coefficient of thermal expansion between the materials. Such lattice-matched layers have been grown beyond 500 nm thickness [42]. When designing an $Al_xIn_{1-x}N$/GaN HEMT, a mole fraction $x > 83\%$ may be desirable to enhance carrier concentration. In the extreme case the growth of AlN is limited by (28) to a critical thickness of 49 Å.

The inclusion of an AlN interbarrier increases the polarization-induced sheet charge density within the 2DEG. Recalling Figure 5, the AlN/GaN heterointerface gives rise to the largest fixed, positive polarization charge possible in the wurtzite III-N/GaN material system. Additionally, the ~1.9 eV conduction band offset at the AlN/GaN interface and the increased effective mass in the AlN reduce wavefunction penetration into the barrier, increasing hot-electron confinement within the channel and improving mobility. Furthermore, the abrupt, binary AlN/GaN heterojunction provides a more uniform Coulombic potential than a ternary–GaN interface, further increasing mobility.

For the two material structures presented in Figure 9, which differ only by the inclusion of an AlN interbarrier, the calculated parameters are presented in Table 7. These are the epitaxial layers investigated on GaN-on-diamond in Chapter 5, in which good agreement is demonstrated against device results. The zero-bias sheet densities n_{s0} and threshold voltages V_t are estimated using the electrostatic, classical approximation in equation (27). The sheet densities under zero-bias and full-channel conditions, the latter approximated at +1 V_{GS}, are calculated using semi-classical and quantum-mechanical techniques in [41]. Note that the quantum-mechanically calculated sheet densities are slightly lower since the ground-state quantized sub-band ε_0 is at a finite energy above the bottom of the triangular quantum well.

The growth of a GaN cap layer improves ohmic contact formation, as GaN exhibits a smaller band gap than AlGaN alloys and is chemically less reactive than surface layers, including aluminum. Additionally, the growth of a 20 Å cap GaN layer reduces tunneling current through the Schottky by more than two orders of magnitude [43]. The thickness of the cap layer must be limited, as it increases the overall barrier thickness and, as such, reduces the 2DEG density and HEMT frequency performance. Typically a thickness of 20–40 Å is chosen.

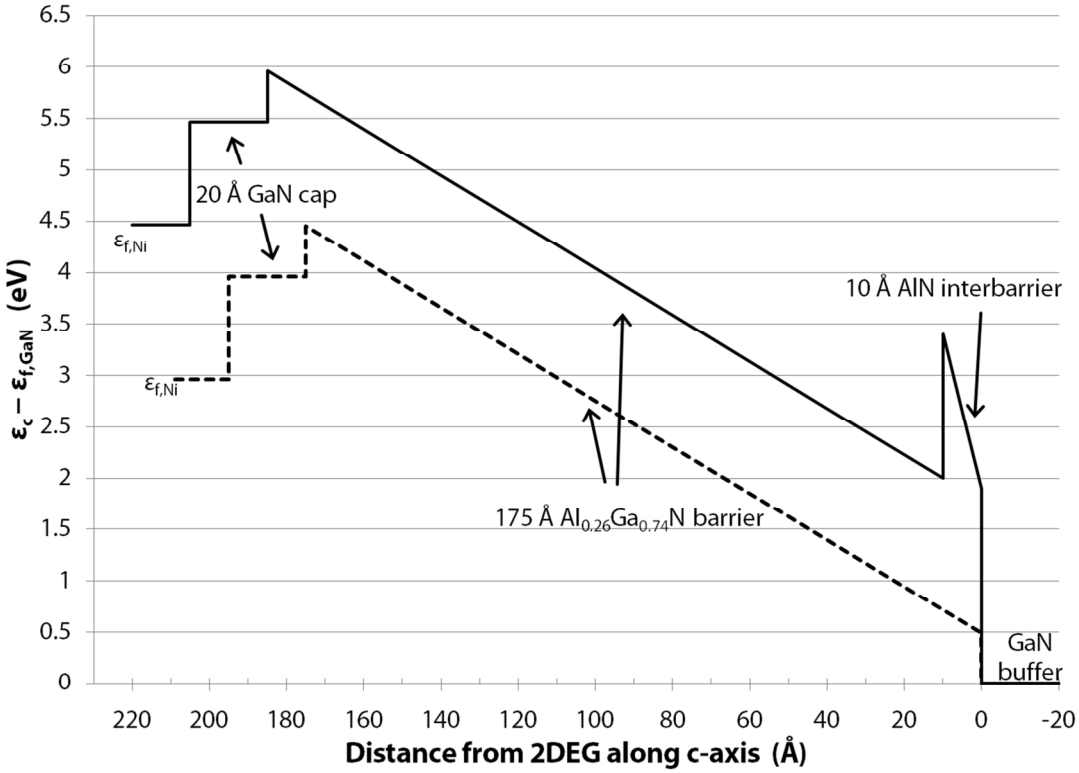

Figure 9. Conduction band edge of an AlGaN/GaN HEMT structure with (solid) and without (dashed) an AlN interbarrier

Table 7. Calculated threshold voltage and zero-bias and full-channel 2DEG sheet density for GaN-on-diamond HEMTs with and without an AlN interbarrier

Method	AlN	V_t (V)	n_{s0} (10^{13}/cm^2)	n_s (10^{13}/cm^2)	Buffer Penetration
Classical	N	−3.0	0.67		
	Y	−4.5	0.96		
Semi-classical	N	-2.9	0.71	0.97	
	Y	-4.3	0.93	1.18	
Quantum	N	-3.1	0.58	0.77	12%
mechanical	Y	-4.5	0.79	0.95	2%

MBE growth is capable of the abrupt heterojunctions necessary for the thin AlN interbarrier and GaN cap layers. It is far more challenging to grow an abrupt interfaces by MOCVD, particularly when the precursors change, as is the case for GaN/$Al_xIn_{1-x}N$ heterojunctions. Thus, some of the HEMT epitaxial layers investigated in this work do not include an AlN interbarrier or GaN cap layer, even though the inclusion of both is preferred.

3.2 AlInN Barriers

The ability to grow unstrained, lattice-matched $Al_{0.83}In_{0.17}N$/GaN layers allows $Al_xIn_{1-x}N$/GaN heterojunctions to achieve higher polarization densities than possible in the $Al_xGa_{1-x}N$/GaN material system, the latter of which is limited by critical layer thicknesses. Deviating slightly toward the Al-rich case of the lattice-matched $Al_xIn_{1-x}N$/GaN engineers additional piezoelectric polarization-induced charge at the interface. Ultimately, it is possible to achieve higher sheet densities using $Al_xIn_{1-x}N$ barriers than is possible using typical mole fractions and thicknesses of $Al_xGa_{1-x}N$.

Due to the higher polarization-induced fixed charge densities, the electric field strength at pinch-off within $Al_xIn_{1-x}N$ barriers for $x \approx 85\%$ is twice as great as achieved in $Al_xGa_{1-x}N$ for $x \approx 26\%$. As a result, the probability of electron tunneling through the Schottky gate barrier is greatly increased. Thus, the growth of a GaN cap layer, which reduces the tunneling probability, is even more essential for $Al_xIn_{1-x}N$ barrier HEMTs.

3.3 Surface Passivation

Given a 2DEG free charge density on the order of 10^{13} cm^{-2}, charge neutrality within the barrier dictates the formation of a large, positive compensating charge density at the surface. Passivation renders these surface states benign, mitigating their effect on the electron transport of the HEMT, including surface hopping and the

virtual gate effect [44]. Furthermore, the surface passivation is typically tens of nanometers thick, which relocates the net surface charge several barrier thicknesses away from the 2DEG, recovering any reduction to the 2DEG density caused by surface depletion. An amorphous SiN_x layer reduces dc–rf dispersion and increases breakdown voltage by an average of 25% [45]. Although small-signal performance decreases due to the capacitive loading of the passivation layer, the rf current recovery more than compensates for this reduction and results in increased output power. This SiN_x layer is blanket-deposited across the wafer at above 300°C and later etched to form electrical contact to the devices. Within this work, a lift-off Atomic Layer Deposition (ALD) Al_2O_3 passivation process was implemented, which allows selective patterning of only the active regions of the device.

3.4 Process Technology

The samples processed in this dissertation were typically squares between 10 mm and 15 mm per side. To protect the surface during dicing, the wafers were coated with 1.2 μm PMMA. To ensure a clean epitaxial surface for fabrication, the PMMA was stripped in methylene chloride or an ultrasonic acetone treatment. In the case of polycrystalline diamond substrates, traditional sawing or scribing techniques applied to crystalline substrates were impractical. Therefore, the GaN-on-diamond samples were diced using a high-power, pulsed Nd:YAG laser in an oxygen atmosphere. The O_2 atmosphere favored the burning of the diamond over the ablation of graphite which would contaminate the epitaxial surface.

This HEMT process was developed to accommodate AlGaN/GaN layers on 25 μm-thick polycrystalline diamond substrates which bowed on the order of 50 μm over 1 cm^2. The bow precluded the use of an optical lithography stepper and the area of the sample was too small to align using available contact lithography tools.

Therefore, a process was developed around the Leica VB-6HR electron beam system, which exhibits a 60 μm depth of field, sufficient for patterning 100 nm gates atop bowed diamond substrates. To facilitate processing, the 25–40 μm-thick GaN-on-diamond wafers were mounted to a 15 mm × 15 mm carrier using Crystalbond 509 adhesive and dismounted before each processing step that exceeded 170 °C temperature. Subsequent 70–100 μm-thick GaN-on-diamond wafers were processed entirely freestanding.

3.4.1 Alignment Marks

The first step in the lithography process is the deposition and lift-off of alignment marks on the bare wafer for all subsequent process steps. Thus, every layer of HEMT lithography is aligned to the same reference plane, which is important because overlay inaccuracies have been observed to occur in the same direction. The metallization of the alignment marks must exhibit good adhesion, thermal stability and high contrast for accurate detection by the tool. The alignment marks must not creep or deform during high-temperature processing to allow the tool to accurately locate the mark edges. It is possible to deposit alignment marks in the same lithography level as ohmic contacts; however, these marks must then be encased in SiN prior to high-temperature annealing to prevent metal creep. This strategy does not work in the case of bulk GaN substrates, which produce increased electron backscatter; for these substrates, a high-Z metal is necessary to provide sufficient contrast for mark detection. Thus, the preferred alignment mark is 25 nm Ti to provide adhesion followed by 175 nm Pt to provide thermal stability and high contrast.

3.4.2 Ohmic Metallization

Ohmic contacts are low-resistance metal-semiconductor junctions exhibiting a linear low-field I–V relationship. In the case of contacts to n-type material, ohmic contact is achieved by minimizing the Schottky barrier or decreasing the work function of the (alloyed) contact metal.

Non-alloyed contact to the 2DEG of a UID AlGaN/GaN heterostructure has been demonstrated using gallium (Ga) and wet silver (Ag) paint to achieve ohmic and Schottky contact, respectively [46]. In this case, the contact resistance is greater than 20 Ω mm, which is useful for process monitoring, but not for high-efficiency transistors. The achievement of non-alloyed contacts to AlGaN/GaN heterojunctions suggests the contact mechanism to be a combination of thermionic emission and thermionic field emission.

To minimize contact resistance and control surface morphology, alloyed contacts based on a four-metal Ti/Al/metal/Au scheme are necessary [47]. Optimized Ti/Al/Mo/Au contacts on AlGaN/GaN material [48] are rectifying, i.e., they exhibit a nonlinear $\delta I/\delta V$ characteristic, prior to high-temperature anneal. The quality, including contact resistance and stability of the post-anneal alloyed contact is a function of temperature and time that a particular metal stack is subjected to a Rapid Thermal Anneal (RTA).

During the anneal, nitrogen diffuses from the AlGaN toward the metal layer [49]. Nitrogen vacancies in the AlGaN barrier layer act as donors. As the nitrogen vacancy density increases, tunneling becomes the dominant mechanism for ohmic contact formation [50]. This trend of contact resistance decreasing as the dopant concentration increases and the depletion region thins is illustrated for the case of ohmic contact to highly-doped GaN layers in Figure 10. For such highly-doped n^{++} GaN, optimal ohmic contact is achieved using nonalloyed Ti/Al/Mo/Au contacts, in

this case, achieving an ultra-low contact resistance of 0.0023 Ω mm and a specific contact resistance of 5.86×10^{-9} Ω cm^2 with a correlation coefficient of $R^2 = 0.9995$ across the sample. Unfortunately, the inclusion of a highly-doped layer above the HEMT barrier would perniciously affect Schottky contact formation and is thus incompatible with a planar HEMT fabrication process. Thus, for the case of GaN HEMTs, nitrogen out-diffusion and alloy formation are the principal methods of ohmic contact formation, and contact resistances below 1.0 Ω mm are deemed reasonable.

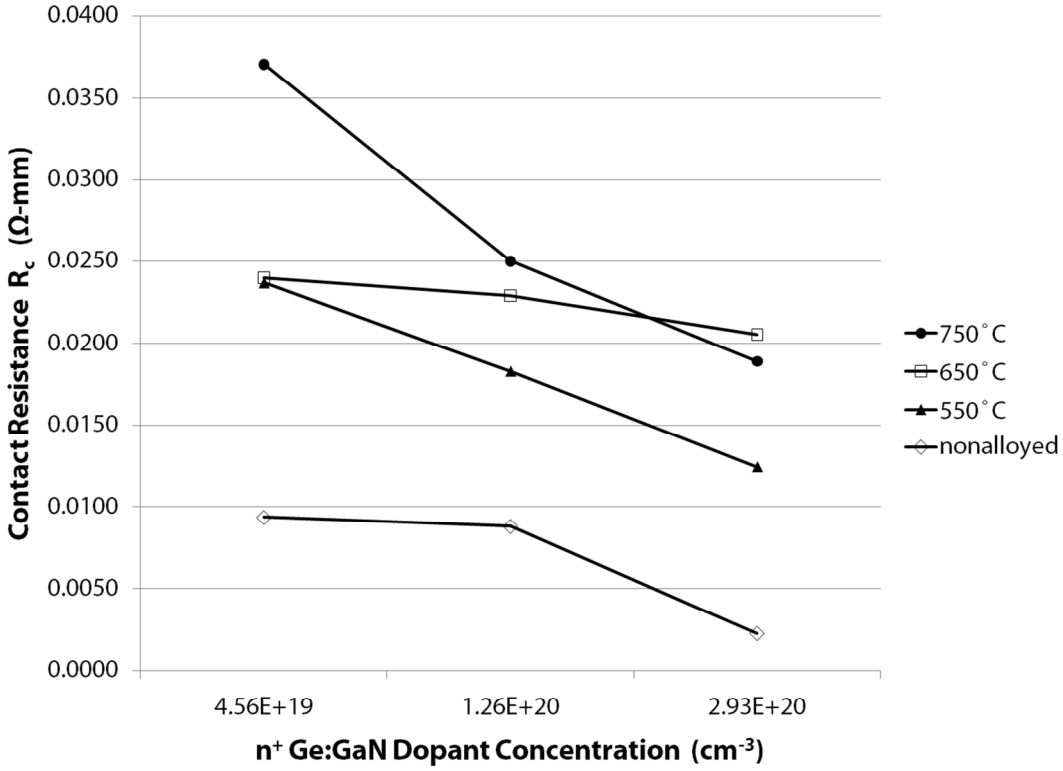

Figure 10. Contact resistance for Ti/Al/Mo/Au contacts to highly-doped n^{++} Ge:GaN as a function of dopant concentration and anneal temperature

Ohmic contact is further improved by metallic pathways to the 2DEG. For the case of alloyed contacts to GaN HEMTs, electrical contact to the 2DEG is achieved along inclusions produced around screw dislocations, implying an inverse correlation between defect density and contact resistance [51]. These electrical pathways from the ohmic contact to the 2DEG have been identified by Scanning Transmission Electron Microscopy (STEM) as TiN inclusions [52]. As seen in Table 8, the work function of TiN is significantly lower than that of Ti and lower than the electron affinity of GaN, χ_{GaN} = 4.1 eV, facilitating ohmic contact formation.

For HEMT designs including an AlN interbarrier, an additional first-layer metal, which alone or alloyed with nitrogen exhibits an even lower work function, is necessary to achieve good ohmic contacts. Utilizing a standard Ti/Al/Mo/Au stack to contact $Al_xGa_{1-x}N$/AlN/GaN material, a contact resistance of 2.0 Ω mm is observed; however, the inclusion of 75 Å Ta into a five-metal Ta/Ti/Al/Mo/Au stack achieves record-low 0.11 Ω mm contact resistance [53]. Thus for the experiments in this dissertation, Ta is used as a first-level metal in the typical Ti/Al/Mo/Au ohmic stack when an AlN interbarrier is present in the epitaxial layer design.

Table 8. Work function Φ_M of selected metals and alloys to GaN

Metal	$q\Phi_M$ (eV)	Ref.
Sc	3.5	[54]
TiN	3.74	[55]
Hf	3.9	[54]
Al	~4.2	[54]
Ta	4.25	[54]
V	4.3	[54]
Ti	4.33	[54]
Hg	4.475	[54]
W	4.55	[54]
Mo	~4.6	[54]
Ni	5.15	[56]
Pd	5.22	[54]
Au	5.4	[54]
Pt	5.64	[54]

3.4.3 Mesa Isolation

The HEMTs must be electrically isolated such that fringing fields may be neglected in the characterization of the devices. This may be accomplished either by ion implantation or by etching all but the active and contact regions of the devices. The latter approach is chosen, due to the availability of processes at the Cornell NanoScale Science & Technology Facility. Specifically, the barrier is etched beyond the 2DEG by an inductively coupled plasma reactive ion etch (ICP RIE) using chlorine (Cl_2), boron trichloride (BCl_3), and argon (Ar) chemistry. The BCl_3 in a reactive ion process physically breaks the crystalline bonds while the Cl_2 chemistry chemically etches the material. The etch depth must be deeper than the barrier layers, such that a 2DEG will not form, and is often even deeper to separate the active regions of the device from potentially high unintentional doping concentrations in the UID GaN. The depth is limited by the height of the gate stack, which must make electrical contact from the gate pad metallization onto the mesa.

3.4.4 Ohmic Anneal

Following mesa isolation and preceding Schottky metallization, the ohmic contacts are annealed to form an alloyed, low-resistance contact to the 2DEG. Both the anneal time and temperature may be optimized for a particular material stack to form the lowest contact resistance. For AlGaN/GaN devices using the four- or five-layer metal stacks investigated in this work, the optimized anneal temperature is typically 800°C.

3.4.5 Passivation

Two methods have been investigated in this work. First, silicon nitride (SiN_x) may be deposited using Plasma-Enhanced Chemical Vapor Deposition (PECVD) at

375°C. For the experiments in this work, the SiN_x dielectric thickness ranges between 40 μm and 85 μm. The deposition of such layers increases the 2DEG density and breakdown voltage of the HEMTs, but increases capacitive loading, specifically the gate–drain capacitance C_{gd}, and thus reduces small-signal gain [45]. Subsequent to the deposition, the contact electrodes and gate footprint are opened using a PMMA-masked fluorine-based RIE. A two-step etch is utilized with a parallel process monitor sample; following the first etch, the etch RF power is reduced and the sample is slowly etched to mitigate surface damage. A 450°C anneal is utilized to ameliorate the current density, which may have degraded due to surface damage within the gate window.

The SiN_x passivation is deposited and windowed prior to gate metallization. As an alternative, rectangular or mushroom-shaped gates may be deposited prior to passivation. This process order allows direct measurement of the effects of passivation by comparing device performance prior and subsequent to dielectric deposition.

The high-temperature of the PECVD process necessitates a blanket deposition; i.e., the wafer may not be selectively masked with resist. A second passivation method investigated in this work involves plasma ALD at ~100°C. At this temperature, the plasma ALD process produces a higher-density film than the alternative, thermal ALD process. The wafer was coated with a high-contrast 950K MIBK/495K A8 PMMA resist stack. The resist was baked at 200°C, well above the 107°C deposition temperature, so reflowing of the patterned resist was not a concern. The active regions of the devices were patterned rapidly by e-beam lithography at a current of 50 nA and a dose of 650 μC/cm². The deposition rate was quoted as 1.37 Å per loop, so 180 loops were performed to target a 25 nm Al_2O_3 film. Following lift-off in methylene chloride, the Al_2O_3 film thickness was measured using a profilimeter as 25–27 nm, corresponding to a plasma Al_2O_3 deposition rate of ~1.45 Å per loop at 107°C.

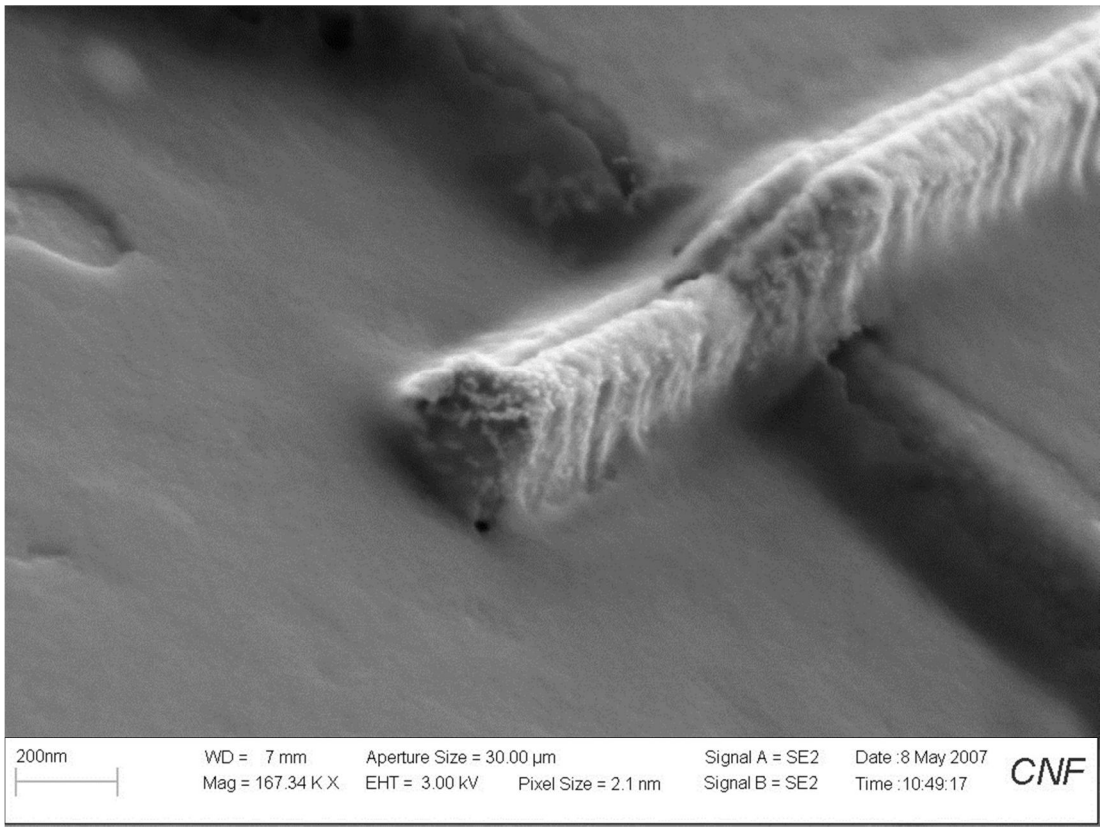

Figure 11. Field-plated Ni/Au gate atop $Al_{0.26}Ga_{0.74}N$/GaN-on-diamond depicting the asymmetric gate extension, atop the SiN_x passivation layer, extending toward the drain

3.4.6 Gate & Pad Metallization

The Schottky contact scheme is opposite that of the ohmics; i.e., a high work function metal is utilized to form a rectifying contact to n-type material. Two common gate metals are Pt or Ni: the latter is preferred as it adheres more readily to GaN. The Schottky barrier height is calculated as a function of the work function of the metal and the electron affinity of the semiconductor:

$$\Phi_B = \Phi_M - \chi_S \tag{29}$$

The accepted value in the literature for the electron affinity of GaN, which is in agreement with Figure 6, is $\chi_{GaN} = 4.1$ eV. Using the values from Table 8 in equation (29), the Schottky barrier height for Ni and Pt gates on GaN is, respectively, 1.0 eV and 1.5 eV.

Often, a gate extension atop the passivation layer toward the drain is desired to increase breakdown voltage and thus increase large-signal voltage swing and output power at the cost of frequency performance. Such a Γ-shaped gate with an asymmetric extension toward the drain is pictured in Figure 11.

If the pad metallization is separated from the gate metallization step, then a Ti/Au scheme may be used for good adhesion, low resistance, and atmospheric inertness. This is particularly important for multi-finger structures, for which an ultrasonic excitation may be necessary to achieve pad lift-off; in this case, the Ti/Au pads may be deposited and lifted off and Ni/Au gates defined in a subsequent lithography step. Additionally, adhesion is critical if the pads will be wire-bonded into a circuit, and a Ti first layer is essential, as Ni/Au pads have been demonstrated to delaminate during wire bonding.

CHAPTER 4: HEMT CHARACTERIZATION

4.1 Material Pre-Screening

Before commencing a process run, it is useful to characterize the morphology and electrical properties of the material to establish a baseline for the HEMT performance.

Following growth and before processing, the electrical properties of the epitaxial layers, including the 2DEG sheet density n_s, may be characterized by a Lehighton contactless sheet conductance measurement, a wetted-Hg probe C–V measurement, and Hall measurement.

The Lehighton Electronics model LEI88 makes a contactless measurement of the sheet conductivity, the reciprocal of the sheet resistance of a 2DEG layer.

A Hewlett Packard wetted mercury probe system is used to profile carrier concentration as a function of depth within the buffer. From the C–V data, the carrier concentration N (cm^{-3}) (30) as a function of depth d (31) is extracted.

$$N(d) = -\frac{C^3}{q\,\epsilon_0\,\epsilon_r\,A^2}\left(\frac{dC}{dV}\right)^{-1} \tag{30}$$

$$d = \frac{\epsilon_0\,\epsilon_r\,A}{C} \tag{31}$$

The 2DEG sheet density n_s may be measured by first sweeping from below pinch-off through approximately +0.5 V to overcome the difference in work function between the Schottky barrier of the mercury contact and the subsequently fabricated Ni gate contact and then integrating the extracted N–d curve.

For unintentionally doped (UID) GaN buffers, the Debye tail from the 2DEG observed in the carrier concentration versus depth (N–d) plot should fall by at least three orders of magnitude from below the 2DEG to the back of the buffer. By

analyzing this plot, undesirably high buffer charge or a parasitic shunt interface conductance may be identified before leaky devices are fabricated.

A sample may be prepared using indium contacts for a measurement of the Hall mobility. Although useful for comparison among wafers, the Hall mobility is ~1.5 times the drift mobility, which is a parameter relevant to electron transport in the HEMT. The drift mobility may be calculated using the sheet resistance R_{sh} and sheet density n_s measured by Lehighton and C–V, respectively. The drift mobility, reported in cm²/V s, follows as:

$$\mu_d = \frac{1}{q\, R_{sh}\, n_s} \tag{32}$$

For the 2DEG of an $Al_xGa_{1-x}N$/GaN HEMT, this is typically μ_d = 1300–1500 cm²/V s.

4.2 Transfer Length Method

After ohmic contacts are formed, transfer length method (TLM) measurements provide an indication of contact and material quality. The TLM model, fully derived in [57], allows the extraction of contact resistance (between the contact metal and the 2DEG), sheet resistance (within the 2DEG), and the transfer length (the characteristic length of current crowding into the ohmic contact.)

This method makes the assumption that the sheet resistance is uniform, which is not the case under the alloyed contacts. For good ohmic contacts, this assumption holds as an approximation. To verify the quality of the contacts, the sheet resistance should be relatively invariant as a function of anneal temperature and should be equal to that obtained by a Lehighton or Hall measurement.

For simplicity, in this dissertation rectangular TLM patterns, consisting of rectangular ohmic contacts separated by semiconductor gap lengths between 5 μm and

35 μm in 5 μm increments, are used. When these contacts sit on isolated mesas on the order of 100 μm wide, then the net current flow is considered to be along one dimension without fringing fields and, due to the large mesa width, surface depletion may be disregarded. Considering the effect of finite length of ohmic contacts, the contact length L_Ω and transfer length L_t are related to the contact resistance, assuming infinite contact length, by:

$$R_c = R_{c\infty} \coth(L_\Omega / L_t) \tag{33}$$

Thus, to avoid a condition of current constriction, HEMTs should be designed with ohmic (source or drain) contact lengths of at least 5 L_t.

For process monitoring purposes, the resistance of the TLM gaps may be measured subsequent to ohmic anneal but prior to mesa isolation; however, the sheet resistance will be artificially low because the fringing current pathways are not constrained between the two mesas. For example, considering Ti/Al/Mo/Au contacts to an $Al_{0.25}Ga_{0.75}N$/GaN HEMT on a bulk SI-GaN substrate before and after mesa isolation in Table 9, the TLM results prior to mesa isolation are severely distorted from the accurate numbers measured for the TLM patterns on isolated mesas.

Table 9. Ohmic contact properties measured by TLM before and after mesa isolation for a 200 Å $Al_{0.25}Ga_{0.75}N$/GaN-on-GaN HEMT

	Before Mesa Isolation	After Mesa Isolation
R_c (Ω-mm)	0.78	0.13 ± 0.02
R_{sh} (Ω/□)	215	439.9 ± 37.8
R_{sc} (Ω-cm²)	2.8×10^{-5}	$4.1 \pm 1.2 \times 10^{-7}$
L_t (μm)	3.6	0.30 ± 0.04

Typical ranges for the contact resistance, specific contact resistance, and transfer length of $Al_xGa_{1-x}N$/GaN HEMTs are R_c = 0.1 – 1 Ω mm, $R_{sh} \approx 450$ Ω/□, $R_{sc} \sim 10^{-6}$ Ω cm², and L_t = 0.3 – 1 μm. Achieving low-resistance ohmic contact to high-Al content $Al_xIn_{1-x}N$/GaN HEMTs remains a challenge, as the electrical barrier height is much larger. In this work, an optimal value of 0.62 ± 0.05 Ω mm was achieved using a Ta/Ti/Al/Mo/Au metallization. This is comparable to the best results reported in the literature, including 0.7 Ω mm for a standard Ti/Al/Ni/Au metal stack at an optimized anneal temperature on a pre-treated surface [58]. However, since the sheet resistance for $Al_xIn_{1-x}N$ barriers designed for microwave HEMTs is $R_{sh} \approx 250$ Ω/□, given such a high contact resistance, the specific contact resistance is on the order of $R_{sc} \sim 10^{-5}$ Ω cm².

4.3 DC

The HEMTs are characterized using a Hewlett Packard 4142B DC Modular DC Source/Monitor. The gate is driven using an HP41420B medium-power source/monitor unit (SMU) capable of sourcing 100 V or 100 mA, and the drain is driven using a high-power SMU HP41420A capable of 200 V or 1 A. Since the HEMT is a voltage-controlled device, an HP41425A analog feedback unit is utilized to quickly modulate the gate voltage to achieve a target drain current.

The DUT is contacted using Cascade coplanar ground-signal-ground (GSG) on-wafer probes. A standard, dc device characterization test routine, controlled by MATLAB software, consists of five measurements. First, a transfer characteristic is obtained in which the drain and gate currents are measured as a function of gate bias from below pinch-off through full-channel operation, typically at V_{GS} = +1 V, at a set drain bias 1–2 V beyond the knee. Next, a stress is applied to the device for about a minute, typically at the same drain bias beyond the knee with a gate bias chosen to

achieve 20% of the full-channel current. This step helps to burn-in the device and ensure that subsequent sweeps are accurate and repeatable. Subsequent to the stress, a second transfer characteristic is measured. Following that, the drain and gate currents are measured as a function of swept drain bias for gate biases stepped from below pinch-off to fully-on. The power compliance is limited to 10 W/mm to avoid damaging these high-current HEMTs. Finally, transfer characteristics are swept at each drain bias of interest for subsequent small-signal measurement.

4.4 Thermal Measurement

Experimental study of HEMT channel temperature rise requires a localized technique. Over the past two decades, scanning thermal microscopy (SThM) has emerged as a means for the high-resolution measurement of temperature [59]; however, it has only recently been applied to AlGaN/GaN HEMTs [60]. One AFM-based SThM implementation involves the replacement of the AFM tip by a microscopic, resistive filament that acts as one leg of a Wheatstone bridge. A platinum-based Wollaston wire filament offers linear response in resistance to changes in temperature. A small amount of current, 3 mA, is passed through the probe below its self-heating threshold. After calibrating against a heat source monitored by a thermocouple, the output voltage of the Wheatstone bridge may be extrapolated to the absolute temperature of the filament. In this work, a ThermoMicroscopes SThM attachment was used on a Park Scientific Instruments M5 AFM. The software simultaneously captures a topographic and thermal profile of the semiconductor surface.

Other spatially-localized thermal measurement techniques include infrared (IR) thermography [61], photoluminescence spectroscopy [62], and micro-Raman spectroscopy [63]. IR thermography is particularly challenging to interpret for opaque

substrates such as SiC, where the observed intensity includes components contributed from as deep as the chuck at the backside of the wafer. Photoluminescence spectroscopy is complicated by the additional laser excitation-induced heating of the material. Rather than a direct measurement of the surface temperature, micro-Raman thermography produces a laterally-resolved temperature profile of the epitaxial layers. Considering the case of GaN HEMTs, this is a ~2 μm GaN buffer in which approximately half of the temperature rise, or equivalently thermal resistance, of the device is evolved. In addition to a lateral temperature profile, the use of confocal micro-Raman spectroscopy permits the measurement of temperature as a function of depth in the substrate [64]. In all of these measurement techniques, careful analysis and comparison to models is necessary to properly interpret the device temperature rise and extract its thermal resistance.

As an alternative to these measurements of temperature, temperature rise may be extracted from the difference between pulsed and dc measurements [65],[66] or from pulsed diode characteristics [67] as a function of base plate temperature. Pulsed techniques often assume isothermal operation, i.e., no temperature rise, for low duty cycles and pulse lengths on the order of 100 ns; however, significant self-heating has been measured even for such short timeframes [68].

Surface temperature rise may be directly measured either by SThM or by liquid crystal thermography. In the latter case, a liquid crystal is melted over the DUT, which is illuminated using a polarized light source. The crystal phase transition is observed through a polarizing filter. The base plate temperature at which the liquid crystal changes phase is measured as a function of dc bias power dissipated across the DUT. The thermal resistance of the DUT is then extracted as the slope of the base plate temperature versus power at which the phase transition takes place. Unlike SThM, the liquid crystal technique requires multiple crystals with different transition

temperatures to measure a nonlinear evolution of thermal resistance as a function of bias.

While each technique has its advantages, the SThM technique is favored in this work for its competitive lateral resolution and direct measurement of surface temperature. The temperature rise on diamond is also reported as measured by liquid crystal thermography and IR spectroscopy, for which the diamond is opaque.

4.5 Thermal Modeling

Three models were utilized in this dissertation to seek agreement with measured thermal data. First, a three-dimensional finite difference simulator was developed at Group4 Labs [69]. The program solves the heat transfer equation in cylindrical coordinates, thereby greatly reducing computation time compared to a three-dimensional rectangular coordinate system. The simulator allows heat sources of arbitrary shape, which is typically an array of rectangles representative of the active regions of a multi-finger HEMT device under bias. The results of this simulator agree with the published results of three-dimensional finite element simulations in [70].

Second, the analytical thermal resistance calculation presented in [70] was adapted into a prolate spheroidal model for single-channel homoepitaxial devices. The model assumes a large-periphery device with multiple fingers such that symmetric boundary conditions are established in planes halfway between each pair of fingers. Without this symmetry, the analytical model cannot be applied to multiple-layer device structures, such as GaN-on-SiC. For the homoepitaxial GaN-on-GaN structures studied in this work, over all of the channel lengths experimentally measured, this three-dimensional analytical model agrees with the computationally-intensive three-dimensional finite difference model within 7%.

The above models do not take into account the nonlinear dependence of thermal conductivity on temperature, depicted in Figure 12, which is modeled as:

$$k(T) = k(300\text{K}) \times \left(\frac{300\text{K}}{T}\right)^{\alpha} \tag{34}$$

The dependency factor $\alpha \approx 1$; values from literature for relevant semiconductors are compiled in [12]. To demonstrate the effect of the nonlinear thermal conductivity on the temperature rise of a HEMT, a two-dimensional finite element model was developed. This simulation utilizes the MATLAB Partial Differential Equation Toolbox to solve the nonlinear heat flow equation:

$$-\nabla \cdot k(T)\,\nabla T = 0 \tag{35}$$

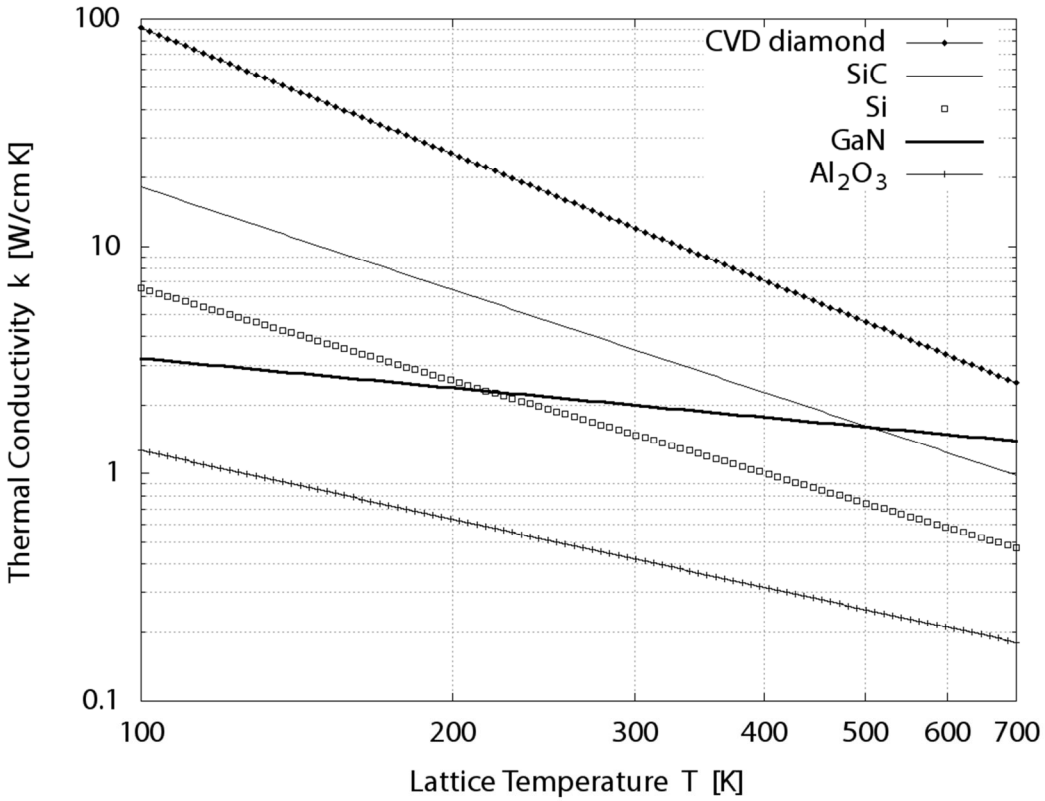

Figure 12. Modeled temperature dependence of thermal conductivity

Consider, for example, a 5 μm long, infinitely-wide HEMT channel with a 1.5 μm GaN buffer and 370 μm SiC substrate, the back side of which is held at 300 K. By incorporating the temperature dependence of thermal conductivity as modeled in Figure 12, a slight superlinear dependence is observed for the temperature rise as a function of dissipated power; the calculated trend is shown in Figure 13.

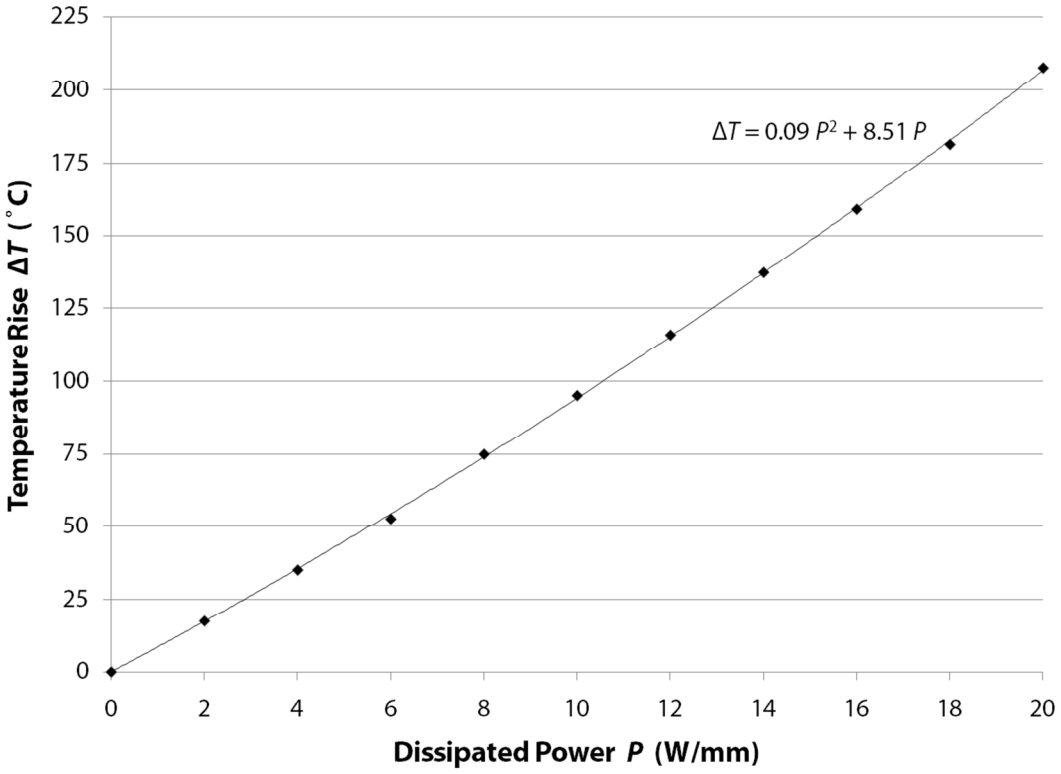

Figure 13. Two-dimensional finite element simulation of the nonlinear dependence of temperature rise versus dissipated power for a GaN-on-SiC HEMT

4.6 Small-Signal Measurement and Modeling

When characterizing an active or passive device at microwave frequencies, we are interested in the magnitude and phase response of the device as a function of frequency. Pragmatically, the scattering parameters, or *s*-parameters, are the most

functional representation for directly measuring and reporting microwave response [71]. In this work, the *s*-parameters are measured as a function of frequency for the HEMTs using a Hewlett Packard 8510C Vector Network Analyzer (VNA). As for the DC measurements, Cascade coplanar GSG on-wafer probes are used to contact the device pads. The VNA reference plane is calibrated at the probe tips using a Cascade impedance standard substrate.

A thorough development of the high-frequency model for GaN HEMT operation is found in [72]. The metrics for the frequency limitations of HEMTs include the unity-current-gain frequency and the maximum frequency of oscillation.

The unity-current-gain frequency, f_T, is the frequency at which the short-circuit current gain $|h_{21}|$ becomes unity for a HEMT in common-source configuration. The conversions between scattering (*s*) and hybrid (*h*) parameters are defined in [71]. For a HEMT, this metric is approximated by the equivalent circuit parameters [73]:

$$f_T = \frac{g_m}{2\,\pi}\left[\left(C_{gs} + C_{gd}\right)\,\left(1 + \frac{R_d + R_s}{R_{ds}}\right) + C_{gd}\,g_m\,\left(R_d + R_s\right)\right]^{-1} \tag{36}$$

In the case of a GaN HEMT, this may be simplified and related to the channel saturation velocity and gate length (the ratio of which is the electron transit time under the gate τ) by the relationship:

$$f_T \cong \frac{g_m}{2\,\pi\,\left(C_{gs} + C_{gd}\right)} \cong \frac{v_{sat}}{2\,\pi\,L_{G,eff}} \tag{37}$$

Thus, the drift velocity may be directly measured using a VNA and a series of gate lengths. The definition of f_T in equation (37) assumes that the HEMT behaves like a single-pole circuit, such that $|h_{21}|$ rolls off at 20 dB/decade or 6 dB/octave.

The definition of the maximum frequency of oscillation, f_{max}, is less straightforward. The stability factor of a two-port network is given by [71]:

$$k(f) = \frac{1 - |s_{11}|^2 - |s_{22}|^2 + |s_{11}s_{22} - s_{12}s_{21}|^2}{2|s_{12}s_{21}|} \tag{38}$$

For frequencies at which $k < 1$, the amplifier is conditionally stable, viz. oscillation may occur for a DUT terminated in a particular range of passive source and load impedances. When this is the case, the Maximum Stable Gain (MSG) is defined:

$$\mathrm{MSG}(f) = \left|\frac{s_{21}}{s_{12}}\right| \tag{39}$$

In the case of frequencies at which $k > 1$, the DUT is unconditionally stable. For HEMTs, this is encountered as the gain decreases at higher frequencies. In this case, the Maximum Available Gain (MAG) is defined:

$$\mathrm{MAG}(f) = \left|\frac{s_{21}}{s_{12}}\right| \left(k - \sqrt{k^2 - 1}\right) \tag{40}$$

Mason's power gain, U, is the maximum achievable gain when a DUT is terminated into a reciprocal, lossless matching network and is given by:

$$U(f) = \frac{\frac{1}{2}\left|\frac{s_{21}}{s_{12}} - 1\right|^2}{k\left|\frac{s_{21}}{s_{12}}\right| - Re\left\{\frac{s_{21}}{s_{12}}\right\}} \tag{41}$$

The metric $f_{\max}$, above which the DUT will not oscillate, is defined as the frequency for which the value of equation (39), defined for $k > 1$, or equation (40), defined for $k < 1$, or equation (41) is equal to unity, or 0 dB. For a HEMT, this metric is approximated for low parasitic resistances by the equivalent circuit parameters [73]:

$$f_{\max} = \frac{g_{\mathrm{m}}}{2\,\pi\left(C_{\mathrm{gs}} + C_{\mathrm{gd}}\right)}\left\{4\,\frac{R_{\mathrm{g}} + R_{\mathrm{s}} + R_{\mathrm{i}}}{R_{\mathrm{ds}}}\left[1 + 4\,\pi\,f_{\mathrm{T}}\,R_{\mathrm{ds}}\,C_{\mathrm{gd}} \times\left(1 + \frac{R_{\mathrm{s}}}{R_{\mathrm{g}} + R_{\mathrm{s}} + R_{\mathrm{i}}} + \frac{2\,\pi\,\tau}{\left(R_{\mathrm{g}} + R_{\mathrm{s}} + R_{\mathrm{i}}\right)C_{\mathrm{gs}}}\right)\right]\right\}^{-1/2} \tag{42}$$

As demonstrated in equations (36) and (42), capacitive effects principally limit the current gain while the parasitic resistances, namely the access resistances R_{d} and R_{s},

additionally limit the frequency performance. Thus, minimizing these parasitics is a crucial step toward realizing mm-wave circuits.

A linear equivalent circuit model provides insight into the small-signal performance of a device by selecting circuit parameters with physical or geometric significance. The equivalent circuit is comprised of extrinsic parasitics and intrinsic circuit elements. The extrinsic parasitics include the pad capacitances and the inductances and resistances associated with the gate, source, and drain. These may be de-embedded using a cold-FET technique and the intrinsic parameters may be extracted as detailed in [74]. This model was recently enhanced in [75] for devices contacted using coplanar waveguide probes.

A schematic for this latest HEMT model appears in Figure 14. The voltage-dependent current source supplies:

$$I_{gm} = V_{Cgs}\, g_{m0}\, e^{-j\omega t} \tag{43}$$

where g_m represents the intrinsic RF transconductance and the driving voltage is evolved across the intrinsic capacitance C_{gs}.

The extrinsic parasitic elements include the combination of resistance and inductance at each device terminal, including pad inductances L_g, L_s, and L_d as well as gate metallization resistance R_g, and access resistances R_s and R_d. The asymmetry in the coplanar waveguide design introduces on-mesa capacitive parasitics C_{gs}^{mesa} and C_{gd}^{mesa}. Passivation-induced gate leakage current is modeled by intrinsic shunt conductances G_{gs} and G_{gd} [75]. As in [74], the parasitic pad capacitances (C_{pgs}, C_{pgd}, and C_{pds}) are extracted in deep pinch-off with a forward bias applied to the shorted source and drain contacts such that the gate leakage is minimized and pad capacitances are locally bias-independent. Following [75], we assume the on-mesa capacitances $C_{gs}^{mesa} = C_{gd}^{mesa} \approx C^{mesa}$ which is calculated as (80 fF/mm) normalized to W_g. The parasitic source and

gate inductances are corrected using the diffusion capacitance and dynamic resistance of the forward-biased Schottky diode. The remaining, intrinsic parameters are extracted following the approach of [74].

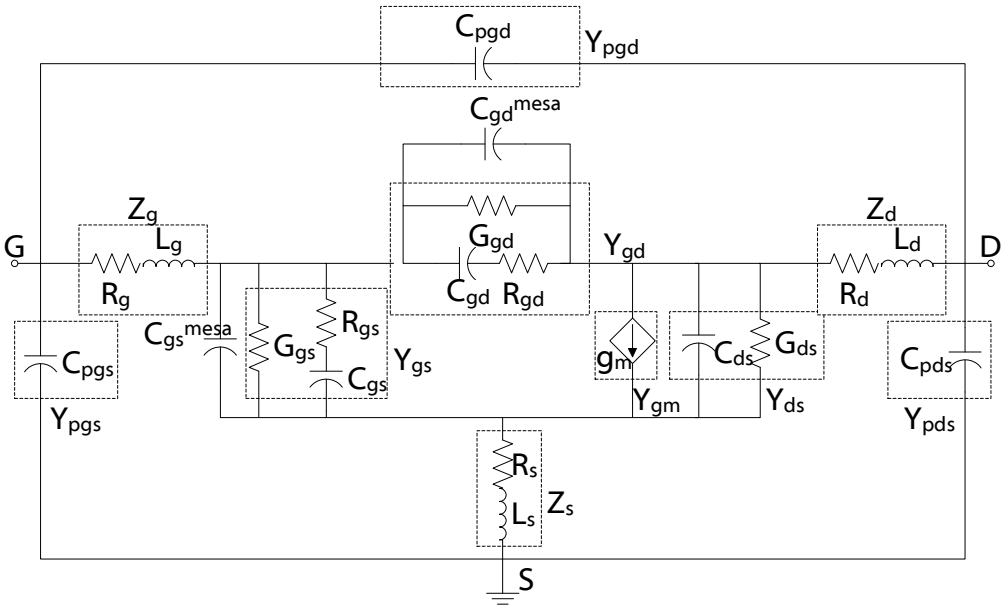

Figure 14. Linear equivalent circuit for a GaN HEMT

A practical matter of the cold-FET extraction requires drawing current through the gate. The high forward gate current density utilized in the traditional cold-FET measurement technique, as employed in the above procedure, may permanently degrade less-robust GaN HEMTs. An alternative extraction procedure for a 20-element distributed small-signal model eliminates the need to draw forward current through the gate [76].

Small-signal models may be extended to model the electrical and thermal nonlinearities encountered during large-signal operation. Large-signal models of GaN HEMTs incorporate the nonlinear distortions of the output waveform which generate harmonics and intermodulation products. Models are categorized into physics-based

and measurement-based models, the latter of which includes analytical, black-box, lookup table-based, and neural network models [77]. These models may include bias, thermal, and temporal (trapping-related) dependences. A lookup table-based model is the most straightforward to create, by measuring the HEMT under a series of bias and drive conditions, while an analytical model may inherently be extrapolated to simulate device performance under arbitrary conditions. An analytical GaN HEMT model implemented in the commercially-prevalent Agilent ADS software has demonstrated close agreement between simulated and measured dc, small-signal, thermal, and large-signal data [78]. For more rapid design cycles, the modeling may be simplified using a combined analytical and lookup table-based approaches, as in [79].

While complex models with additional degrees of freedom facilitate more precise device simulation, which is necessary for pulsed or low-noise circuit design, a physical parameter model provides the greatest insight to the device designer. One such model [80] consolidates all of the parameters related to electron concentration and with just 17 parameters achieves excellent agreement between modeled and simulated dc and capacitive data.

4.7 Pulsed DC

Pulsed DC measurements are used to study the effects of trapping and self-heating on device performance. Contrary to many publications, isothermal conditions may not be assumed when driving GaN HEMTs with 100 ns pulses at a low duty cycle [68]. Thus, trapping and thermal effects are coupled for these pulsed measurements, just as they are for steady-state dc measurements. Regardless, a comparison between CW and pulsed I–V characteristics allows analysis of dispersive effects. In particular, pulsing the gate and drain simultaneously from a sub-threshold large-signal operating point, e.g. $V_{GSq} = V_t - 2$ V and $V_{DSq} = 20$ V, provides an indication of dc–rf dispersion

due to trapping. The pulsed I–V curve is a far simpler and faster measurement than an impedance-matched large signal measurement and, as such, is a useful characterization technique. The metric for this measurement is drain-lag, which is the percentage reduction in I_{DSS} pulsed from V_{GSq}, V_{DSq} referenced either to the cw dc value or the off-state value pulsed from $V_{GSq} = V_{DSq} = 0$ V. In this work, both device channels were simultaneously pulsed from a chosen quiescent point using an Accent DiVA Dynamic IV Analyzer. A disadvantage of the DiVA system is that it is a "black box" and the signals cannot be monitored, e.g., for inductive ringing effects; to minimize inductance, the DiVA system was connected by a short run of 3.5 mm rf cable directly to Cascade coplanar GSG on-wafer probes.

4.8 Load-pull

Perhaps the most pertinent measurement of transistors designed for microwave power amplification is a measurement of output power, gain, and efficiency as a function of input drive. At the wafer level, this power-in power-out (PIPO) measurement must be impedance matched to maximize power transfer into and out of the common-source HEMT. At the circuit level, such a match is would be implemented by an rf matching network. The goal of an rf matching network is to minimize reflection, i.e., to achieve $\Gamma = 0$. This will simultaneously maximize power transfer:

$$P_{in} - P_{refl} = P_{in}\,(1-|\Gamma|^2) \tag{44}$$

and minimize the standing wave ratio:

$$SWR = \frac{1 + |\Gamma|}{1 - |\Gamma|} \tag{45}$$

The capacitive reactance of the linear, small-signal performance of the device must be matched with its conjugate inductance. The load match is often reported as a series representation of resistance and capacitive reactance; it is useful to conceptualize the real component of the parallel transformation of the load impedance, referred to as the real load line:

$$R_L = |Z_L| = (R_s^2 + X_s^2) / R_s \tag{46}$$

The average output power of the device follows as:

$$P_{out} = V_{rms}^2 / R_L = I_{rms}^2 R_L \tag{47}$$

The amplitude of the sinusoidal CW voltage and current waveforms at the drain within the linear region of device operation, for which the higher-order harmonics are negligible, follow as:

$$V_a = (2 P_{out} R_L)^{½} \tag{48}$$

$$I_a = (2 P_{out} / R_L)^{½} \tag{49}$$

In addition to the output power of the HEMT, the efficiency is an equally important metric of performance. Any power that is not converted to microwave output power is dissipated within the device as heat, which will further degrade the overall device performance. The drain efficiency is given by:

$$\eta_D = P_{out} / P_{dc} \times 100\% \tag{50}$$

The drain efficiency continues to rise even as the device is driven deeply into saturation. A more useful measure of device efficiency takes into account the input power driving the device; the power-added efficiency (P.A.E.) is:

$$\text{P.A.E.} = (P_{out} - P_{in}) / P_{dc} \times 100\% \tag{51}$$

The peak in power-added efficiency (P.A.E.) is achieved at a slightly higher load impedance than the peak output power P_{out}; at this higher load impedance in class AB operation, the load line is reduced below the dynamic knee saturation current.

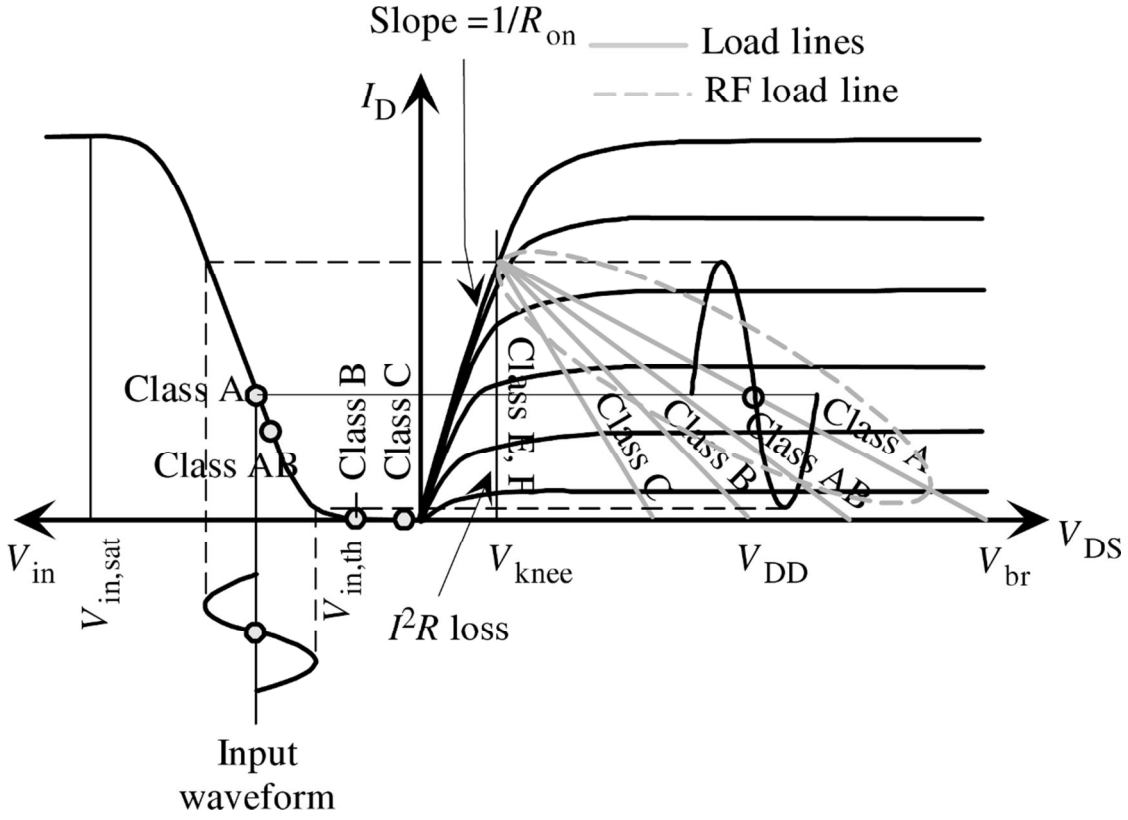

Figure 15. Classes of amplifier operation illustrated by quiescent point of gate and drain bias and load line; the dynamic class A load line is indicated by the light-gray, dashed ellipse [81]

The real component of the device load line in equation (46) may be approximated from a static dc I–V curve as shown in Figure 15, which depicts the pertinent bias points for class A, AB, and B amplifier operation. A class A amplifier is always on and achieves high output power with good linearity at the expense of efficiency; a class B amplifier is rectifying for one half cycle, thereby achieving higher

efficiency at the expense of linearity. GaN HEMTs perform with the highest efficiency while maintaining reasonable output power in class AB operation. This represents the quiescent bias points near pinch-off where f_T remains high, as self-heating and its impact on mobility are limited. Thus, class AB operation is the typical mode of operation for the CW evaluation of GaN microwave HEMTs. The characteristics of these three classes of operation are detailed in Table 10. Higher classes of operation are switching amplifiers involving more complicated circuitry to achieve higher efficiency operation.

Table 10. Output waveform, conduction angle, peak drain efficiency, and maximum output power for passively-terminated continuous-wave amplifier operation

	Class A	Class AB	Class B
Output Waveform	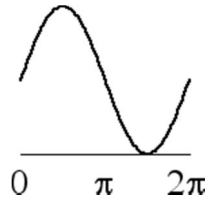	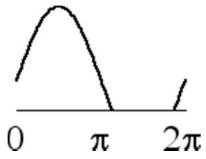	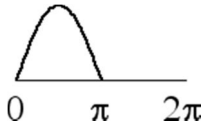
Conduction Angle	$\Theta = 2\pi$	$\pi < \Theta < 2\pi$	$\Theta = \pi$
Drain Efficiency η_D	< 50%		< 78.5%
Output Power P_{out}	$< \frac{1}{8}\, \Delta V\, \Delta I$		$< \frac{1}{4}\, \Delta V\, \Delta I$

The setup utilized for the majority of measurements in this work is depicted in Figure 16. The instrumentation includes rf switches, which facilitate wafer-level calibration and allow VNA small-signal measurements in addition to dc and large-signal measurements. The source is comprised of a Hewlett Packard 83622A synthesized sweeper and a 5 W solid-state amplifier. The bias system is an HP 4142B DC Modular SMU. A directional coupler at the input allows monitoring of

the input power reflected from the DUT so that it may be minimized during measurement. The reflected input and output power levels are measured using an HP 438A Power Meter. A second directional coupler beyond the rf switch on the drain side of the setup allows waveform monitoring by an HP 71500A Microwave Transition Analyzer (MTA), which functions as a sampling oscilloscope. The MTA allows real-time monitoring of the amplified waveform, but does not measure accurate incident power as quickly as the HP 438A. A pair of computer-controlled Maury MT983A01 tuners allow source and load impedance matching.

Due to the nonlinearities of the transistor operation, which is limited by finite access resistance and breakdown voltage, the match for optimal power transfer differs from the small-signal conjugate impedances. However, these conjugate impedances s_{11}* and s_{22}*, measured at the quiescent bias and frequency of interest, serve as a starting point for source- and load-pull measurements. The real component of the load impedance $|Z_L| = R_L$ should be increased such that the load line passes below the peak current I_{DSS} at the knee voltage.

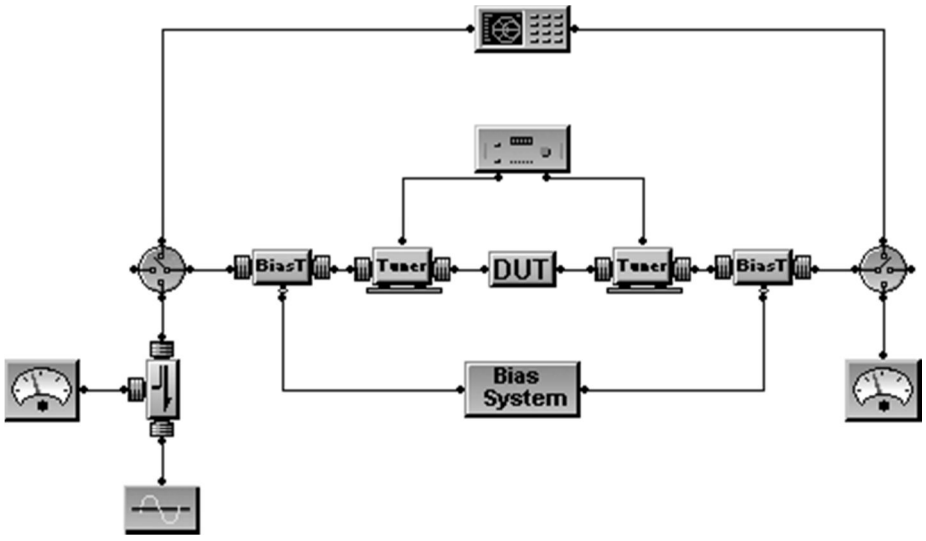

Figure 16. Block diagram for dc, small-signal, and 10 GHz power measurements

The large-signal performance of GaN HEMTs is limited by the breakdown voltage and the on resistance R_{on}, which is the sum of the source, drain, and channel resistances. In addition to these static characteristics, trap-induced dc–rf dispersion reduces the achievable current under high frequency operation, as discussed in section 4.7. Finally, the temperature rise in the device at high bias and drive levels reduces the electron mobility and limits performance. Thus, it is essential to achieve low-resistance contacts to the device, high-quality epitaxial layers free from trapping effects, and a high-thermal conductivity wafer design to limit self-heating.

4.9 Efficiency Model for Multi-Finger HEMTs

The Tilak model for the efficiency of large-periphery $Al_xGa_{1-x}N$/GaN HEMTs operated in class B [82] has been integrated with the analytical thermal resistance model [70]. The temperature dependence of drift mobility in GaN has been measured as [83]:

$$\mu \sim (T/T_0)^{-1.8} \tag{52}$$

Thus, the knee voltage as a function of temperature is modeled by:

$$V_{\text{knee}}(T) = V_{\text{knee}}(300\text{K}) \times \left(\frac{T}{300\text{K}}\right)^{1.8} \tag{53}$$

The temperature rise and drain efficiency are modeled as a function of device geometry and material thermal conductivity. The solution is iterated until the solution converges, typically after five cycles.

For this example, we assume identical device electrical performance from 2 μm GaN epitaxial layers, including I_{DSS} = 1 A/mm, V_{knee} = 4 V, and 100 V swing, such that V_{br} > 104 V, and a substrate thinned to 100 μm, a reasonable value for backside processing. The thinned substrate is maintained at room temperature in the model; practically, there would be an interface thermal resistance between the backside of the

device and a heat sink. The device geometry is set at 8 fingers with variable finger width. The device is biased for class B operation and driven at 10 GHz CW. The simulated thermal resistance of the devices as a function of gate width is presented in Figure 17.

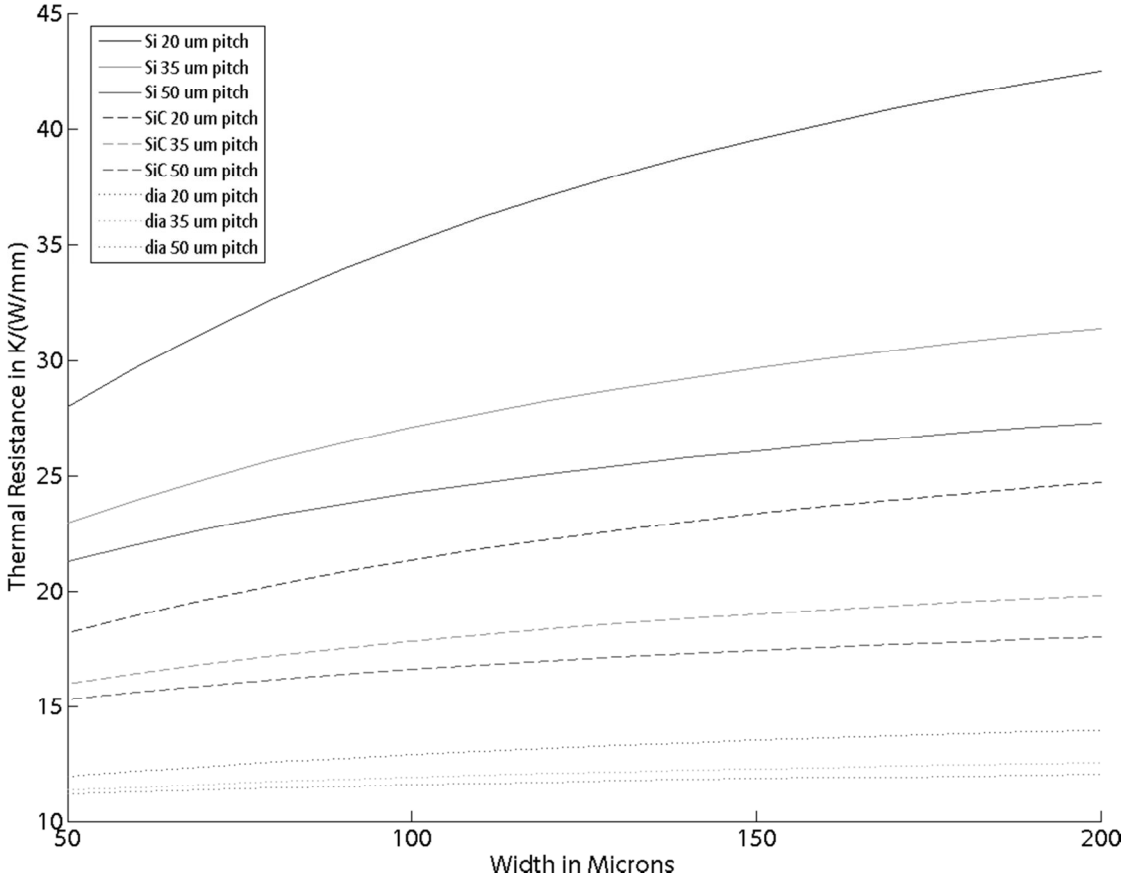

Figure 17. Thermal resistance as a function of channel width and gate pitch for an 8-finger $Al_xGa_{1-x}N$/GaN HEMT on a 100 μm Si, SiC, or diamond substrate

Next, the gate width is assumed to be 125 μm for a total periphery of 1 mm and dc power density of 1 A. The efficiency and temperature rise for Si, SiC, and diamond substrates are presented in Figure 18. For increasingly short gate-to-gate pitch, the temperature rise increases precipitously and knee walk-out causes a sharp decrease in

device efficiency. Given the relative insensitivity of the HEMT thermal resistance to the gate pitch in Figure 17, it is consistent that the drain efficiency continues to increase for GaN-on-diamond HEMTs even for very a short gate-to-gate pitch of 10 μm. Thus, GaN-on-diamond substrates enable higher density fabrication than possible even on the other commercially prevalent substrate technologies for microwave HEMTs.

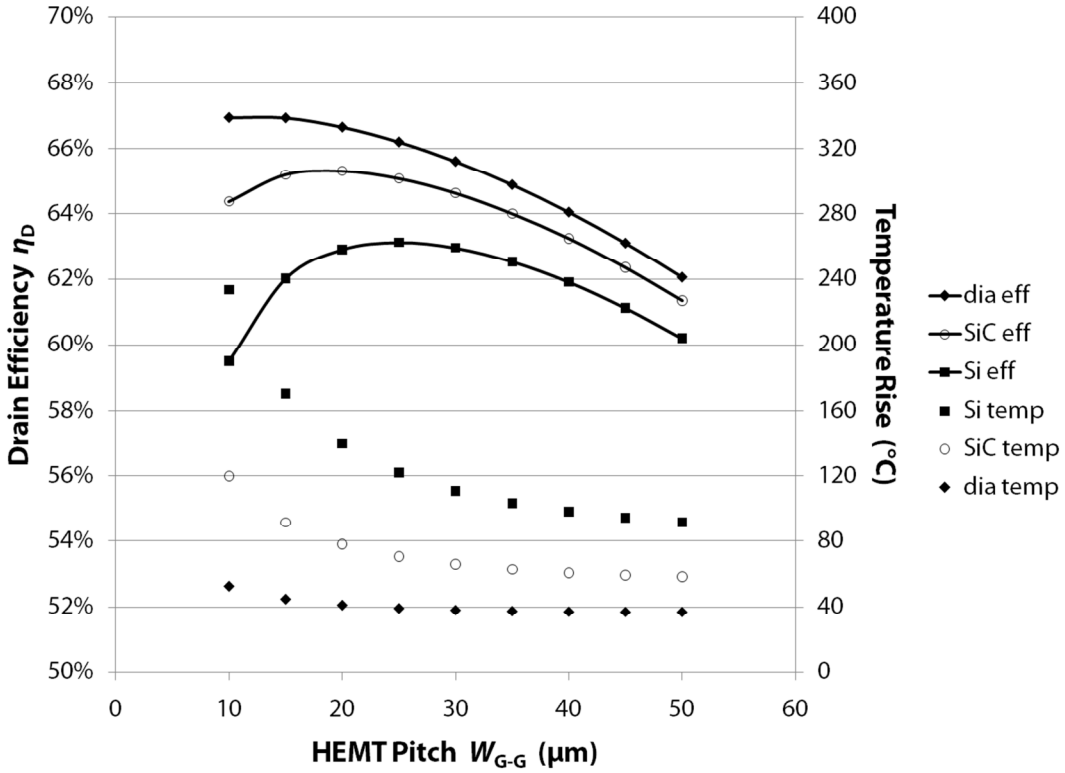

Figure 18. Drain efficiency and temperature rise as a function of pitch

CHAPTER 5: APPROACHES

5.1 AlGaN/GaN-on-Diamond HEMTs

$Al_xGa_{1-x}N$/GaN high-electron-mobility transistors (HEMTs) are well-suited to high-frequency and high-power applications. Electron mobility has been observed to decrease in AlGaN/GaN HEMTs as a function of temperature rise according to equation (52). To ameliorate the thermal limitations to high-power device performance, the device structure ought be located within close proximity to a material with high thermal conductivity. Polycrystalline diamond exhibits a thermal conductivity approximately 3.5 and 8 times that of SiC and Si, respectively (Table 6).

Group4 Labs has developed composite wafers in which GaN epitaxial layers are atomically attached to synthetic diamond substrates. This technology provides high thermal conductivity substrates for high-power GaN devices and exhibits near-optimal heat spreading. In the epitaxial transfer process, a 2 μm-thick GaN layer is lifted from its host silicon substrate and transferred to a CVD-grown diamond substrate. Group4 Labs' GaN-on-diamond process has been extended to four-inch diameter, 100 μm-thick substrates with estimated thermal conductivity of 12–15 W/cm-K. Figure 19 shows three GaN-on-diamond wafers with diameters of 1.5, 2, and 4 inches, all 100 μm in thickness.

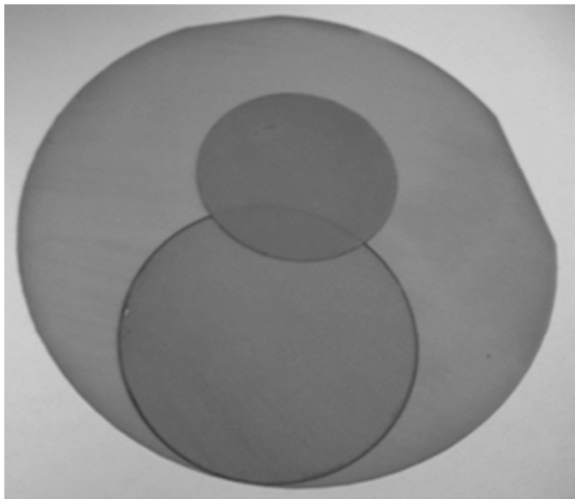

Figure 19. 1.5", 2", and 4" GaN-on-diamond wafers

5.1.1 Material Preparation

AlGaN/GaN is grown epitaxially on a silicon substrate, the front side is mounted onto a sacrificial carrier and the Si substrate is etched away. The exposed buffer is treated with a proprietary dielectric coating and atomically attached to 40–100 μm polycrystalline diamond. Finally, the AlGaN/GaN surface is liberated as the sacrificial carrier wafer is wet-etched from the front side of the material stack.

The epitaxial layers are comprised of 175 Å $Al_{0.26}Ga_{0.74}N$ pseudomorphically grown on 0.8 μm unintentionally-doped (UID) GaN atop a 1.1 μm AlGaN transition layer. A 20 Å GaN cap improves ohmic contact formation and a 50 nm interface layer located at the bottom of the AlGaN transition promotes the attachment to the diamond substrate. Note that material for one of the experiments, identified below, includes a 10 Å AlN interbarrier grown at the AlGaN/GaN interface.

The 2DEG is characterized by Lehighton and wetted-Hg probe C–V measurements. For these experiments, the material was laser cut into 15 × 15 mm pieces to facilitate processing.

5.1.2 Fabrication and Measurement

The devices were fabricated at the Cornell NanoScale Science & Technology Facility via electron-beam lithography. To facilitate handling, the 40 μm-thick GaN-on-diamond wafer was mounted to a carrier wafer using Crystalbond 509 adhesive and dismounted before steps that exceeded 170 °C. In multiple recent fabrication runs, 75 μm- and 100 μm-thick material was processed entirely freestanding.

A standard Ta/Ti/Al/Mo/Au ohmic recipe was used. Mesa isolation was achieved via an inductively-coupled plasma $Cl_2/BCl_3/Ar$ etch. The wafers were passivated with ~45nm PECVD SiN_x deposited at 375°C. The SiN_x was etched using an CF_4 RIE resulting in 70° sidewalls. The gates were Γ-shaped, following the 70° SiN_x sidewalls with a 50% field plate extension toward the drain.

Transfer length method (TLM) measurements were performed via four-probe technique. DC and small-signal characterization were performed using an HP 4142 and an HP 8510C with Cascade on-wafer probes. Pulsed dc measurements were made using an Accent DIVA system. Large-signal measurements were completed using Maury and Focus load-pull systems at 10 GHz.

5.1.3 AlGaN/GaN-on-Diamond Performance

Before processing, C-V measurements indicated a threshold voltage of -2.1 V and a sheet density $n_s = 8.1\times10^{12}$ cm^{-2}. After fabrication, TLM measurements averaged over eight sites across the wafer revealed a GaN-on-diamond contact resistance of 0.47 ± 0.07 Ω-mm and a sheet resistance of 440.5 ± 13.7 Ω/sq.

Table 11. Characteristics of an $Al_{0.26}Ga_{0.74}N$/GaN-on-diamond HEMT averaged over more than twenty 2 × 100 μm devices

	L_G = 0.10 μm	L_G = 0.15 μm
V_t (V)	-2.1±0.1	-2.0±0.1
I_{Dmax} (mA/mm)	797±32	786±16
I_{D0} (mA/mm)	604±32	591±9
g_m (mS/mm)	355±11	346±7
f_T (GHz)	57.1±2.2	48.0±0.6

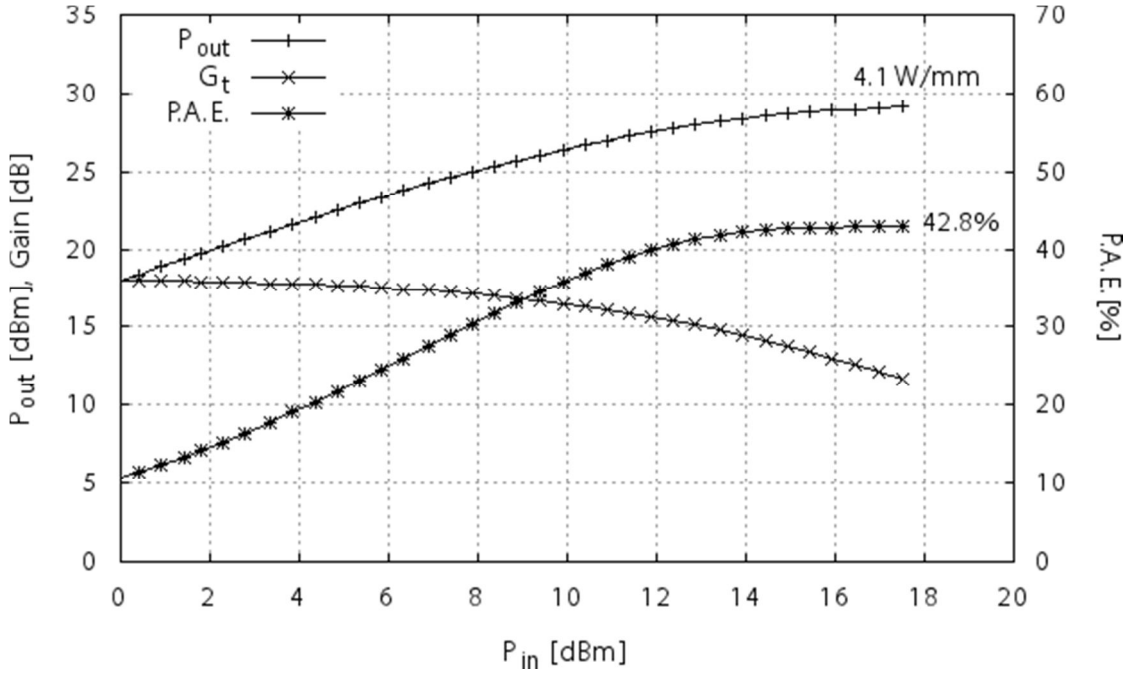

Figure 20. Output power measured at 10 GHz CW, V_{DS} = 35 V class AB for a 2 × 100 × 0.1 μm AlGaN/GaN-on-diamond HEMT with matching condition $Z_S = 178 \,||\, j82\ \Omega$ and $Z_L = 454 \,||\, j748\ \Omega$

Across the wafer, dc and small-signal device performance was consistent, indicating good process and material uniformity as shown in Table 11. Devices were

tested under continuous-wave (CW) class AB operation. A 2 × 100 × 0.1 μm AlGaN/GaN-on-diamond HEMT demonstrated a peak output power of 4.1 W/mm with power-added efficiency (PAE) of 42.8% when biased at V_{DS} = 35 V (Figure 20). Drain-lag pulsed I-V measurements revealed 15% dispersion in the knee region; this correlates to dc-rf dispersion and limits the output power.

Thermal measurements have been performed on GaN-on-diamond using thermal microscopy, IR thermography, and liquid crystal thermography. All three measurement techniques were performed on small devices and agree well for these similar geometries. Comparing HEMTs L_{SD} ~ 5 μm on diamond and SiC using the thermal microprobe, the thermal resistance on diamond was measured as ~6 °C/(W/mm), half that of the GaN-on-SiC device [84]. For a slightly-shorter 2 μm gap, the thermal resistance of GaN-on-diamond was measured by IR thermography as 7.6 °C/(W/mm). These values were confirmed by liquid crystal thermography, which reported a thermal resistance of 6.7 °C/(W/mm) and agreed within 10% of values from three-dimensional finite element simulations [85].

5.1.4 Comparison between AlGaN/AlN/GaN HEMTs on Diamond and Si Substrates

Pre-fabrication C–V measurements indicated a sheet density n_s = 7–9×10^{12} cm^{-2} for the identical epitaxial layers on transferred diamond and as-grown Si substrates. TLM measurements indicated a contact resistance R_c = 1.1 Ω-mm on GaN-on-diamond and GaN-on-Si.

A 2 × 50 × 0.06 μm AlGaN/AlN/GaN-on-diamond HEMT exhibited a full-channel current I_{Dmax} = 685 mA/mm and a zero-gate-bias current I_{D0} = 636 mA/mm. This device exhibited a unity-current-gain frequency f_T = 70.1 GHz, while a similar HEMT on Si substrate exhibited only f_T = 55.3 GHz.

Averaged over more than twenty devices on each substrate, the threshold voltage was V_t = -3.2±0.1 V on both substrates.

Equal-gate-length devices with gate footprint lengths of 60, 80, and 100 nm atop AlGaN/AlN/GaN epitaxial layers were compared between diamond and as-grown Si substrates. This initial comparison indicated that the devices on diamond exhibited ~9% higher current density (Figure 21) and 29% higher unity-current-gain frequency than identical structures on Si substrate.

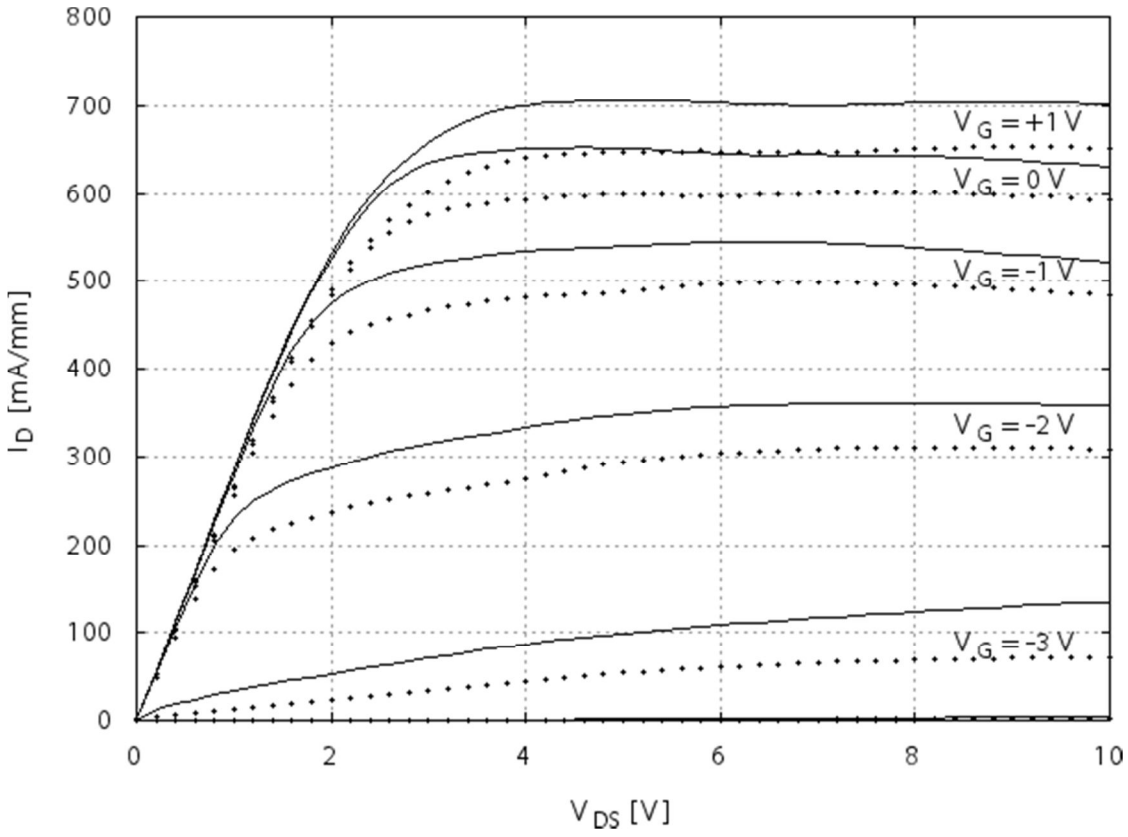

Figure 21. I-V characteristics for a 2 × 50 × 0.06 μm GaN-on-diamond (solid) and GaN-on-Si (dotted) HEMT

5.1.5 Summary

Good process and material uniformity has been demonstrated for AlGaN/GaN-on-diamond HEMTs. Utilizing the large-signal impedance match from the on-wafer measurements made as a part of this work, a passive matching circuit was developed and the first packaged GaN-on-diamond amplifier has been demonstrated [85].

The results of our first comparison between identical AlGaN/AlN/GaN epitaxial layers on diamond and Si substrates indicate improved HEMT performance on the material transferred to diamond. Buffer leakage native to the AlGaN/AlN/GaN-on-Si material precluded high-bias measurements such as large-signal characterization.

As a demonstration of the limits to frequency scaling for this relatively thick epitaxial structure, a 2 × 50 μm × 0.04 μm GaN-on-diamond HEMT exhibited f_T = 85 GHz and f_{max} = 95 GHz, the latter of which was limited by relatively high source resistance [86]. Further mm-wave performance enhancement demands a thinned epitaxial layer design with higher aluminum composition. Improved GaN epitaxial quality, perhaps from GaN-on-SiC or GaN-on-GaN source wafers, will allow high-power devices to fully utilize the improved thermal management of the GaN-on-diamond composite substrate technology.

5.2 AlGaN/GaN-on-GaN HEMTs

The homoepitaxial growth of AlGaN/GaN HEMTs on semi-insulating (SI) GaN substrates eliminates the dense dislocation matrix at the buffer-substrate interface present for other choices of substrate, commonly SiC, Si, or sapphire. The uniformity of the material mitigates threading dislocations and mismatch in thermal expansion coefficients typically stemming from the non-homogeneous buffer-substrate

interfaces. HEMTs fabricated on bulk GaN substrates have experimentally demonstrated 10W/mm large-signal performance at 10GHz and good reliability [87]. In this work, the K_a-band and thermal performance of AlGaN/GaN-on-GaN devices is presented.

5.2.1 Fabrication and Measurement

Bulk SI-GaN substrate was grown via HVPE at Kyma Technologies. AlGaN/GaN epitaxial layers were grown by MOCVD atop GaN and SiC substrates. 200Å $Al_{0.25}Ga_{0.75}N$ was grown atop 2.4μm regrown GaN on 374μm-thick GaN. The epitaxial layers on 370μm-thick SiC substrate were comprised of 200Å $Al_{0.26}Ga_{0.74}N$ atop 1.5μm GaN.

Devices on SI-GaN and SiC substrates were fabricated in parallel at the Cornell NanoScale Science and Technology Facility. A standard Ti/Al/Mo/Au Ohmic recipe was used, including a post-deposition anneal. Mesa isolation was achieved after Ohmic contact anneal via an ICP etch. After passivation with ~85 nm PECVD SiN_x, Ni/Au gates with field-plate extensions were patterned [88]. The devices were characterized electrically and thermally.

5.2.2 Experimental Results

The AlGaN/GaN HEMTs on SI-GaN demonstrated exceptionally good performance. Transfer length method measurements revealed a contact resistance of 0.13 Ω-mm and a sheet resistance of 440 Ω/□ (Table 12). Of note, the I-V curves exhibited reduced negative output resistance in saturation compared to HEMTs on other substrates.

Table 12. Ti/Al/Mo/Au ohmic contact properties measured by four-point probe TLM at seven sites across each wafer

Barrier	20 nm $Al_{0.25}Ga_{0.75}N$	20 nm $Al_{0.26}Ga_{0.74}N$
Substrate	SI-GaN	SiC
R_c (Ω-mm)	0.13 ± 0.02	0.22 ± 0.05
R_{sh} (Ω/□)	439.9 ± 37.8	409.0 ± 7.9
R_{sc} (Ω-cm²)	$4.1 \pm 1.2 \times 10^{-7}$	$12.1 \pm 5.0 \times 10^{-7}$
L_t (μm)	0.30 ± 0.04	0.53 ± 0.13

The devices exhibit a sharp pinch-off characteristic at $-5V_{GS}$ with a peak transconductance of 340mS/mm. The usual ~$5V_{DS}$ knee voltage with a drain current of 1050mA/mm at $+1V_{GS}$ was observed. The unity-current-gain frequency f_T was at 46.4GHz for a 100nm gate with field plate extension. The gate leakage current is moderately high, at 182μA, which is an order of magnitude greater than that observed for similar devices on SiC.

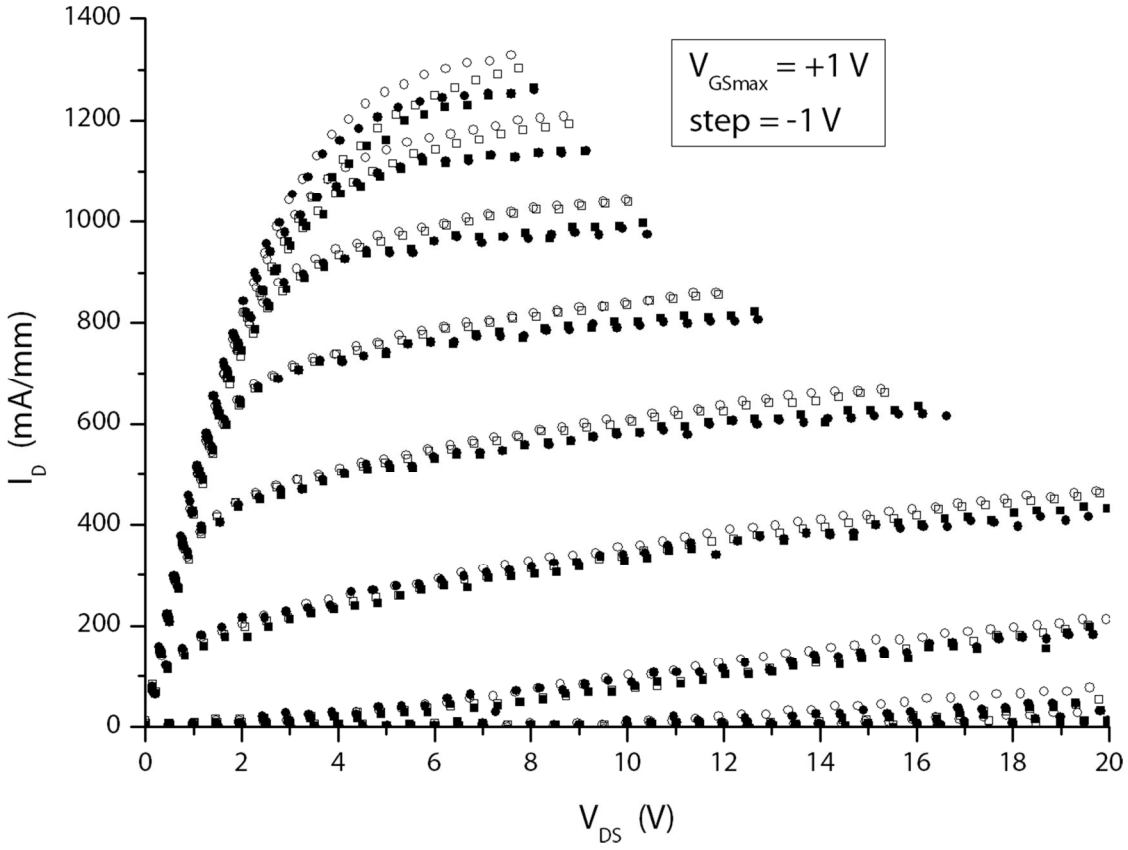

Figure 22. Quasi-dc (solid) and 200 ns pulsed (hollow) off-state (circular; V_{DS} = 0 V, V_{GS} = 0 V) and drain-lag (square; V_{DS} = 20 V, V_{GS} = −7 V) performance of a 2×100×0.1 μm (FP), 50 μm pitch $Al_xGa_{1-x}N$/GaN HEMT

Compared to dc characteristics, 200 ns pulsed off-state and drain-lag measurements for devices on bulk GaN indicate low dispersion, thus predicting good microwave performance (Figure 22). Large-signal measurements were completed at 18 and 28 GHz. At 18 GHz, for a 2×75×0.1 μm HEMT with 12 μm pitch between gate centers driven at 22 dBm and biased at 20 V and 511 mA/mm, output was 3.41 W/mm with 29.5% PAE. At 28 GHz, for a similar device with 25 μm pitch driven at 22 dBm biased at 20 V and 562 mA/mm, output was 2.54 W/mm with 16.8% PAE; when driven to 24 dBm, the HEMT output 3.12 W/mm with 18.3% PAE.

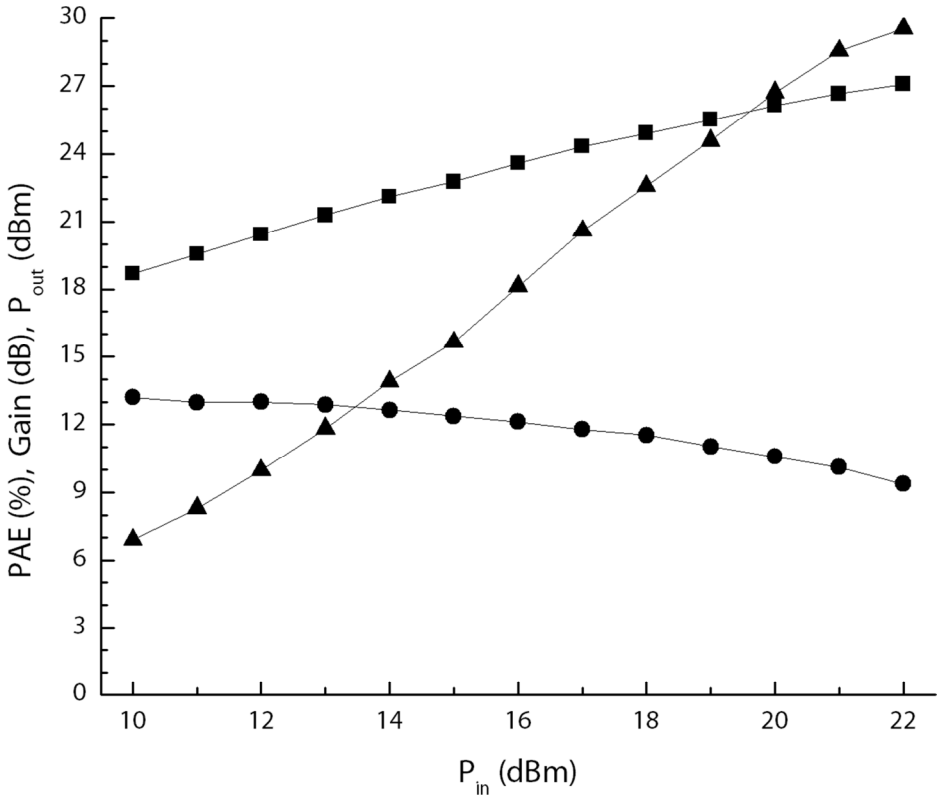

Figure 23. 18 GHz large-signal power-matched performance of a 2 × 75 × 0.1 μm (FP), 12 μm pitch GaN-on-GaN HEMT

The surface temperature in the active region of un-gated, mesa-isolated, 80μm-wide devices was measured via Scanning Thermal Microscopy (SThM). The peak operating temperature rise, averaged over several line scans, versus dissipated dc power was measured. To first-order, the temperature rise was a linear function of dissipated power; from this relationship, the thermal resistance was extracted for devices of 5, 15, and 30μm gap between the Ohmic contacts. For the structure with a 10 μm gap measured on GaN and SiC substrates using a thermal epoxy on the backside, the thermal resistance was observed to be 5.9°C/(W/mm) on SiC and only 5.2°C/(W/mm) on SI-GaN (Figure 24).

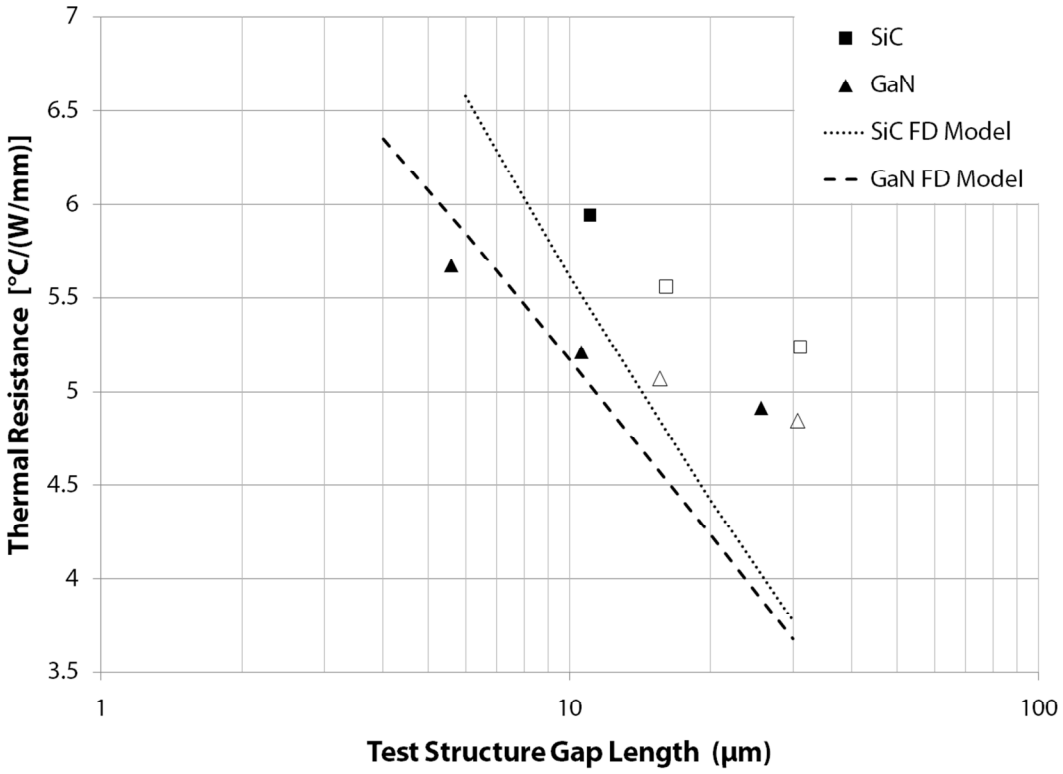

Figure 24. Thermal resistance for 80 µm-wide GaN-on-GaN and GaN-on-SiC devices measured by SThM and calculated using a 3D finite-difference (FD) model

Thermal resistance was estimated via a three-dimensional finite-difference method; for the structures on bulk GaN, analytic cylindrical-spherical and prolate spheroidal models were developed. The modeled structure on SiC includes a thermal boundary resistance (TBR) of 1.25×10^{-6} m² K/W which increases the thermal resistance of the structure by ~50%, consistent with the empirical results of [89] for similar structures. This TBR results from the dense dislocation matrix at the interface between the GaN epitaxy and the SiC substrate.

The inclusion of TBR explains the experimentally-observed comparable thermal resistance for devices on bulk GaN and SiC substrates. Particularly for the shorter gaps, the electrical probes may be acting as a heat sink, lowering the thermal

resistance. Additionally, poor backside contact between the devices and the chuck may explain the offset between the experiment and theory.

5.2.3 Summary

The growth of GaN buffers atop non-native substrates results in a threading dislocation density on the order of 10^9 cm^{-2}; for GaN-on-GaN, this value decreases by at least two orders of magnitude to below 10^7 cm^{-2} [90]. In spite of the lower dislocation density, superior alloyed contacts formed on the homoepitaxial material.

The HEMTs fabricated on SI-GaN substrate demonstrated very little dc-rf dispersion, which is consistent with good power performance up to K_a band. Despite the superior thermal conductivity of bulk SiC, the heterointerface between the buffer and the substrate impedes phonon propagation; thus, similar thermal resistance was observed for devices on GaN and SiC substrates. The outlook for HEMTs on SI-GaN substrates includes potential reliability enhancements based on reduced defect density and the elimination of epi-substrate thermal expansion mismatch.

5.3 AlInN Barrier HEMTs

HEMT frequency scaling by reducing the gate footprint is not in itself sufficient to achieve high power performance at increasing frequency. The unity-current gain frequency is inversely proportional to the effective gate length:

$$f_T = v_{eff}/(2\pi L_{G,eff}) \approx v_{eff}/[2\pi(L_{G0}+2d)] \quad (54)$$

where v_{eff} is the effective electron velocity in the GaN channel, L_G is the gate length, and d is the barrier thickness between the gate footprint and the 2DEG. When reducing gate length it is necessary to simultaneously reduce the barrier thickness in order to maintain effective gate modulation and mitigate short channel effects [91]. To maintain a desirable current density, on the order of 1 A/mm, a thinned barrier

dictates an increase in Al composition. Engineered high-Al composition $Al_xIn_{1-x}N$ barriers provide higher polarization-induced sheet charge with lower strain than is achievable using traditional $Al_xGa_{1-x}N$ barrier layers. In this work, the performance of $Al_xIn_{1-x}N$/AlN/GaN-on-SiC HEMTs is investigated.

5.3.1 Material Structure and Properties

The first $Al_xIn_{1-x}N$ material investigated in this work is comprised of a 100 Å $Al_{0.85}In_{0.15}N$ barrier, 15 Å AlN interbarrier, and 2 μm GaN buffer grown by MOCVD atop SiC. The barrier composition was chosen to be Al rich compared to lattice-matched $Al_{0.83}In_{0.17}N$/GaN case, thus leveraging piezoelectric polarization to further enhance the sheet charge density, n_s, of the 2DEG. The material did not include a GaN cap layer.

For subsequent experiments, $Al_xIn_{1-x}N$/AlN/GaN epitaxial layers were grown by MOVCD on 3" SiC substrates. The 1.85 μm GaN buffer was compensation doped with iron to increase its resistivity and mitigate subthreshold leakage current. The buffer was topped by a 15 Å AlN interbarrier and an 80 Å $Al_{0.85}In_{0.15}N$ barrier. The barrier design did not include a GaN cap layer. The surface morphology was characterized by atomic force microscopy (AFM). The 2DEG properties were examined by wetted Hg probe C–V, Lehighton, and transfer length method (TLM) measurements.

5.3.2 Fabrication and Characterization

The devices were fabricated at the Cornell NanoScale Science and Technology Facility. A standard Ta/Ti/Al/Mo/Au ohmic contact recipe was used. Mesa isolation was achieved via a $Cl_2/BCl_3/Ar$ ICP etch following the 800°C ohmic contact anneal.

In the first experiment, the 115 Å barrier was passivated with 80 nm SiN_x deposited by PECVD at 375°C. In the second experiment, the thinner, 95 Å barrier was passivated with 45 nm PECVD SiN_x at 375°C. In both cases, the passivation was etched by CF_4 and the etch-induced current degradation was ameliorated by a 450°C RTA. Finally, field-plated, Γ-shaped Ni/Au gates were deposited.

In a subsequent experiment, rectangular gates were deposited and HEMTs were characterized prior to and following 25 nm atomic layer deposition (ALD) thermal Al_2O_3 passivation, which was selectively deposited over active regions of the devices at ~100°C utilizing a high-contrast lift-off technique.

Transfer length method (TLM) measurements were performed using the four-point probe technique. DC characterization and small-signal measurements were completed using on-wafer GSG probes. Power-matched large-signal measurements were made using a Maury load–pull system at 10 GHz CW.

5.3.3 Experimental Results

The first experiment on the thicker, 115 Å barrier wafer exhibited a sheet resistance of 310 Ω/□ and sheet density $n_s = 1.6\times10^{13}$ cm^{-2}. For a representative 2×100 μm device, DC characteristics indicate a threshold voltage of V_t = -3.5 V, a full-channel current density of $I_{D,max}$ = 1.25 A/mm at V_{GS} = +1 V, and a peak transconductance of 370 mS/mm for a 220 nm-footprint gate. Despite PECVD SiN_x passivation, the gate leakage was very high compared to the thin-barrier material (Figure 25) and increased to I_G = 0.55 mA/mm at V_{GS} = -10 V.

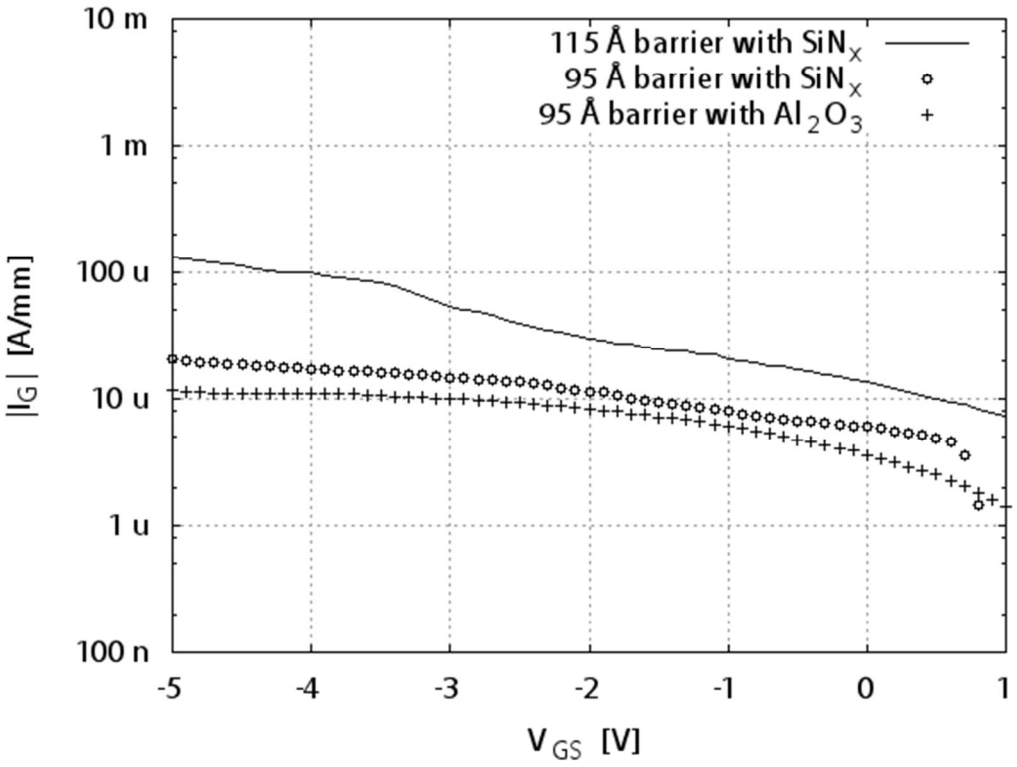

Figure 25. Gate leakage for typical 2-finger $Al_xIn_{1-x}N$/GaN-on-SiC HEMTs from each process at V_{DS} = 10 V

AFM measurement of the thin-barrier $Al_xIn_{1-x}N$ surface indicates an RMS roughness of 0.6 nm for a 10 μm scan. The 2DEG density is measured by C–V at multiple sites on the wafer as $n_s = 2.2\times10^{13}$ cm^{-2}. Excellent agreement is observed with a Schrödinger-Poisson model of the epitaxial layers. Lehighton measurements mapped across the 3" wafer prior to processing indicate $R_{sh} = 252.6 \pm 16.2$ Ω/□. This is in good agreement with TLM measurement results, presented in Table 13 alongside data from a 20 nm-$Al_{0.26}Ga_{0.74}N$/GaN-on-SiC wafer, which was processed in parallel.

Table 13. Ohmic contact properties measured by four-point probe TLM

	AlInN/AlN/GaN	AlGaN/GaN	AlInN/AlN/GaN
passivation	45 nm SiN_x	45 nm SiN_x	25 nm Al_2O_3
R_c (Ω-mm)	0.62 ± 0.05	0.43 ± 0.08	1.14 ± 0.42
R_{sh} (Ω/□)	250.3 ± 9.5	353.1 ± 2.4	291.8 ± 20.7
R_{sc} (Ω-cm²)	$1.5 \pm 0.3 \times 10^{-5}$	$5.5 \pm 2.4 \times 10^{-6}$	$5.3 \pm 5.1 \times 10^{-5}$
L_t (μm)	2.49 ± 0.28	1.23 ± 0.24	4.02 ± 1.88

A study of anneal temperatures 740°C–820°C in 20°C increments confirms optimal contact formation at 800°C, the temperature used for the devices in this work.

Considering a representative 2×50 μm HEMT with L_{GD} = 1.5 μm, peak dc metrics include I_{D0} = 1.03 A/mm, $I_D\big|_{+1Vgs}$ = 1.37 A/mm, and g_m = 530 mS/mm. For this device with 0.15 μm field-plated gate footprint, unit-current-gain frequency f_T = 37 GHz and breakdown onsets at 37 V_{DS} and is preceded by an increase in gate current.

The SiN_x passivated devices exhibit ~20% drain lag in the knee region when driven with 500 ns pulses at a low duty cycle from V_{DSq} = 20 V and V_{GSq} = -5 V. Inhibited by dc-rf dispersion and restricted by breakdown to 20 V_{DS} bias, output power in deep class AB operation driven at 10 GHz CW is 4.0 W/mm with 43% P.A.E.

The third experiment involved rectangular-gate devices passivated using an ALD lift-off technique. Since pulsed IV capabilities were not available for this experiment, hysteresis was measured in the I_D–V_{DS} curves prior and subsequent to Al_2O_3 passivation. Considering all 2×50 μm HEMTs with L_{GD} between 1.5 μm and 3.5 μm, hysteresis (quantified as the percentage change in I_{DSS0} at the knee voltage) is reduced from 18% to <5% following passivation. Additionally, gate leakage is reduced

two orders of magnitude to a typical value of ~10μA/mm, similar to the SiN_x passivated devices.

5.3.4 Summary

$Al_xIn_{1-x}N$/GaN epitaxial layers on a high-thermal conductivity substrate such as SiC are a promising platform for achieving efficient, high power, high frequency operation. The thinner barrier facilitates scaling device geometries well into the mm-wave regime.

Compared to typical $Al_xGa_{1-x}N$/GaN device values, the relatively poor ohmic contact (Table 13) even at an optimized anneal temperature suggests a future contact metallization study for high-Al-composition, wider band gap $Al_xIn_{1-x}N$ barriers. It is observed that channel breakdown is seeded by an increase in hot electrons tunneling through the sharp $Al_xIn_{1-x}N$ barrier; this motivates the in-situ growth of a GaN cap layer [43] or the deposition of a thin gate dielectric [92] to reduce the tunneling probability. The demonstrated lift-off ALD is a powerful technique for the selective use of a thin oxide.

CHAPTER 6: CONCLUSIONS AND FUTURE DIRECTIONS

Three approaches toward the realization of high-power, high-efficiency, high-frequency transistors have been demonstrated. The first two, GaN-on-diamond and GaN-on-GaN, address thermal concerns. During rf operation, bias power dissipated as heat reduces the device low-field mobility and current density, which lowers the efficiency and perpetuates the effect. One solution is to increase gate pitch; however, the microwave performance is reduced in this case due to parasitic losses. A superior solution for high-density fabrication, which necessitates short pitch, is to improve thermal management of the device by switching to a high thermal conductivity platform, such as homoepitaxial GaN-on-GaN or composite GaN-on-diamond.

The second and third approaches, GaN-on-GaN and $Al_xIn_{1-x}N$/GaN, address electrical performance concerns. The former, homoepitaxial approach produces superior rf performance and very good thermal performance with the present limitation of commercial substrate size. As substrate production processes continue to advance, this native substrate may become the de-facto standard for high-performance microwave GaN devices. The use of $Al_xIn_{1-x}N$ barriers allows the realization of greater 2DEG charge densities than feasible on $Al_xGa_{1-x}N$. This meets the challenge of improving output power by increasing the available current swing. Some fundamental challenges remain for this relatively nascent technology, including improving device contacts and increasing breakdown to the order of 100 V commonly achieved on $Al_xGa_{1-x}N$.

In the future, the ultimate wafer for high-power performance may be composite GaN-on-diamond, but with the source epitaxial layers either re-grown on a GaN-on-diamond template or transferred from a high-quality, low-dislocation growth on SiC or bulk GaN.

The robust nature of GaN makes it a promising platform for new applications in harsh environments. For example, GaN is being actively researched for chemical sensing in harsh environments. In addition to wafer-level thermal management techniques, post-processing devices with heat-spreading thin films is an avenue rife for exploration. These over-layers include such high thermal conductivity materials as AlN, polycrystalline diamond, and graphene. It is difficult to imagine a more promising technology for the utmost in high-power mm-wave performance than GaN HEMT epitaxial layers encased between a substrate and overlayer of CVD diamond.

APPENDIX A

INFORMATION CONTROLS ON DUAL-USE TECHNOLOGY

Freedom to communicate results of basic research had long been held as one of the tenets of academia. In contrast, the communication and conduct of research into dual-use technologies of military interest is limited by statute. Dual-use encompasses technologies, such as high-speed computer processors, with applications to military and civilian systems and research areas, such as biotechnology, which may be applied for the general good or misappropriated toward biological warfare. While there are clear areas, particularly at the military system level, where these government controls are not problematic, there are many aspects of fundamental research in which government concerns about technology transfer may conflict with standard academic collaboration. Navigating those situations can be difficult.

Secrecy and its now commonplace role in government operations were born of a military heritage. Policy toward information control throughout recent U.S. administrations is embodied in a series of presidential executive orders governing classification. After World War II, the Soviet Union was the easily identifiable threat with well-characterized capabilities and methods. Fueled by the Cold War Zeitgeist, the impetus for President Eisenhower's national security policy was to "meet the Soviet threat" and protect the United States' "economy, values, and institutions."[2] This policy emphasized the federal role in protecting the country's economic strength, which remains a top priority today. In response to the Soviet threat, the U.S. government keenly protected the research, development, and production of US technology of military interest, limiting communication of ideas between foreign and domestic scientists as well as restricting the export of goods. The concern about secrecy is well-

[2] Eisenhower, Dwight D. (1953). "NSC 162/2: Basic National Security Policy." 30 October.

captured in a 1978 memo from an official at the CIA's Office of Performance Evaluation and Improvement to the Director of Central Intelligence with respect to the U.S. satellite photoreconnaissance program; in it, he expressed "concern about… further inquiries and disclosures, particularly [Freedom of Information Act requests];" within the intelligence community, concealing the existence of a secret is considered the "first line of defense for security."[3] This mentality, while clearly important for national security, is at odds with the collaborative nature of the scientific process carried out at university research labs throughout the country

Over the latter half of the 20th century, university scientific research became increasingly dependent upon federal support. One of the first examples of the conflict between academia and the government over information controls came from a letter from J. A. Meyer of the National Security Agency (NSA) to the organizers of an October 10, 1977, Institute of Electrical and Electronics Engineers (IEEE) cryptology symposium in Ithaca, New York. In the letter, Mr. Meyers cautioned this group to be cognizant of export controls, including the State Department's International Traffic in Arms Regulations (ITAR),[4] which authorized extreme financial penalties and imprisonment for individuals who exported designated controlled information. In this case, Mr. Meyer was interpreting ITAR's fundamental research exclusions within a new, quite narrow scope. This was the first of many public encounters between academic and industrial scientists interested in publishing results of fundamental research and government officials increasingly concerned with a perceived threat to national security posed by those publications.

---

[3] Office of Performance Evaluation and Improvement (1978). Memorandum for the Director of Central Intelligence. 13 September. At http://www.fas.org/sgp/othergov/nrpdecl.html.

[4] Shapley, Deborah and Kolata, Gina Bari. (1977). "Cryptology: Scientists Puzzle Over Threat to Open Research, Publication." *Science* 197:1345-1349. 30 September.

Toward the end of the Carter administration, federal government officials became increasingly concerned with foreign nationals, specifically those from communist countries, training in the nation's top universities. By 1979, 21%, 26%, and 47% of U.S. doctoral degrees respectively in physical science, mathematical sciences, and engineering were bestowed upon foreign nationals.[5] The fear was that student researchers would have access to sensitive information. The federal response to concerns about unwanted technology transfer in the early 1980s was to further increase controls on the exchange of technical information, particularly in the fields of cryptology and high-speed electronics.

The threat to national security by foreign nationals was often documented in high-profile cases. For example, the "magnitude of the Soviets' collection effort and… ability to assimilate collected equipment and technology…" was revealed by the December 1983 publication of information obtained by the French counter-intelligence agency from a KGB defector codenamed "Farewell."[6] It had become clear that "the Soviets were stealing the U.S. blind."[7] That said, the September 1985 U.S. report on the "Farewell" documents, *Soviet Acquisition of Militarily Significant Western Technology: An Update*, released by Secretary of Defense Caspar Weinberger, overrepresented the collective importance of the Soviet acquisitions, much of which were never classified.[8]

Within this climate of anxiety over perceived threats, President Reagan issued the National Security Study Directive (NSSD) 11-82 "U.S. Policy Toward the Soviet

---

[5] Wallerstein, Mitchel B. (1982). "The Role of Foreign Nationals Studying or Working in U.S. Universities and Other Sectors." *Scientific Communication and National Security*. Washington, D.C.: National Academy Press.
[6] Hanson, P. (1986). *Soviet Industrial Espionage: Some New Information*. University of Birmingham Centre for Russian and East European Studies. January Draft.
[7] Corson, D. R. (2007). Interview at his residence, Ithaca, NY. 6 December.
[8] Hanson, P. (1986). *Soviet Industrial Espionage: Some New Information*. University of Birmingham Centre for Russian and East European Studies. January Draft.

Union" on August 21, 1982, the response to which, dated December 6, called for a tightening of controls on "dual-use technology, products, services and know-how… to protect the lead-time on which the qualitative advantage of U.S. military strength depends."[9]

Contemporaneously, the National Academy of Sciences Panel on Scientific Communication and National Security, formed at the behest of the Department of Defense, identified three categories of university research: basic research for the benefit of humankind, which should not be controlled; research with near-term military applications, for which classification is requisite; and a narrow "gray area" necessitating limited restrictions.[10] For such narrowly-determined areas, the panel recommended disallowing students from designated countries from participating in specific federally-funded research contracts and university reporting of foreign nationals seeking to join such projects. To assuage concerned scientists, the panel requested a periodically published summary of government restrictions upon scientific communication.

On December 23, 1982, President Reagan issued NSSD 14-82 entitled "Scientific Communication and National Security," charging a fourteen-agency group, including the National Science Foundation, to propose a National Security Decision Directive (NSDD) "Policy for Protection of Sensitive, but Unclassified, Scientific Information" to the National Security Council by March 1, 1983.[11] Within the directive, the administration acknowledged that certain government controls may not be appropriate for application to the derivatives of scientific discovery and alluded to inconsistent policy with respect to the presentation of scientific findings. Such a NSDD

---

[9] Interagency Group No. 30. (1982.) *Response to NSSD 11-82: U.S. Relations with the USSR*. 6 December.
[10] National Academy of Sciences. (1982). *Scientific Communication and National Security*. Washington, D.C.: National Academy Press. 30 September.
[11] Reagan, R. (1982). *NSSD 14-82: Scientific Communication and National Security*. 23 December.

on sensitive, but unclassified (SBU) scientific information was never issued, and a formal response to the recommendation of the NAS Panel would not be issued for two-and-a-half years.

The years after the issuance of the National Academy report were accompanied by increased military funding of academic research.[12] There were signs of improving political climate, including policy reviews in late 1984 by the Departments of Defense, Commerce, and State; however, the uniform policy sought by researchers and recommended by the NAS panel remained elusive.

President Reagan signed NSDD 189, "National Policy on the Transfer of Scientific, Technical and Engineering Information," on September 21, 1985. In the halls of academia, the issue was put to rest, as NSDD 189 satisfied those involved in the debate.[13] However, the social contract lasted only a few years. In 1989, former Executive Officer of the American Association for the Advancement of Science (AAAS) Bill Carey commented, "…what science may see as important, desirable, and useful in international cooperation is hostage to the very fast and conclusive veto of the security establishment."[14]

The Reagan administration was concerned about maintaining American technological advantage in light of the Soviet threat. President Reagan's 1982 EO 12356 reversed the trend toward openness under Presidents Nixon and Carter by removing provisions for mandatory declassification.

After the fall of the USSR, the threat shifted to nation states with lesser-characterized methods and nebulous non-state actors. Proliferation concerns lingered, while the "mirror imaging" practices effective in the Soviet era were rendered

---

[12] Nelkin, D. (1984). *Science as Intellectual Property*. New York: Macmillan Publishing Company.
[13] Corson, D. R. (2007). Interview at his residence, Ithaca, NY. 6 December.
[14] Carey, W. D. (1989). *Science and Society: Uncensored Opinions of a Science Watcher*. Keynote address at the 20th Anniversary of the Science & Technology Studies Program at Cornell University.

obsolete.[15] In this multi-polar world, the threat became asymmetric, but the policies, deeply rooted in their cold war origins, fell short of suiting the sociopolitical climate.

The Clinton Administration of the 1990s was marked by a period of relative calm among superpowers and increased openness in government. In 1995, President Clinton repealed President Reagan's order EO 12356 and replaced it with EO 12958, "Classified National Security Information." This order reinstated the policy of broad, automatic, declassification established by Nixon but later revoked by Reagan.

The attacks on American soil on September 11, 2001, dramatically affected the government's perception of threats to national security. President George W. Bush amended President Clinton's order via EO 13292. The revised introduction broadened the definition of national security information requiring protection to include "information relating to defense against transnational terrorism." It also added language about protecting "our homeland security" to its motivations for classifying information. Stripped from the introduction of EO 13292 was the post-Cold War observation that "dramatic changes have altered, although not eliminated, the national security threats that we confront… [providing] a greater opportunity to emphasize our commitment to open Government." Along with a shift away from openness in government, this order established the office of the Vice President on equal footing with the office of the President with respect to granting original classification authority and providing exemptions to mandatory declassification review.

In the academic realm, the individual's freedom to publish and collaborate openly is balanced against the government's desire to limit the dissemination of the latest dual-use technologies in the interest of protecting the public and state. The progress of science and changes in the international system have increased the risks to

---

[15] Epstein, Gerald R. (2009). *Assessing the Security Significance of Emerging and Dual-Use Technology.* Bovay Seminar in History and Ethics in Engineering at Cornell University. 4 November.

national security from the spread of technical information. In addition to the globalization of science, recently flourishing fields, such as biotechnology, have lower barriers to entry than previous areas of concern, such as high-speed integrated circuits and nuclear weapons programs. In other words, the large investment in infrastructure required for microelectronic circuits and nuclear weapons is not necessary to enter certain new fields, developments in which could pose threats to national security. State-sponsored investments are no longer required; rather, small groups of determined non-state operators with modest funding have the capacity to wreak havoc through the misapplication of dual-use technology.

The conventional wisdom of supply-side controls (i.e., export control lists) has persisted while its effectiveness has been challenged by the international diffusion and development of technology. Global markets have developed increasingly well-machined or high-purity engineering components. Additionally, software and communication systems enjoy a thriving global marketplace. For example, a 1996 NAS report on cryptography acknowledged that in spite of U.S. export controls on cryptography, "some foreign targets of interest… use [unbreakable] encryption." The report also noted that affected U.S. companies cannot export products with strong cryptography. This forces the company to split development programs between domestic and global markets, which results in a situation where "domestic availability of products with strong encryption capability is diminished."[16] This forced separation of markets increases development costs and time and results in a loss of competitive advantage. On the research side, hindrance to free scientific collaboration presents a barrier to scientific excellence. For example, U.S. scientists may be prevented from

[16] Dam, K. W. & Lin, H. (1996). *Cryptography's Role in Securing the Information Society*. Washington, DC: National Academy Press.

discussing their research with international experts by rules governing so-called "deemed exports."

The markets for defense products in the area of information technology have paled in comparison to global consumer markets. This shift was recognized in the DoD Very High Speed Integrated Circuit (VHSIC) program; dual-use spillover within the quickly-maturing electronics industry was expected to occur from commercial developments into military applications, not vice versa.[17] Since then, businesses have remained "adept at exploiting… technologies to create [and expand] market[s]" but "US leadership is not automatic."[18] A comingling of dual-use arenas has evolved in which variants on commercial parts are now implemented in military systems. In order to maintain leadership in the global marketplace, domestic companies must be allowed to compete.

The complexity of the present restrictions on technology and knowledge dissemination, as regulated by the Departments of Commerce, Defense, and State, continues to present an impediment to implementation and to enforcement. While chairing the Panel on Scientific Communication and National Security, Dr. Dale R. Corson observed, "...few people either inside or out of the government have a comprehensive understanding of the government's technology control effort."[19] The technology and government have evolved co-dependently such that black and white decisions about classification are insufficient. For this reason, the NAS report urged classification of a narrow "grey area" of dual-use technologies.

Furthermore, policy cannot keep pace with recent technological innovation. For example, consider the case of biotechnology. As a result of government controls

---

[17] Moore, David H. and Towle, William J. (1980). *The Industry Impact of the Very High Speed Integrated Circuit Program: A Preliminary Analysis*. Arlington, VA: The Analytic Sciences Corporation. 15 August.
[18] Dam, K. W. & Lin, H. (1996). *Cryptography's Role in Securing the Information Society*. Washington, DC: National Academy Press.
[19] Kolata, G. (1982). "Security Controls Hurt Research, NAS Warns." *Science* 218:271-272. 15 October.

on long, all-inclusive lists of potentially dangerous biological agents, research groups have lost valuable supplies. Crudely-implemented export controls detrimentally affect research by inducing delays and contamination when biological agents are shipped across borders. "Dual-use" has become an increasingly fuzzy designation as development of civilian technology outpaces military advances.

Sociologist Georg Simmel defined a secret as a dynamic entity which defines a relationship among a triumvirate – the first party shares a secret with a second party, while the third party is excluded from the confidence.[20] Within Simmel's framework, the existence of the secret may be universally known; he cautions, "in the case of organizations which are secret in principle, the suspicion that their secrecy conceals dangers is all the more natural."[21] In practice, government projects have been hidden in the open, for example the Boston-area facilities developing the first airborne radar systems identified themselves as the "radiation lab," at the time an innocuous name. Along these lines, Ben Rich recalled Kelly Johnson's "unorthodox security methods [at the Lockheed Martin Skunk Works], which worked beautifully in the early days of the 1950s. We never stamped a security classification on any paperwork. That way, nobody was curious to read it. We just made damned sure that all sensitive papers stayed inside the skunk works."[22]

VHSIC development programs were another area of increasing government controls. On December 12, 1980, a Department of Defense (DoD) memo was sent to VHSIC research program directors detailing how ITAR restrictions would apply to the research; the memorandum's author commented, "ITAR, if enforced to the letter,

---

[20] Simmel, G. (1906). The Sociology of Secrecy and of Secret Societies. *American Journal of Sociology*. 11 (4), 441-498.
[21] Simmel, G. (1906). "The Sociology of Secrecy and of Secret Societies." *The American Journal of Sociology*, 11(4):441-498. January.
[22] Rich, B. R., & Janos, L. (1994). *Skunk Works: A Personal Memoir of My Years at Lockheed*. Boston: Little, Brown.

would cover virtually everything... people understand they are written very generally."[23] That statutory vagueness resulted in the inconsistent and increasing application of such controls to basic research. Some examples border on the absurd; at Lockheed Martin, a mug displaying the stealth program logo with the fighter protruding from a cloud was classified as top secret and needed to be locked in a safe between coffee breaks.[24]

Government information controls, including deemed exports for dual-use technologies, may have spillover consequences for information-sharing within the academic realm. Despite Reagan's NSDD 189, which states, "no restrictions may be placed upon the conduct or reporting of federally-funded fundamental research that has not received national security classification…", visa controls and citizenship requirements are prevalent in some areas of university research.

If not carefully and sparingly applied, access controls put our country at risk of falling behind in new technology. Well-implemented secrecy programs not only limit information from perceived threats, but also from those who could produce a mutual benefit from the information; even interagency cooperation is hindered by excessive secrecy. Within the framework established by Georg Simmel, it may be useful to divide the "other" from whom the secret is withheld into two categories – those who would derive mutual benefit from knowing the secret and the threat from which the secret is withheld. For example, within the context of government information sharing of national security information, there is a desire to communicate effectively among federal, state, and local agencies without the impediments of the classifications system. Steven Aftergood, director of the Project on Government Secrecy at the Federation of American Scientists, identifies this lack of distinction within the classification system

---

[23] Kolata, Gina B. (1981). "Attempts to Safeguard Technology Draw Fire." *Science* 212:523-526. 1 May.
[24] Rich, B. R., & Janos, L. (1994). *Skunk Works: A Personal Memoir of My Years at Lockheed*. Boston: Little, Brown.

as an "embarrassment," in that the public is treated as the enemy, e.g., unauthorized disclosure to the New York Times is treated the same as that to bin Laden himself.[25]

Tighter controls on access may result in projects exceeding their budget and deadlines. In response to the Air Force classifying the stealth prototype program "top secret – special access required," Kelly Johnson, former leader of the Lockheed Martin Skunk Works, advised his replacement that "the security they're sticking onto this thing will kill you. It will increase your costs twenty-five percent and lower your efficiency to the point where you won't get any work done. The restrictions will eat you alive. Make them reclassify the thing or drop it."[26] After Lockheed was awarded the contract, the project lead noted that some of its board members "resented our independence and occasional arrogance, and suspected us of being profligate spenders hiding our excesses behind screens of secrecy imposed by our highly classified work."[27] The National Academy of Sciences identified that secrecy "has sometimes been used to stifle public debate and conceal poorly conceived and ill-informed national policies."[28]

Uncertainty of the future, specifically of unpredictable threats, presents a unique challenge, as "declassification is an irreversible step that may have harmful consequences under changed world conditions."[29] Overzealous classification either at a higher level or for a longer term than necessary has economic costs. In the decade between FY 1998 and 2008, the cost of government classification doubled to $9.85

---

[25] Aftergood, Steven. (2008). Interview at the Federation of American Scientists, Washington, DC. 22 April.
[26] Rich, B. R., & Janos, L. (1994). *Skunk Works: A Personal Memoir of My Years at Lockheed*. Boston: Little, Brown.
[27] Rich, B. R., & Janos, L. (1994). *Skunk Works: A Personal Memoir of My Years at Lockheed*. Boston: Little, Brown.
[28] Dam, K. W., & Lin, H. (1996). *Cryptography's Role in Securing the Information Society*. Washington, DC: National Academy Press.
[29] CIA, Office of Performance Evaluation and Improvement (1978). Memorandum for the Director of Central Intelligence. 13 September. At http://www.fas.org/sgp/othergov/nrpdecl.html.

billion.[30] Beyond these direct costs, indirect costs are incurred by academia when the practice of science is impeded.

Given the civilian purposes of dual-use technologies, they are rarely formally classified. Rather, they often fall under a category termed "Sensitive, but Unclassified" (SBU). The recent change in nomenclature from SBU toward "Controlled Unclassified Information" (CUI) abandons the stigma associated with the ill-defined SBU designation. The shift began when the DoD Chief Information Officer signed the May 2007 "DoD Information Sharing Strategy" and was adopted among agencies in October 2007, when George W. Bush published his "National Strategy for Information Sharing." The policy was meant to streamline nomenclature and standardize document markings throughout the government. However, the lack of rigor for designating and maintaining CUI compared to the classification system presents a quagmire for mishandling of information.

A.1 Case Study

Throughout the literature on export controls, claims of loss of competitive advantage due to government controls and, in particular, deemed exports, often go unsubstantiated. Possible metrics for measuring the effects of export controls include anecdotal, economic, and academic data. Anecdotal data are limited to select accounts and economic data are difficult to ascribe to international collaborative efforts. Of the three, the academic dataset, in particular using publication as a metric, is most suitable for a case study due to its availability, relative completeness, and ease of identifying author origin.

---

[30] Bosanko, William J. (2009). "Report on Cost Estimates for Security Classification Activities for Fiscal Year 2009." Information Security Oversight Office, Washington, DC. 25 June. At http://www.fas.org/sgp/isoo/2009costs.pdf

One way to quantify changes in behavior brought on by changes in the U.S. export control regime is to examine the response of international collaborations in the wake of a policy shift. In particular, it is useful to examine the case of a dual-use technology, the military significance of which was recognized from the outset. In such a case, collaboration ought to decrease in response to a tightening in policy and vice versa. Thus, any impediment to scientific excellence or loss in competitive advantage would be evidenced by a decrease in collaboration with international institutions.

Such international collaboration may be observed using the affiliation of the authors of scholarly publications as a variable and using publication count as the metric. The implementation of new federal information control policy is not instantaneous. Because the research process takes time and new policy trickles down slowly as contracts are let, an observable change in collaboration as measured by publication counts should follow a shift in technology policy. To test this hypothesis, I have examined the development of gallium arsenide (GaAs) technologies, covering more than three decades of scholarly publications, by quantifying collaboration between the United States and other countries within the temporal context of shifts in U.S. information control policy.

In 1980, the Department of Defense launched the VHSIC program. The program was designed to advance the state-of-the-art silicon integrated circuits and reorient and fortify suppliers to the needs of the military systems market in parallel with ongoing commercial developments. The VHSIC program focused on silicon technology, which while abundant and becoming increasingly cost-effective by markets of scale, remained limited by the narrow electrical band-gap of the material, which precluded high-power, high-temperature device operation. Fueled by a desire to exceed the frequency and environmental limitations of silicon integrated circuit technology, early gallium arsenide (GaAs) technology demonstrations included the

1963 Gunn diode and the 1971 IMPATT diode, both of which had applications in high-frequency military systems, including radar and communications. Within the context of the silicon-oriented VHSIC federal program, GaAs transistor technology represented a development with dual-use applications, both military and commercial, that were readily recognized by the government. These GaAs devices could operate at higher speeds and temperatures as well as offering greater radiation hardness than those on silicon. The military interest in GaAs transistors made it an excellent technology to test the impact of information controls on technology development.

To measure citation counts as a function of author affiliation, I utilized the Thompson Reuters Institute of Scientific Information (ISI) citation database accessible at www.isiknowledge.com. Using their *Web of Science* tool I searched the SCI-EXPANDED database from 1972 to 2008. This methodology has been employed in other literature.[31] A spot-check of highly-cited papers confirmed that the database query accurately identified the scholarly papers on the topic of GaAs transistor development.

Author affiliation, including institution and country, was indexed within the SCI-EXPANDED database. Of the 3,114 publications returned by the GaAs transistor query, a mere 81 (2.6%), all of them early papers, designated no author affiliation and they are ignored in the following statistics. Additionally, I assumed that a U.S. author of a paper with international collaborators would specify "USA" as his country of affiliation.

My research showed that within an active global scientific community, the United States was the world leader in GaAs transistor development as evidenced by scholarly publication count (Figure 26). Despite the U.S. leading role, the number of

[31] Jones, B. F., Wuchty, S., and Uzzi, B. (2008). "Multi-University Research Teams: Shifting Impact, Geography, and Stratification in Science." *Science* 322:1259-1262. 21 November.

international collaborations by U.S. scientists in this field (Figure 27) constituted less than 10% of total domestic publications. This low figure was more than just the result of information controls, in that inter-institution collaborations face barriers even among domestic institutions, for example, by the complexity of accounting and reporting requirements under contracts. These factors are relatively constant over the period of interest, so changes in collaboration may be linked to changes in controls.

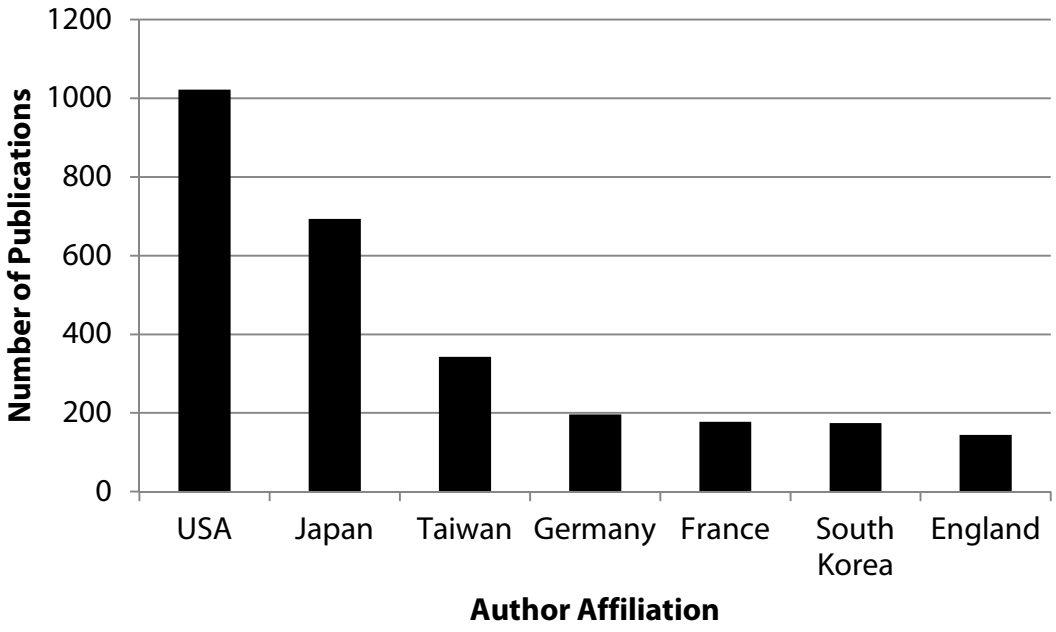

Figure 26. Number of publications on the subject of GaAs transistors by author affiliation for the top seven contributing countries, 1972–2008.

The results also showed that the distribution of domestic scholarly GaAs transistor publications per year (Figure 28) was a natural research lifecycle following the shape of an Abernathy–Utterback process innovation curve,[32] a finding that

[32] Abernathy, W.J. and Utterback, J.M. (1978). "Patterns of Industrial Innovation." *Technology Review* 80(7):40-47. June/July.

supported the claim that the publication count metric encompasses the body of publications.

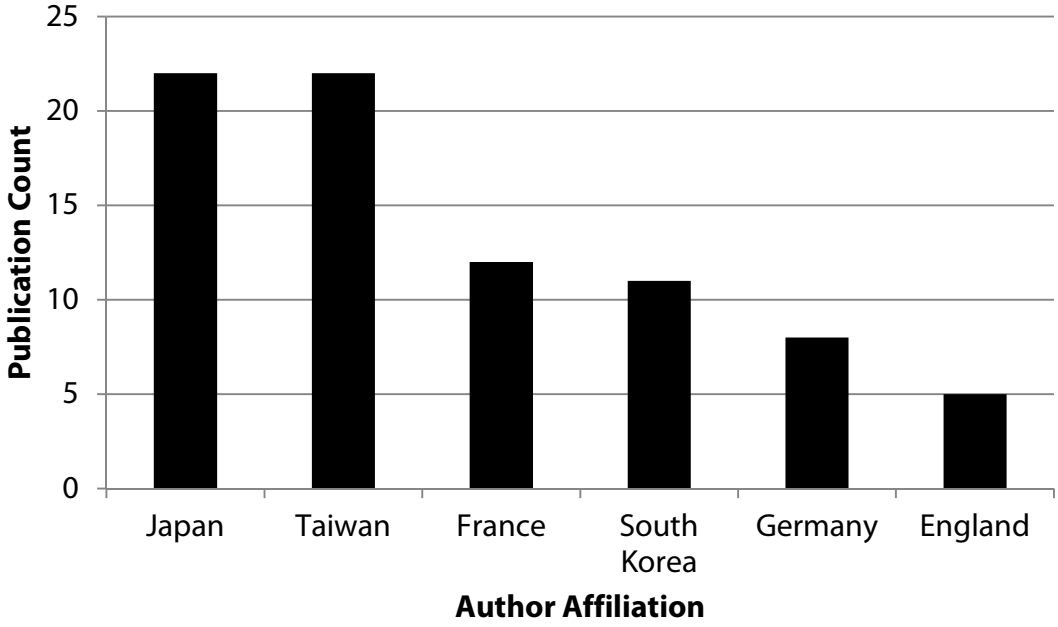

Figure 27. Collaborative publication count on the subject of GaAs transistors between the United States and other top-seven contributing countries, 1972–2008.

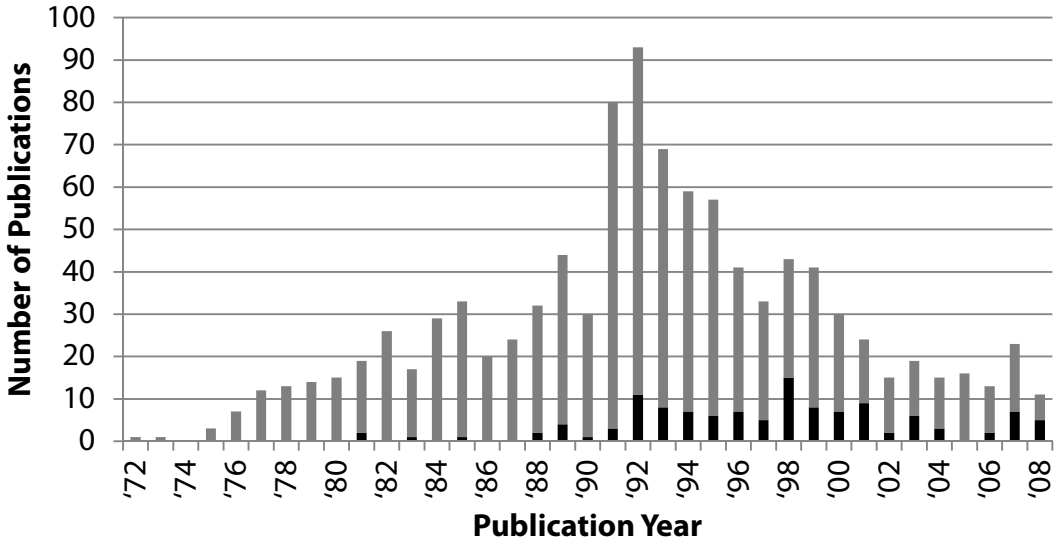

Figure 28. Number of publications on GaAs transistor technology by domestic authors, 1972–2008; black indicates the subset of publications that include collaborators with foreign affiliations.

A control technology developed for commercial interests was useful to identify the upward trend in international research collaboration. In this work, GaAs laser diodes, used primarily in civilian communications networks and optical data storage, were selected for comparison. A similar methodology was applied to identify the subset of papers including international collaborators of those published by U.S. research groups. If changes to the export control regime resulted in the creation of new barriers, then the number of international collaborations for the military-relevant technology, GaAs transistors, would be sensitive to changes in the government policy toward information controls while the number of civilian-based GaAs laser diode technology would not.

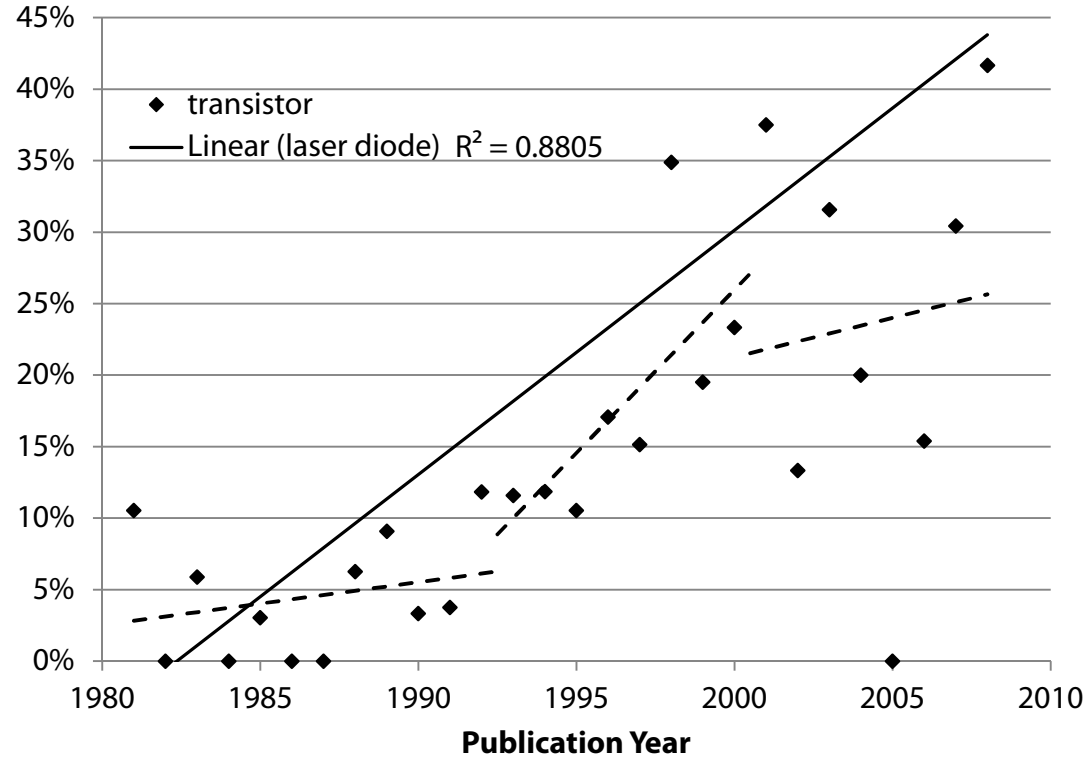

Figure 29. Percentage of US-Affiliated GaAs Publications with International Collaborators, 1981–2008.

Between 1998 and 2008, co-authored articles worldwide listing authors from institutions in more than one country grew from 8% to 22%; in 2008, 30% of U.S. papers involved international co-authors.[33] As was true more generally, the level of international collaboration among domestic authors on the subjects of GaAs transistor and laser diode development increased over time (Figure 29). Within this general trend, it is interesting to note responses to changes in the government's policy on information control. As described above, policy is most immediately affected and historically controlled by executive orders, in particular the shifts under Presidents Reagan, Clinton, and G.W. Bush. In the 1980s, along with heightened controls for

[33] National Science Board (2010). *Science and Engineering Indicators 2010*, National Science Foundation (NSB 10-01), Arlington, VA.

security reasons, globalization in civilian technologies continued as congressional actions fostered increased collaboration between academia and industry.[34,35] Subsequent administrative changes included a relaxed concentration on deemed exports in the 1990s and increased anxiety fueled by terrorism concerns under President George W. Bush's tenure. In Figure 29, a linear extrapolation for each of these three sub-periods is displayed for international collaboration in GaAs transistor development.

After President Clinton's EO 12958 took effect in April 1995, the number of international collaborations in GaAs transistor research as a percentage of domestic publication increased sharply. For the case of laser diodes which are dominated by civilian applications, the increase in the rate of collaboration can be captured by a single trend line. The annual data are not displayed, but the correlation coefficient of 0.88 reflects the linearity of the international publication percentage as a function of time (Figure 29). The response of the military-relevant GaAs transistor technology demonstrated a greater variation, particularly in the third period from 2001–08 during which the overall number of publications was decreasing (Figure 28) and, as a result, small variations in absolute collaborative publication count resulted in large changes in percentage.

Like GaAs laser diodes, the GaAs transistor research demonstrates an increasing trend in international collaboration as a function of time. However, over the three political periods, there is a notable deviation between the two technologies, which exhibit similar trends only during the Clinton administration. This comparison demonstrates an effect on rates of international collaboration sensitive to changes in

---

[34] Foerstel, H.N. (1993). *Secret Science; Federal Control of American Science and Technology*, Praeger, Westport, CT.

[35] Slaughter, S. and Rhoades, G. (1996). "The Emergence of a Competitiveness Research and Development Policy Coalition and the Commercialization of Academic Science and Technology." *Science, Technology, & Human Values* 21(3):303-339.

export control regime. The reasons for this may include self-censorship or contract stipulations. The latter case was not possible to test since the publication dataset has a largely incomplete index of funding agency. This latter case is also unlikely, as most major research universities will not accept contracts containing stipulations limiting the conduct or publication of basic research. Ultimately, this sensitivity indicates that the export controls appear to have an impact on the conduct of research.

A.2 Recommendations & Conclusion

Since the time of the Corson NAS report, the perceived threat to national security has transitioned from a well-defined nation state with well-characterized capabilities and methods, the USSR, to nebulous entities operating without the support of a sovereign state. The technology of the information age permits unparalleled access to information and analysis. The government has yet to find the ideal balance between open access and information controls.

A 1970 report by the Defense Science Board Task Force on Secrecy acknowledged that, "We may gain far more by a reasonable policy of openness because we are an open society." The report observed that during WWII, "[M]ost of the best scientists and engineers were engaged in classified defense research." It provided three examples in favor of a policy of openness. First, the U.S. lead in microwave electronics and computer technology was solidified after the 1946 release of wartime research. Next, international research and development on nuclear reactors "accelerated remarkably" following declassification in the mid-1950s. Finally, the postwar development of transistor technology was attributed to "open research."[36]

[36] Seitz, Frederick. (1970). "Report of the Defense Science Board Task Force on Secrecy." Office of the Director of Defense Research and Engineering, Washington, DC. 1 July.

Unfortunately, this publication was not persuasive to government agencies, particularly the DoD.[37]

A succinct, publicly-available list of militarily-significant technologies would alleviate confusion and aid uniform application of controls. Carefully-implemented criteria should separate system-level developments of military interest from commercial components with global markets. By concentrating on system-level developments of military interest, a separate market for secrecy could be maintained while research and development into the underlying technologies was allowed to flourish. This would also preserve "academic freedom" to collaborate in academia as well as in industry, since the global economic and intellectual marketplace requires participation for the United States to maintain its standing. The existence of a classified scientific community is an additional expense to society and impedes research. Concentrating classification efforts on specific areas with reasonable declassification targets permits most efficient use of resources to protect the evolving body of classified information.

The government must work to maintain its separate market for secrecy in order to protect military systems. The distinction must be made between commercial components that constitute technological systems of national security interest and the systems themselves. Within the realm of dual-use technology, it is advisable to develop criteria to protect system-level developments of military interest while preserving freedom for academia and industry to advance the underlying technologies in a global economic and intellectual marketplace.

[37] Aftergood, Steven. (2008). Interview at the Federation of American Scientists, Washington, DC. 22 April.

WORKS CITED

[1] A. Holmes-Siedle, "Gallium nitride, a valuable semiconductor," *Nature*, vol. 252, Dec. 1974, pp. 443-444.

[2] J. Duboz, "GaN as seen by the industry," *Comptes Rendus de l'Académie des Sciences - Series IV - Physics*, vol. 1, Mar. 2000, pp. 71-80.

[3] C.G. Van de Walle and J. Neugebauer, "Universal alignment of hydrogen levels in semiconductors, insulators and solutions," *Nature*, vol. 423, Jun. 2003, pp. 626-628.

[4] E. Kohn and D. Maier, "InAlN/GaN HEMTs," *WOCSEMMAD*, Newport Beach, CA: 2010.

[5] O. Ambacher, B. Foutz, J. Smart, J.R. Shealy, N.G. Weimann, K. Chu, M. Murphy, A.J. Sierakowski, W.J. Schaff, L.F. Eastman, R. Dimitrov, A. Mitchell, and M. Stutzmann, "Two dimensional electron gases induced by spontaneous and piezoelectric polarization in undoped and doped AlGaN/GaN heterostructures," *Journal of Applied Physics*, vol. 87, Jan. 2000, pp. 334-344.

[6] O. Ambacher, J. Majewski, C. Miskys, A. Link, M. Hermann, M. Eickhoff, M. Stutzmann, F. Bernardini, V. Fiorentini, V. Tilak, B. Schaff, and L. Eastman, "Pyroelectric properties of Al(In)GaN/GaN hetero- and quantum well structures," *Journal of Physics: Condensed Matter*, vol. 14, 2002, pp. 3399-3434.

[7] D. Fritsch, H. Schmidt, and M. Grundmann, "Band-structure pseudopotential calculation of zinc-blende and wurtzite AlN, GaN, and InN," *Physical Review B*, vol. 67, Jun. 2003, p. 235205.

[8] E. Burstein, "Anomalous Optical Absorption Limit in InSb," *Physical Review*, vol. 93, Feb. 1954, p. 632.

[9] T.L. Tansley and C.P. Foley, "Optical band gap of indium nitride," *Journal of Applied Physics*, vol. 59, 1986, pp. 3241-3244.

[10] V.Y. Davydov and A.A. Klochikhin, "Electronic States in InN and Lattice Dynamics of InN and InGaN," *Indium Nitride and Related Alloys*, Boca Raton, FL: CRC Press, 2010, pp. 181-242.

[11] P.D.C. King, T.D. Veal, A. Adikimenakis, H. Lu, L.R. Bailey, E. Iliopoulos, A. Georgakilas, W.J. Schaff, and C.F. McConville, "Surface electronic properties of undoped InAlN alloys," *Applied Physics Letters*, vol. 92, 2008, p. 172105.

[12] R. Quay, *Gallium Nitride Electronics*, Springer, 2008.

[13] I. Vurgaftman and J.R. Meyer, "Band parameters for nitrogen-containing semiconductors," *Journal of Applied Physics*, vol. 94, 2003, pp. 3675-3696.

[14] R. Goldhahn, P. Schley, A. Winzer, G. Gobsch, V. Cimalla, O. Ambacher, M. Rakel, C. Cobet, N. Esser, H. Lu, and W. Schaff, "Detailed analysis of the dielectric function for wurtzite InN and In-rich InAlN alloys," *physica status solidi (a)*, vol. 203, 2006, pp. 42-49.

[15] P. Schley, R. Goldhahn, A.T. Winzer, G. Gobsch, V. Cimalla, O. Ambacher, H. Lu, W.J. Schaff, M. Kurouchi, Y. Nanishi, M. Rakel, C. Cobet, and N. Esser, "Dielectric function and Van Hove singularities for In-rich $In_xGa_{1-x}N$ alloys: Comparison of N- and metal-face materials," *Physical Review B*, vol. 75, May. 2007, p. 205204.

[16] S. Burghartz and B. Schulz, "Thermophysical properties of sapphire, AlN and $MgAl_2O_4$ down to 70 K," *Journal of Nuclear Materials*, vol. 212-215, Sep. 1994, pp. 1065-1068.

[17] "Properties and Benefits of Sapphire: A Quick Reference Guide."

[18] Y. Wu, M. Moore, A. Saxler, T. Wisleder, and P. Parikh, "40-W/mm Double Field-plated GaN HEMTs," *Device Research Conference, 2006 64th*, 2006, pp. 151-152.

[19] F. Roccaforte, M. Weng, C. Bongiorno, F. Giannazzo, F. Iucolano, and V. Raineri, "Structural defects and device electrical behaviour in AlGaN/GaN heterostructures grown on 8° off-axis 4H-SiC," *Applied Physics A: Materials Science & Processing*.

[20] S. Tirelli, D. Marti, Haifeng Sun, A. Alt, H. Benedickter, E. Piner, and C. Bolognesi, "107-GHz (Al,Ga)N/GaN HEMTs on Silicon With Improved Maximum Oscillation Frequencies," *Electron Device Letters, IEEE*, vol. 31, 2010, pp. 296-298.

[21] T.J. Anderson, F. Ren, L. Voss, M. Hlad, B.P. Gila, L. Covert, J. Lin, S.J. Pearton, P. Bove, H. Lahreche, and J. Thuret, "AlGaN/GaN high electron mobility transistors on Si/SiO_2/poly-SiC substrates," *Journal of Vacuum Science & Technology B: Microelectronics and Nanometer Structures*, vol. 24, 2006, pp. 2302-2305.

[22] N. Defrance, J. Thorpe, Y. Douvry, V. Hoel, J. De Jaeger, C. Gaquiere, Xiao Tang, M. di Forte-Poisson, R. Langer, M. Rousseau, and H. Lahreche, "AlGaN/GaN HEMT High Power Densities on SiC/SiO2/poly-SiC Substrates," *Electron Device Letters, IEEE*, vol. 30, 2009, pp. 596-598.

[23] A. Dussaigne, M. Malinverni, D. Martin, A. Castiglia, and N. Grandjean, "GaN grown on (1 1 1) single crystal diamond substrate by molecular beam epitaxy," *Journal of Crystal Growth*, vol. 311, Oct. 2009, pp. 4539-4542.

[24] M. Alomari, A. Dussaigne, D. Martin, N. Grandjean, C. Gaquiere, and E. Kohn, "AlGaN/GaN HEMT on (111) single crystalline diamond," *Electronics Letters*, vol. 46, 2010, pp. 299-301.

[25] J. Zimmer and G. Chandler, "Advances in large diameter GaN on diamond substrates," *Proc. CS MANTECH*, Chicago, IL: 2008.

[26] J. Zimmer, "GaN on SOD Substrates," *WOCSEMMAD*, Newport Beach, CA: 2010.

[27] K. Chabak, J. Gillespie, V. Miller, A. Crespo, J. Roussos, M. Trejo, D. Walker, G. Via, G. Jessen, J. Wasserbauer, F. Faili, D. Babic, D. Francis, and F. Ejeckam, "Full-Wafer Characterization of AlGaN/GaN HEMTs on Free-Standing CVD Diamond Substrates," *Electron Device Letters, IEEE*, vol. 31, 2010, pp. 99-101.

[28] E. Piner, J. Zimmer, J. Roberts, G. Chandler, and R. Sadler, "Epi-Inverted N-Face GaN/Diamond for AlGaN/GaN/AlGaN FETs," *WOCSDICE*, Málaga, Spain: 2009.

[29] J. Chung, E. Piner, and T. Palacios, "N-Face GaN/AlGaN HEMTs Fabricated Through Layer Transfer Technology," *Electron Device Letters, IEEE*, vol. 30, 2009, pp. 113-116.

[30] D. Francis, F. Faili, D. Babic, F. Ejeckam, A. Nurmikko, and H. Maris, "Formation and characterization of 4-inch GaN-on-diamond substrates," *Diamond and Related Materials*, vol. 19, Feb. , pp. 229-233.

[31] D.C. Look and J.R. Sizelove, "Dislocation Scattering in GaN," *Physical Review Letters*, vol. 82, Feb. 1999, pp. 1237-1240.

[32] I. Arslan, A. Bleloch, E.A. Stach, and N.D. Browning, "Atomic and Electronic Structure of Mixed and Partial Dislocations in GaN," *Physical Review Letters*, vol. 94, Jan. 2005, p. 025504.

[33] N.G. Weimann, L.F. Eastman, D. Doppalapudi, H.M. Ng, and T.D. Moustakas, "Scattering of electrons at threading dislocations in GaN," *Journal of Applied Physics*, vol. 83, 1998, p. 3656.

[34] D. Jena, A.C. Gossard, and U.K. Mishra, "Dislocation scattering in a two-dimensional electron gas," *Applied Physics Letters*, vol. 76, 2000, p. 1707.

[35] C. Liechti, "GaAs IC technology - Impact on the semiconductor industry," *Electron Devices Meeting, 1984 International*, 1984, pp. 13-18.

[36] S.M. Sze, *Physics of semiconductor devices*, New York: Wiley, 1981.

[37] P. Asbeck, E. Yu, S. Lau, G. Sullivan, J. Van Hove, and J. Redwing, "Piezoelectric charge densities in AlGaN/GaN HFETs," *Electronics Letters*, vol. 33, 1997, pp. 1230-1231.

[38] F. Bernardini, V. Fiorentini, and D. Vanderbilt, "Polarization-Based Calculation of the Dielectric Tensor of Polar Crystals," *Physical Review Letters*, vol. 79, Nov. 1997, p. 3958.

[39] S. Giugni and T.L. Tansley, "Comment on the compositional dependence of bandgap in AlGaAs and band-edge discontinuities in AlGaAs-GaAs heterostructures," *Semiconductor Science and Technology*, vol. 7, 1992, p. 1113.

[40] G. Martin, S. Strite, A. Botchkarev, A. Agarwal, A. Rockett, H. Morkoc, W.R.L. Lambrecht, and B. Segall, "Valence-band discontinuity between GaN and AlN measured by x-ray photoemission spectroscopy," *Applied Physics Letters*, vol. 65, 1994, pp. 610-612.

[41] M. Foisy, *A physical model for the bias dependence of the modulation-doped field-effect transistor's high-frequency performance*, Ithaca, NY: Ph.D. Dissertation, Cornell University, 1990.

[42] M. Gonschorek, J. Carlin, E. Feltin, M.A. Py, N. Grandjean, V. Darakchieva, B. Monemar, M. Lorenz, and G. Ramm, "Two-dimensional electron gas density in $Al_{1-x}In_xN$/AlN/GaN heterostructures ($0.03 \leq x \leq 0.23$)," *Journal of Applied Physics*, vol. 103, 2008, p. 093714.

[43] A.J. Sierakowski and L.F. Eastman, "Analysis of Schottky gate electron tunneling in polarization induced AlGaN/GaN high electron mobility transistors," *Journal of Applied Physics*, vol. 86, 1999, p. 3398.

[44] R. Vetury, N. Zhang, S. Keller, and U. Mishra, "The impact of surface states on the DC and RF characteristics of AlGaN/GaN HFETs," *Electron Devices, IEEE Transactions on*, vol. 48, 2001, pp. 560-566.

[45] B. Green, K. Chu, E. Chumbes, J. Smart, J. Shealy, and L. Eastman, "The effect of surface passivation on the microwave characteristics of undoped AlGaN/GaN HEMTs," *Electron Device Letters, IEEE*, vol. 21, 2000, pp. 268-270.

[46] M. Fagerlind, H. Zirath, and N. Rorsman, "A room temperature HEMT process for AlGaN/GaN heterostructure characterization," *Semiconductor Science and Technology*, vol. 24, 2009, p. 045014.

[47] F.M. Mohammed, L. Wang, H.J. Koo, and I. Adesida, "Anatomy-performance correlation in Ti-based contact metallizations on AlGaN/GaN heterostructures," *Journal of Applied Physics*, vol. 101, 2007, p. 033708.

[48] Y. Sun, X. Chen, and L.F. Eastman, "Comprehensive study of Ohmic electrical characteristics and optimization of Ti/Al/Mo/Au multilayer Ohmics on undoped AlGaN/GaN heterostructure," *Journal of Applied Physics*, vol. 98, 2005, p. 053701.

[49] S. Ruvimov, Z. Liliental-Weber, J. Washburn, D. Qiao, S.S. Lau, and P.K. Chu, "Microstructure of Ti/Al ohmic contacts for n-AlGaN," *Applied Physics Letters*, vol. 73, Nov. 1998, pp. 2582-2584.

[50] H. Morkoç, *Nitride semiconductors and devices*, New York: Springer, 1999.

[51] A. Vertiatchikh, E. Kaminsky, J. Teetsov, and K. Robinson, "Structural properties of alloyed Ti/Al/Ti/Au and Ti/Al/Mo/Au ohmic contacts to AlGaN/GaN," *Solid-State Electronics*, vol. 50, Jul. , pp. 1425-1429.

[52] L. Wang, F.M. Mohammed, and I. Adesida, "Differences in the reaction kinetics and contact formation mechanisms of annealed Ti/Al/Mo/Au Ohmic contacts on n-GaN and AlGaN/GaN epilayers," *Journal of Applied Physics*, vol. 101, 2007, p. 013702.

[53] Y. Sun and L.F. Eastman, "Low-resistance Ohmic contacts developed on undoped AlGaN/GaN-based high electron mobility transistors with AlN interlayer," *Journal of Vacuum Science & Technology B: Microelectronics and Nanometer Structures*, vol. 24, Nov. 2006, pp. 2723-2725.

[54] *CRC handbook of chemistry and physics*, 2009.

[55] L. Smith, R. Davis, R. Liu, M. Kim, and R. Carpenter, "Microstructure, electrical properties, and thermal stability of Ti-based ohmic contacts to n-GaN," *Journal of Materials Research*, vol. 14, 1999, pp. 1032-1038.

[56] Z. Lin, W. Lu, J. Lee, D. Liu, J.S. Flynn, and G.R. Brandes, "Barrier heights of Schottky contacts on strained AlGaN/GaN heterostructures: Determination and effect of metal work functions," *Applied Physics Letters*, vol. 82, 2003, p. 4364.

[57] R. Williams, *Modern GaAs processing techniques*, Boston: Artech House, 1990.

[58] G. Pozzovivo, J. Kuzmik, C. Giesen, M. Heuken, J. Liday, G. Strasser, and D. Pogany, "Low resistance ohmic contacts annealed at 600°C on a InAlN/GaN heterostructure with $SiCl_4$-reactive ion etching surface treatment," *physica status solidi (c)*, vol. 6, 2009, pp. S999-S1002.

[59] E. Gmelin, R. Fischer, and R. Stitzinger, "Sub-micrometer thermal physics - An overview on SThM techniques," *Thermochimica Acta*, vol. 310, Feb. 1998, pp. 1-17.

[60] Raphal Aubry, Jean-Claude Jacquet, J. Weaver, Olivier Durand, P. Dobson, G. Mills, Marie-Antoinette di Forte-Poisson, Simone Cassette, and Sylvain-Laurent Delage, "SThM Temperature Mapping and Nonlinear Thermal Resistance Evolution With Bias on AlGaN/GaN HEMT Devices," *Electron Devices, IEEE Transactions on*, vol. 54, 2007, pp. 385-390.

[61] M. Thorsell, K. Andersson, M. Fagerlind, M. Sudow, P. Nilsson, and N. Rorsman, "Thermal Study of the High-Frequency Noise in GaN HEMTs," *Microwave Theory and Techniques, IEEE Transactions on*, vol. 57, 2009, pp. 19-26.

[62] T. Batten, A. Manoi, M.J. Uren, T. Martin, and M. Kuball, "Temperature analysis of AlGaN/GaN based devices using photoluminescence spectroscopy: Challenges and comparison to Raman thermography," *Journal of Applied Physics*, vol. 107, 2010, p. 074502.

[63] M. Kuball, S. Rajasingam, A. Sarua, M.J. Uren, T. Martin, B.T. Hughes, K.P. Hilton, and R.S. Balmer, "Measurement of temperature distribution in multifinger AlGaN/GaN heterostructure field-effect transistors using micro-Raman spectroscopy," *Applied Physics Letters*, vol. 82, 2003, p. 124.

[64] A. Sarua, Hangfeng Ji, K. Hilton, D. Wallis, M. Uren, T. Martin, and M. Kuball, "Thermal Boundary Resistance Between GaN and Substrate in AlGaN/GaN Electronic Devices," *Electron Devices, IEEE Transactions on*, vol. 54, 2007, pp. 3152-3158.

[65] A. Conway, P. Asbeck, J. Moon, and M. Micovic, "Accurate thermal analysis of GaN HFETs," *Solid-State Electronics*, vol. 52, May. 2008, pp. 637-643.

[66] Jungwoo Joh, J. del Alamo, U. Chowdhury, Tso-Min Chou, Hua-Quen Tserng, and J. Jimenez, "Measurement of Channel Temperature in GaN High-Electron Mobility Transistors," *Electron Devices, IEEE Transactions on*, vol. 56, 2009, pp. 2895-2901.

[67] A. Darwish, A. Bayba, and H. Hung, "Utilizing Diode Characteristics for GaN HEMT Channel Temperature Prediction," *Microwave Theory and Techniques, IEEE Transactions on*, vol. 56, 2008, pp. 3188-3192.

[68] G. Riedel, J. Pomeroy, K. Hilton, J. Maclean, D. Wallis, M. Uren, T. Martin, and M. Kuball, "Nanosecond Timescale Thermal Dynamics of AlGaN/GaN Electronic Devices," *Electron Device Letters, IEEE*, vol. 29, 2008, pp. 416-418.

[69] D. Babić, "3D Heat-Flow Analysis for Planar Field-Effect Transistors in Cylindrically Symmetric Media Using Arbitrary Heat Sources," Internal Publication, Group4 Labs, LLC, Menlo Park, CA, USA: .

[70] A. Darwish, A. Bayba, and H. Hung, "Thermal resistance calculation of AlGaN-GaN devices," *Microwave Theory and Techniques, IEEE Transactions on*, vol. 52, 2004, pp. 2611-2620.

[71] D.M. Pozar, *Microwave engineering*, Hoboken, NJ: Wiley, 2005.

[72] B. Green, "Characteristics, Optimization, and Integrated Circuit Applications of Aluminum Gallium Nitride/Gallium Nitride High Electron Mobility Transistors," Ithaca, NY: Ph.D. Dissertation, Cornell University, 2001.

[73] S. Tiwari, *Compound semiconductor device physics*, Boston: Academic Press, 1992.

[74] G. Dambrine, A. Cappy, F. Heliodore, and E. Playez, "A new method for determining the FET small-signal equivalent circuit," *Microwave Theory and Techniques, IEEE Transactions on*, vol. 36, 1988, pp. 1151-1159.

[75] J. Shealy, Jiali Wang, and R. Brown, "Methodology for Small-Signal Model Extraction of AlGaN HEMTs," *Electron Devices, IEEE Transactions on*, vol. 55, 2008, pp. 1603-1613.

[76] J. Lu, Y. Wang, L. Ma, and Z. Yu, "A new small-signal modeling and extraction method in AlGaN/GaN HEMTs," *Solid-State Electronics*, vol. 52, Jan. 2008, pp. 115-120.

[77] W.R. Curtice, "Nonlinear transistor modeling for circuit simulation," *RF and Microwave Circuits, Measurements, and Modeling*, CRC Press, Inc., 2008, pp. 32.1-32.25.

[78] I. Angelov, M. Thorsell, K. Andersson, A. Inoue, K. Yamanaka, and H. Noto, "On the Large Signal Evaluation and Modeling of GaN FET," *8th Topical Workshop on Heterostructure Microelectronics*, Nagano, Japan: 2009.

[79] G. Crupi, D. Schreurs, A. Caddemi, I. Angelov, Rui Liu, M. Germain, and W. De Raedt, "Combined empirical and look-up table approach for non-quasi-static modelling of GaN HEMTs," *Telecommunication in Modern Satellite, Cable, and Broadcasting Services, 2009. TELSIKS '09. 9th International Conference on*, 2009, pp. 40-43.

[80] T. Oishi, H. Otsuka, K. Yamanaka, A. Inoue, Y. Hirano, and I. Angelov, "Semi-physical nonlinear model for HEMTs with simple equations," *INMMIC 2010*, Göteborg, Sweden: 2010.

[81] H. Morkoç, *Handbook of nitride semiconductors and devices*, Weinheim: Wiley, 2008.

[82] V. Tilak, *Fabrication and Characterization of Aluminum Gallium Nitride/Gallium Nitride High Electron Mobility Transistors*, Ithaca, NY: Ph.D. Dissertation, Cornell University, 2002.

[83] J.R.S.E. al, "An AlGaN/GaN high-electron-mobility transistor with an AlN sub-buffer layer," *Journal of Physics: Condensed Matter*, vol. 14, 2002, p. 3499.

[84] J. Felbinger, M. Chandra, Yunju Sun, L. Eastman, J. Wasserbauer, F. Faili, D. Babić, D. Francis, and F. Ejeckam, "Comparison of GaN HEMTs on Diamond and SiC Substrates," *Electron Device Letters, IEEE*, vol. 28, 2007, pp. 948-950.

[85] D. Babic, Q. Diduck, P. Yenigalla, A. Schreiber, D. Francis, F. Faili, F. Ejeckam, J. Felbinger, and L.F. Eastman, "GaN-on-diamond Field-Effect Transistors: from Wafers to Amplifier Modules," *MIPRO*, Opatija, Croatia: 2010, pp. 597:1-7.

[86] Q. Diduck, J. Felbinger, L. Eastman, D. Francis, J. Wasserbauer, F. Faili, D. Babić, and F. Ejeckam, "Frequency performance enhancement of AlGaN/GaN HEMTs on diamond," *Electronics Letters*, vol. 45, 2009, pp. 758 -759.

[87] K. Chu, P. Chao, and J. Windyka, "Stable high power GaN-on-GaN HEMT," *High Performance Devices, 2004. Proceedings. IEEE Lester Eastman Conference on*, 2004, pp. 114-120.

[88] Yunju Sun and L. Eastman, "Large-signal performance of deep submicrometer AlGaN/AlN/GaN HEMTs with a field-modulating plate," *Electron Devices, IEEE Transactions on*, vol. 52, 2005, pp. 1689-1692.

[89] G. Riedel, J. Pomeroy, K. Hilton, J. Maclean, D. Wallis, M. Uren, T. Martin, U. Forsberg, A. Lundskog, A. Kakanakova-Georgieva, G. Pozina, E. Janzen, R. Lossy, R. Pazirandeh, F. Brunner, J. Wurfl, and M. Kuball, "Reducing Thermal Resistance of AlGaN/GaN Electronic Devices Using Novel Nucleation Layers," *Electron Device Letters, IEEE*, vol. 30, 2009, pp. 103-106.

[90] D. Storm, D. Katzer, J. Roussos, J. Mittereder, R. Bass, S. Binari, L. Zhou, D.J. Smith, D. Hanser, E. Preble, and K. Evans, "Microwave performance and structural characterization of MBE-grown AlGaN/GaN HEMTs on low dislocation density GaN substrates," *Journal of Crystal Growth*, vol. 305, Jul. 2007, pp. 340-345.

[91] G. Jessen, R. Fitch, J. Gillespie, G. Via, A. Crespo, D. Langley, D. Denninghoff, M. Trejo, and E. Heller, "Short-Channel Effect Limitations on High-Frequency Operation of AlGaN/GaN HEMTs for T-Gate Devices," *Electron Devices, IEEE Transactions on*, vol. 54, 2007, pp. 2589-2597.

[92] J. Shi, L.F. Eastman, X. Xin, and M. Pophristic, "High performance AlGaN/GaN power switch with HfO_2 insulation," *Applied Physics Letters*, vol. 95, 2009, p. 042103.